Josephson junctions fabricated via Pd diffusion into the topological insulator $(Bi_{1-x}Sb_x)_2Te_3$

INAUGURAL -DISSERTATION
zur
Erlangung des Doktorgrades
der Mathematisch-Naturwissenschaftlichen Fakultät
der Universität zu Köln

vorgelegt von

Mengmeng Bai

aus Henan, China

Köln, 2022

Berichter:	Prof. Dr. Yoichi Ando
	Prof. Dr. Thomas Lorenz
Vorsitzender der Prüfungskommission:	Prof. Dr. Petra Becker-Bohatý
Tag der mündlichen Prüfung:	24.03.2022

Contents

1 Introduction

Topological insulators (TIs) are a kind of material that has insulating bulk states and metallic surface or edge states. TIs have attracted tremendous attention from the scientific community since the beginning of this century. In 2007, a two-dimensional (2D) TI was realized in experiments in the CdTe/HgTe/CdTe quantum well system [1]. This experiment followed the proposals from Kane and Mele [2, 3], Bernevig and Zhang [4]. In the case of 3D TI, Fu and Kane made the prediction [5], and the first 3D TI material that was experimentally discovered is $Bi_{1-x}Sb_x$ [6]. Now, a lot of TI materials have been confirmed. Such as Bi_2Se_3, Bi_2Te_3 and $(Bi_{1-x}Sb_x)_2Te_3$. Majorana modes are predicted to appear in the TI [7, 8] if two s-wave superconductors are separated by a small gap located on the three-dimensional (3D) TI surface. A nonchiral one-dimensional wire for Majorana fermions will form in such an S-TI-S Josephson junction. Majorana fermions are exotic particles that are their own antiparticles [9]. Majorana fermions attracted great interest in condensed matter because they could be the building block for topological quantum computing [10]. Scientists predicted that Majorana fermions will occur in fractional quantum Hall states [11], in quantum anomalous Hall states, in p-wave superconductors [12], and in hybrid superconductor-semiconductor devices. However, the signatures of Majorana fermions observed in experiments are not convincing. People doubt the results of quantized Majorana conductance in InSb nanowire [13] and the results of chiral Majorana fermion modes in a quantum anomalous Hall insulator [14]. There are some reasons why the Majorana fermions are challenging to be detected. In the case of TIs, sometimes the signatures of surface states are hidden by the bulk. Even though we can have a very insulating bulk in ternary compounds or even quaternary compounds, a lot of impurity states may have been introduced in the TI. Secondly, the requirements for nanofabrication technology are high.

So my aim is to make high-quality SNS Josephson junction devices and search for signatures of Mjorana physics based on the JJs.

In Chapter 2, the setups for ultra-low-temperature transport measurements are discussed. The low-pass filters and the powder filters are introduced in detail. Our data are mainly taken by using a low-frequency ac lock-in technique, and the electronic measurement circuits are described.

Chapter 3 presents one of the main results of this thesis. We discovered a method to have an epitaxial self-formed superconductor on the 3D TI $(Bi_{1-x}Sb_x)_2Te_3$ (BST) thin film, which was confirmed by scanning transmission electron microscopy (STEM). I made a planar JJ and a superconducting quantum interference device (SQUID) based on this method. The BST films are successfully proximitized by the self-formed superconductor in these two devices. A junction transparency ≈ 0.96 was estimated from the SQUID. This is among the highest transparency reported for TI-based Josephson junctions. On the other hand, we also noticed that the lack of multiple Andreev reflections in SQUID is not consistent with the high transparency, such inconsistence need to be reconciled in furture studies.

In Chapter 4, we changed the Pd deposition method from magnetron sputtering to thermal evaporation. STEM results show that the Pd penetrates fully through the BST film beneath the Pd. If we deposit two Pd electrodes onto the BST film with a small gap, the BST in between would be sandwiched by SCs and a sandwich SNS Josephson junction is created. The characterization of JJs shows the resonance conductance peaks of MAR and a strong superconducting proximity effect in the BST films. At last, we did the Shapiro measurements. The missing first Shapiro step is observed, suggesting that a 4π-periodic contribution to the current-phase relation exists in our JJs, which gives possible evidence for topological Majorana bound states.

2

Ultra-low-temperature transport measurements

2.1 Noise filtering

Most of the measurements in this thesis are performed at an ultra-low temperature (~10-20 mK), and the amplitude of the signal can be smaller than 100 nV. So it is of great importance to have filters that reduce the noise to $\sim$ 20 nV, and keep the electron temperature baout 100 mK.

2.1.1 Low-pass filters at room temperature

A lock-in technique with frequencies lower than 30 Hz and a pure DC technique are applied for our measurements. So the low-pass filters are required. I will introduce two kinds of filters here. They are RC filter and LC filter, as shown in Fig.2.1. In order to avoid electromagnetic noise, the filters are packaged in a metal box (Fig.2.1.(c) and (d)).

The first one is the well-known LC filter which is also called π-filterand because of the construction arrangement of the components like the shape of the Greek letter π. The π-filter consists of one capacitor and two inductors. The cutoff frequency is the most important thing when designing a filter. The formula to calculate the cutoff frequency for the LC filter is $1/(2\pi\sqrt{LC})$. Capacitance and inductance used in this filter are 1 nF and 5 mH, respectively. Thus, the cutoff frequency $f_{LC} \approx 710$ kHz. In principle, one can get an arbitrarily small f_{LC} by increasing the value of the inductor. However, in fact, there is a parasitic capacitance in parallel to the inductor. The critical frequency for this parasitic capacitance is called self-resonant frequency (SRF). When the frequency is higher than SRF, the parasitic capacitance begins to dominate. And the high-frequency noise will flow into the measurement circuit through the parasitic capacitance.

Sometimes we need a low-pass filter with a lower cutoff frequency. We should consider the second type of filter, namely the RC filter. The filter is made of a 510 Ω resistor and two 10 nF capacitors. The mechanism of the RC filter is that noise will flow into the ground via a capacitor, and only the signal passes through the filter. We can get the cutoff frequency for RC filter depending on the formula $f_{RC} = 1/(2\pi RC)$, and the $f_{RC} \approx 31$ kHz, which is about 20 times smaller than the LC filter mentioned above. It seems that the f_{RC} can be lower if we increase the resistance or the capacitance. But we should take the actual measurement situation into account. The input impedance of Lock-ins is 10 MΩ, which means the lower cable resistance the more precision result. Besides, we know that the electrical impedance of capacitor is smaller when the capacitance is larger. Leakage current becomes serious for large capacitance. These are the two factors that limit the f_{RC}.

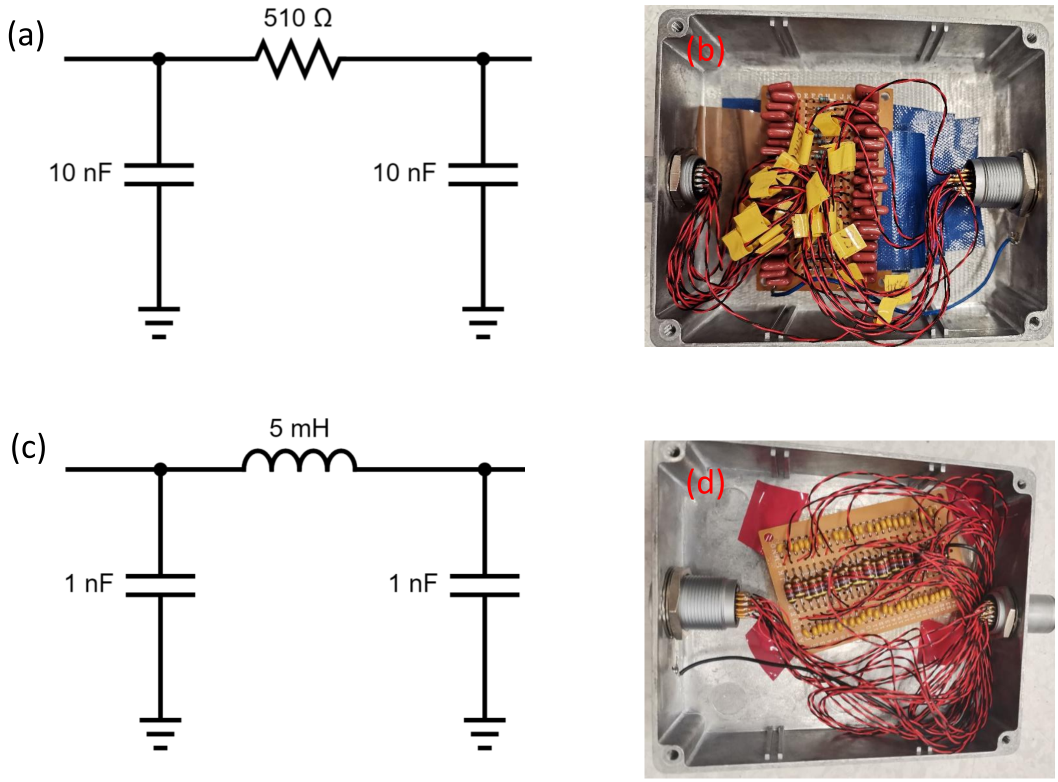

Figure 2.1: The circuit diagram and schematic diagram of RC filter and LC filter.

2.1.2 Powder filters at low temperature

The low-pass filters are very effective for the noise whose frequency is lower than ~100 MHz. However, the noise can not be screened by thise filters effectively at higher frequencies. There are kinds of filters specialized built for high-frequency noise. For instance, filters made by the coaxial cable named Thermocoax® Philips[15], filters based on microfabricated chips[16], and distributed thin-film filters[17]. One of the most well-known and widely used is the copper powder filter proposed by Martinis *et al*[18].

The metal powder filters consist of twisted wires in a shell filled with refined copper grains or stainless grains. The smallness of the powder grains gives a quite huge effective surface area. So the skin-effect damping is considerable[19]. Fig.2.2 shows a illustration of home-made metal powder filter.

Choosing an appropriate wire is important because the metal powder filter will be mounted on a cold plate of a temperature below 4K. High conductivity wires will give rise to heat leakage. Another consideration is the Joule heating caused by the wires with high resistance. We find the manganin wires with an insulating layer meet these requirements. As shown in Fig.2.2(a), 12 twisted pair wires with a diameter of 100 μm are put in an O_2-free copper housing. The length of the wires is 3 m that is long enough to have a sufficient attenuation of ~GHz noise.

Usually, Stycast epoxy is used to fix the wires and metal powders. Mix stycast 1266 part A and part B uniformly in two cups(Fig.2.2(b)), then pour the copper powder and stainless powder[20] in cups separately(Fig.2.2(c)). The mass ratio of metal powder to Stycast epoxy is 1:1. In order to avoid the distribution of metal powders are inhomogeneous that is caused by the random air bubbles in the mixture, the mixture is kept in a vacuum box to degas for about 15 minutes. Pour the mixture separately into each compartment of the box to fully immerse the wires. Solder the wires to the micro d-sub connectors at the two ends of the box(Fig.2.2(e)). The metal powder filters are mounted on the bottom of the mixing chamber plate, which is indicated by a red arrow, as shown in Fig.2.2(f).

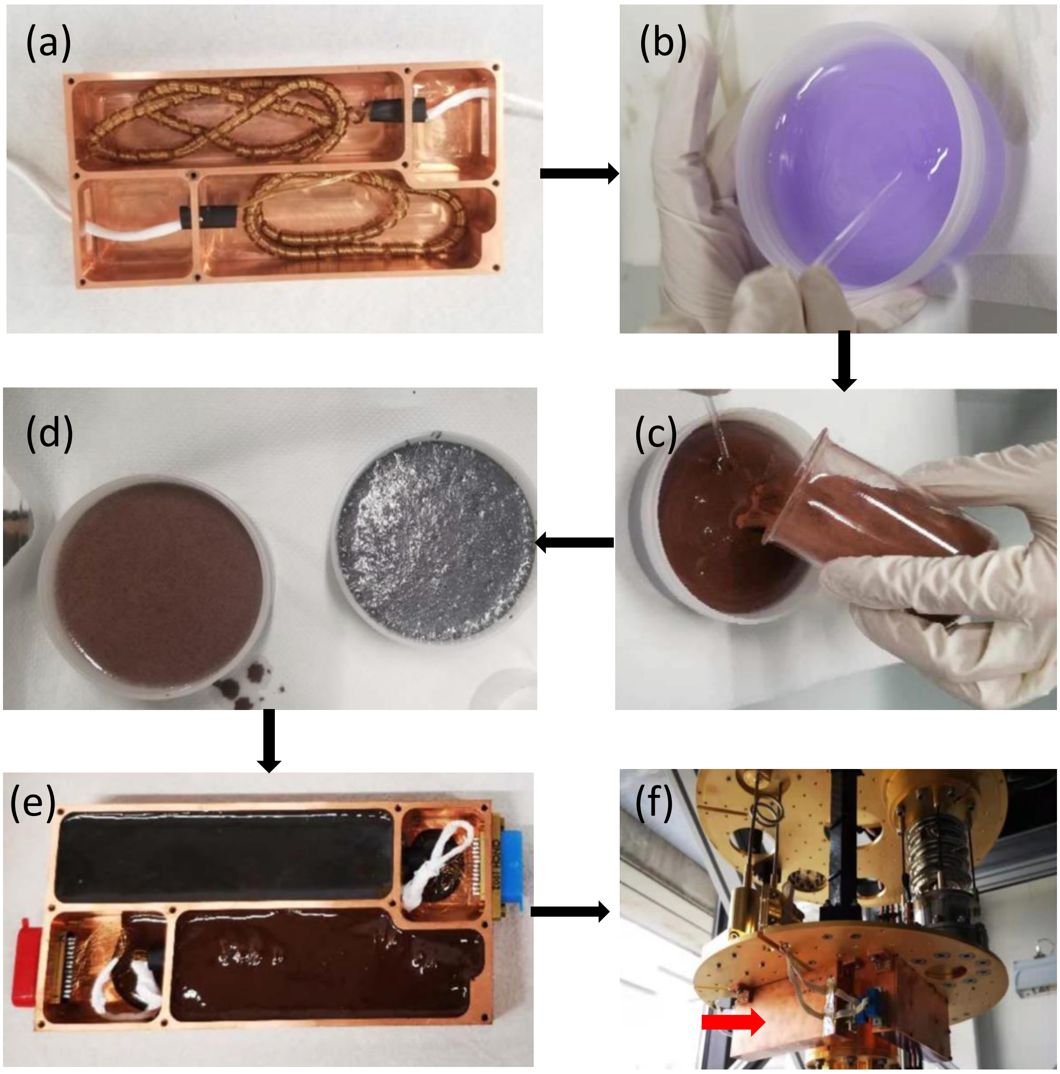

Figure 2.2: Illustration of making a powder filter

2.2 Low-frequency lock-in and DC measurements

Lock-in amplifiers play an essential role in the weak ac signals measurement. The basic idea of lock-ins is intuitive, explained by a straightforward calculation of trigonometric functions[21]. Let us consider a signal $V_S\sin(\omega_1 t+\theta_1)$ on a device, where V_S, ω_1, and θ_1 are amplitude, frequency, and phase, respectively. We multiply the signal with a sine wave reference signal $V_R\sin(\omega_2 t+\theta_2)$.

$$\begin{aligned} V_{\text{multi}} =& V_S V_R \sin(\omega_1 t + \theta_1)\sin(\omega_2 + \theta_2) \\ =& \frac{1}{2} V_S V_R \cos((\omega_1 - \omega_2)t + \theta_1 - \theta_2) \\ &- \frac{1}{2} V_S V_R \cos((\omega_1 + \omega_2)t + \theta_1 + \theta_2) \end{aligned} \tag{2.1}$$

These are two ac signals. When the V_{multi} treated by a low-pass filter, then nothing will be left but only if $(\omega_1 = \omega_2)$.

$$V_{\text{multi}} = \frac{1}{2} V_S V_R \cos(\theta_1 - \theta_2) \tag{2.2}$$

That is why only the signals with the frequencies that are very close to the lock-in reference frequency can be detected, and noise will be excluded.

The two most used measurement setups are shown in Fig2.3. Lots of the information about the physical properties of Josephson junctions are characterized by differential resistance (dV/dI). In Fig.2.3(a), a standard resistor R_1 with a resistance of 1 kΩ is used to detect the current in devices. The current is constant during the measurements because the resistance of $R_2$is two to three orders larger than the device resistance. Dc bias on the devices is provided by a Keithley 2450 sourcemeter. Both lock-ins and Keithley 2450 are voltage sources, while in fact, the devices are driven by current due to the large resistance of R_2.There are several types of locin-ins used in our lab, namely SR830, NF LI5640, and NF LI5645. Keithley 2450 can output both current and voltage, and the current limit is 1 A.

Fig.2.3(b) shows how to measure the current-voltage ($I - V$) characteristic curves. The current is output and detected by the keithley 2450, a nanovoltmeter Keithley 2182A is used to measure the voltage dropped on the devices. The noise level of Keithley 2182A is around several hundreds of nanovolts. The data is averaged over more than ten times of independent scans to have a higher SNF. The noise is reduced by $\sqrt{n}$, where n is the times of scans.

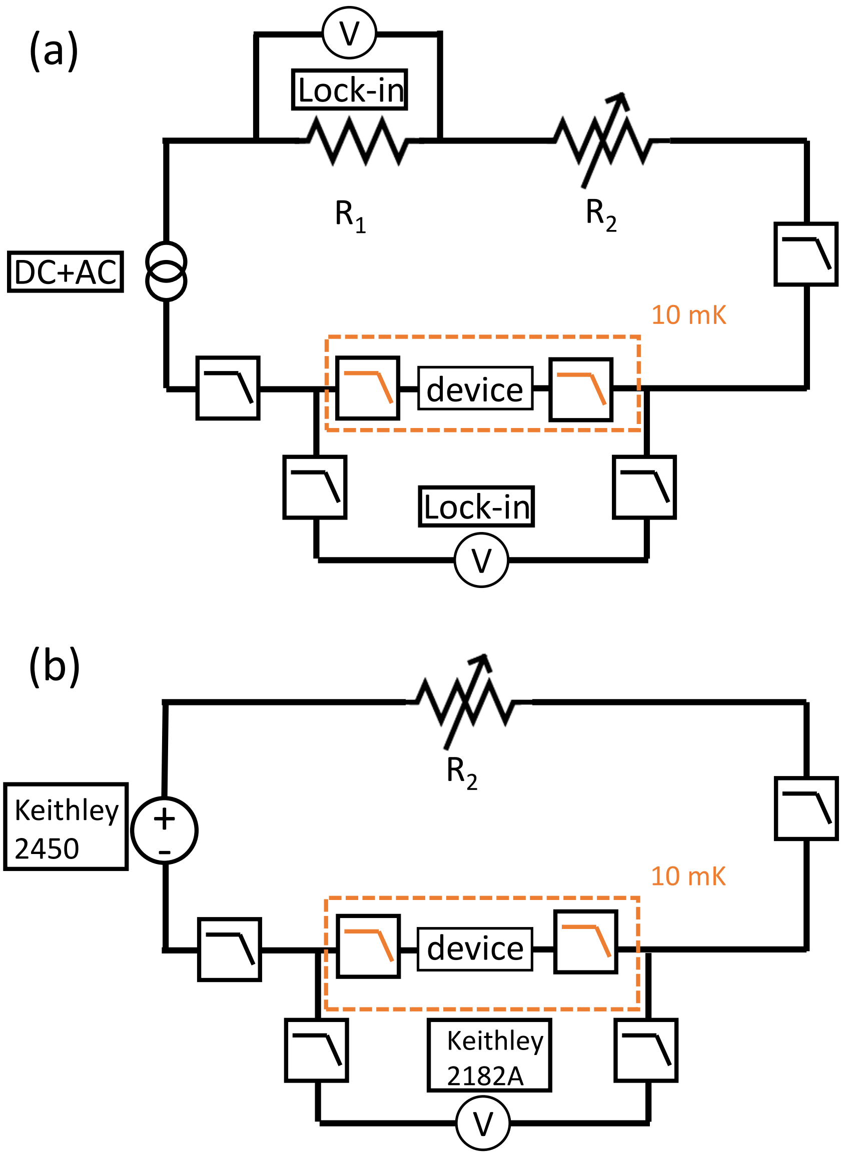

Figure 2.3: Sketch of measurement electronic circuit that uesd in this thesis. The filters in orange colour are the metal powder filters, while the RT low-pass RC or LC filters in black colour. (a) Both ac excitation and dc bias are applied on the device. Ac voltage drops on the device was measured by a lock-in. (b) A pure dc setup for measuring the I-V curves.

2.3 Shapiro-step measurements

To perform rf measurements, we use the rf signal generator R&A SGS100A (see Fig. 2.4 (a)), which can generate rf microwaves between 80 MHz and 12.75 GHz. Our devices were irradiated by rf microwaves via a coaxial cable. The open end of the coaxial cable is around ~1-2 mm above the sample holder, as shown in Fig. 2.4 (b). A 2D plot of differential resistance (dV/dI) as a function of I_{bias} and rf power for a typical Shapiro measurement is shown in Fig. 2.4 (c). The y-axis label is in the unit of dBm. One can see that the data at higher power is compressed in a small area. To display the result reasonably, the y-axis is converted to an arbitrary unit by $\sqrt{10^{(\text{rf Power})/10}}/\sqrt{10^{(\text{rf Power}_{max})/10}}$, as shown in Fig. 2.4(d). The V_{bias} is obtained from integration of dV/dI vs I_{bias}, then, V_{bias} is normalized by $hf/(2e)$ to emphasize the Shapiro-step nature of the response. Fig. 2.4(d), finally, shows a 2D plot of differential conductance (dI/dV) as a function of rf excitation and $V(hf/2e)$. The Shapiro-step nature of the response is emphasized in Fig. 2.4(d).

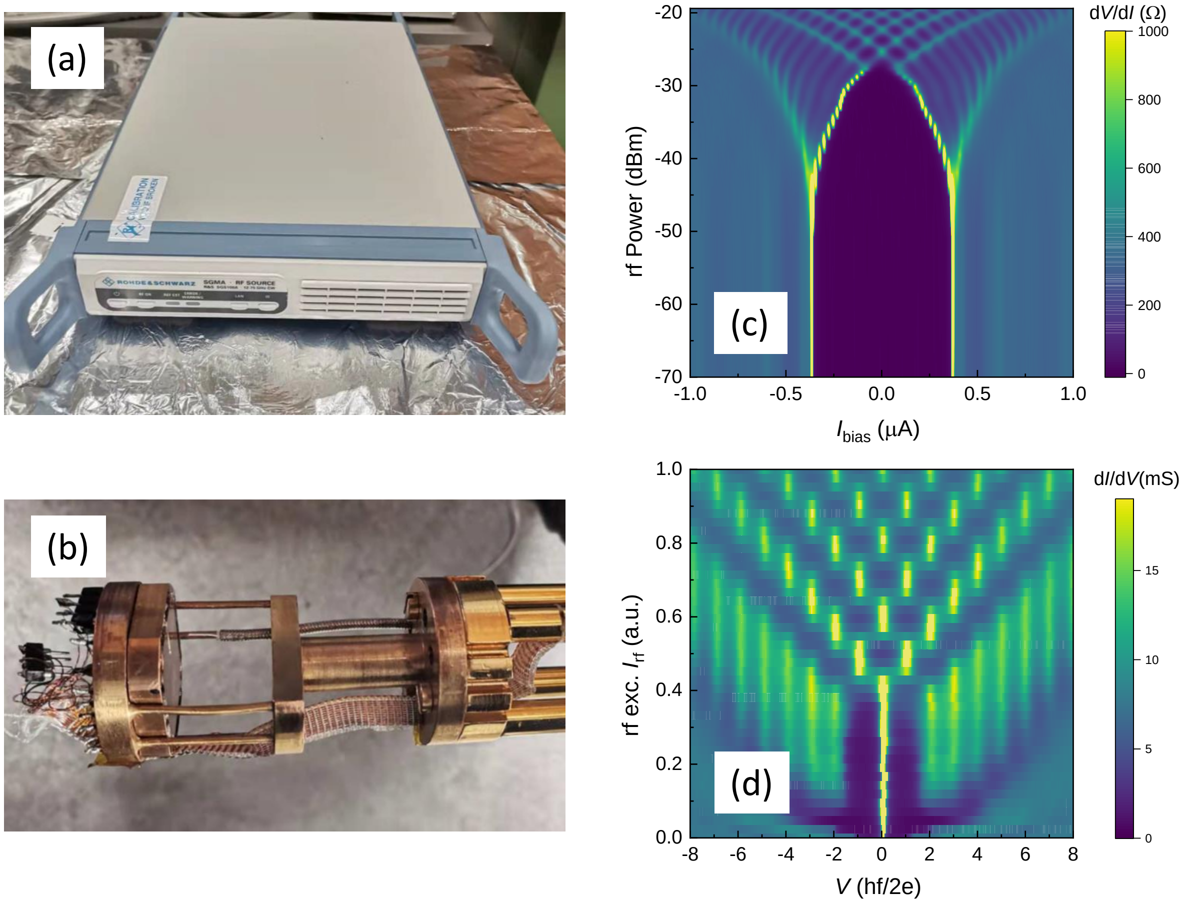

Figure 2.4: (a) A picture of a rf signal generator R&A SGS100A (b) A photograph of the sample holder and the coaxial cable. (c) 2D plot of dV/dI as a function of I_{bias} and rf power. (d) 2D plot of dI/dV as a function of V_{bias} and rf excitation.

3

Planar Josephson junction fabricated with $Pd/(Bi_{1-x}Sb_x)_2Te_3$ bilayer

In this chapter the proximity-induced superconductivity in the topological insulator is discussed. We discovered that an epitaxial self-formation of $PdTe_2$ superconductor can be obtained by simply depositing Pd on thin films of $(Bi_{1-x}Sb_x)_2Te_3$. A Josephson junction device and a SQUID were fabricated to confirm the proximity-induced superconductivity. The supercurrent is observed in both two devices. The superconductivity was characterized by the current-voltage characteristics and magnetic-field dependence of the critical current. To identify the $PdTe_2$ phase, STEM and EDX were employed. The high junction transparency is estimated from the SQUID.
The following chapter is based on a paper published as:
Mengmeng Bai, Fan Yang, Martina Luysberg, Junya Feng, Andrea Bliesener, Gertjan Lippertz, A. A. Taskin, Joachim Mayer, and Yoichi Ando; *Novel self-epitaxy for inducing superconductivity in the topological insulator $(Bi_{1-x}Sb_x)_2Te_3$*; Phys. Rev. Materials 4, 094801 (2020).

Dr. Martina Luysberg and Prof. Dr. Joachim Mayer performed the STEM analyses on the devices that were prepared by Mengmeng Bai.

3.1 Device fabrication

The Josephson junction devices were fabricated on a well-known 3D topological insulators $(Bi_{1-x}Sb_x)_2Te_3$ (BST). To some extent, BST consists of Bi_2Te_3 and Sb_2Te_3. Bi_2Te_3 is n-type doped, while Sb_2Te_3 is p-type doped [22]. So the Fermi level of BST can be shifted from the conduction band to the valence band by increasing the x value from 0 to 1 [23]. A "real" topological insulator is engineered when the Fermi level and the Dirac point are shifted inside the bulk gap [23–25].

The films were grown in the ultrahigh vacuum molecular beam epitaxy (MBE) chambers, and the best of MBE chambers in our lab can be achieved to 10^{-11} mbar [26]. Fig. 3.1(a) shows an AFM image of a freshly as-grown BST film. Triangular terraces with sharp edges are observed, and the film is atomically flat. The terraces are still observable even after Pd deposition (see Fig. 3.1(b)).Such a good morphology is an indication of high-quality films.

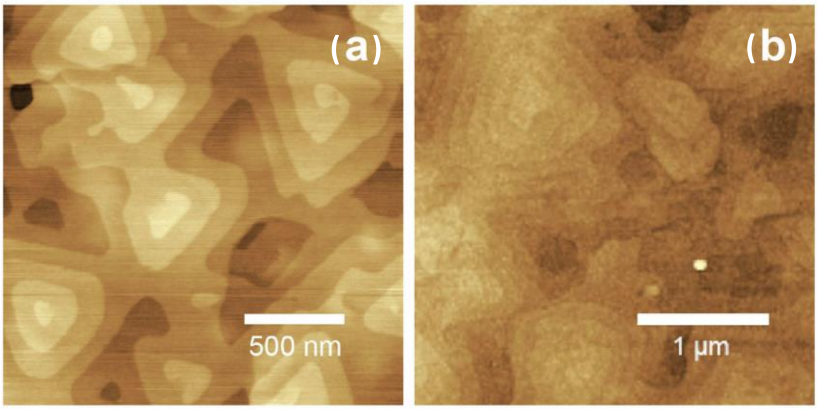

Figure 3.1: (a) AFM image of an as-grown $(Bi_{1-x}Sb_x)_2Te_3$ film. (b) AMF image of sample 1 after Pd deposition. (modified from [27])

3.1.1 Electron-beam lithography

Standard electron-beam lithography (EBL) technique was used to transfer the patterns onto BST films. At first, drop a few drops of positive Poly (methyl methacrylate) (PMMA) A4 resist on the wafer, and then spin it at 6000 rpm for 1 min. About 180 nm PMMA will cover the film uniformly, as shown in Fig. 3.2(a). The thickness of the resist was mainly determined by spin speed, and the resolution of patterns is related to the PMMA thickness. Thinner resist gives a better resolution. After spin coating, put the substrate on a hot plate at 120°C to bake the resist for 15 mins. The solvent of PMMA will be evaporated, and the glass transition of PMMA happens. The major component of PMMA is a long-chain polymer. The long-chain will be broken when PMMA is exposed to electron beams, and the broken long-chain can be dissolved into certain solvents which are called developer [28]. Compared to conventional developer MIBK, the sensitivity and contrast of PMMA resist increases a lot if one uses water/Isopropanol(IPA) as the developer [29]. The resolution of EBL also depends on the energy of the electrons. Backscattering of electrons in the resist will be reduced and the de-Broglie wavelength of the electrons is smaller when the energy of the electrons is higher. The highest energy of electron-beam in our Raith system is 30 keV, and we can have the smallest structure around 50 nm.

3.1.2 RIE plasma etching

After the resist development, the substrates are transferred in a reactive ion etching (RIE) apparatus for surface cleaning(Fig. 3.2(d)). In order to remove several nanometers of PMMA residual resist and the native oxide layer of BST film. In the RIE chamber, there are low-density plasma ions with high energy hitting against the sample. The thin residual resist layer and the oxidized layer are knocked off (sputtered). This kind of etching is called physical etching. As there are no in situ cleaning fittings in our metalization equipments, the samples need to be moved to metalization equipments immediately after RIE etching and to keep the air-exposure time as short as possible.

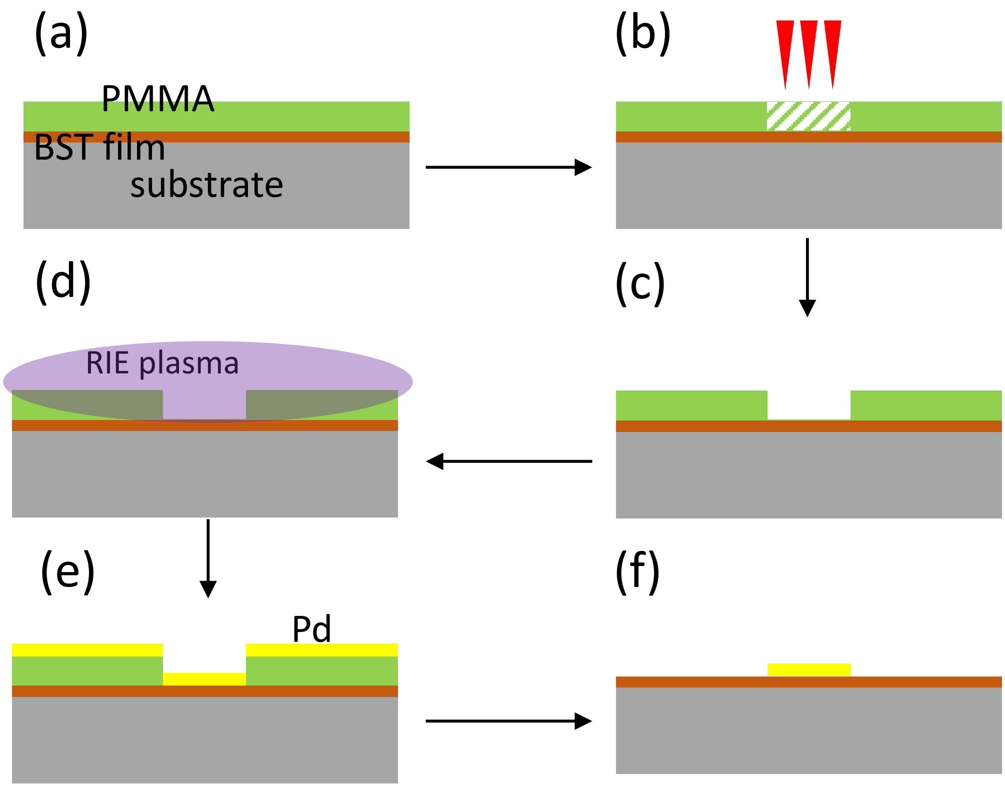

Figure 3.2: Schematic illustration of nanofabrication approach used in this thesis. (a) Spin coating of a thin layer of PMMA. (b) Electron beam lithography. (c) Development of the resist. (d) Surface cleaning by Ar plasma in RIE chamber. (e) Thin Pd film deposited on the samoles. (f) Lift-off to remove the remaining resist with the surplus Pd film.

3.1.3 Metalization

Both magnetron sputter deposition and thermal evaporation were employed for making electrodes on devices. We use a homemade one-target magnetron sputtering system with a base vacuum of $\sim 1 \times 10^{-7}$ mbar. A gaseous plasma was generated in a flow of Ar gas by applying an alternating current (ac) of radiofrequency, typically at 13.6 MHz. The electrons are confined in the area near the target by a magnetic field in a magnetron. The possibility of Ar ions created by the collision of electrons is much higher in this area. Atoms on the surface of the target will be ejected due to the collisions of Ar ions. The ejected atoms will move to the surface of the substrate through few collisions because of the vacuum environment. There are several advantages of magnetron sputtering deposition. Such as high deposition rates, high adhesion of films on the substrate, high film-quality and high repeatability.

Fig.3.2(e) shows that the samples are wholly covered by a layer of the metal film. The undesired films will be removed when putting the samples in acetone at 70°C. This is the so-called lift-off process.

3.1.4 Nanofabrication parameters of a Josephson junction device and a SQUID

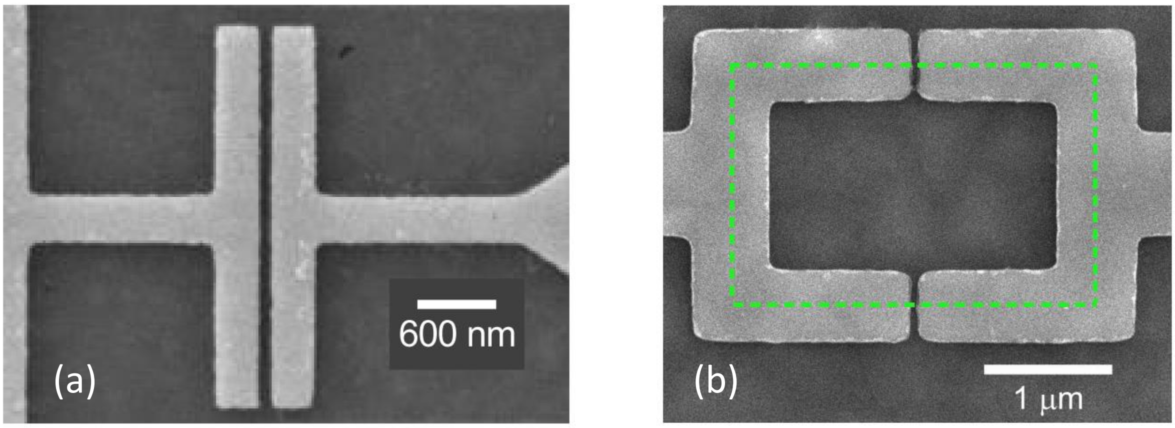

Figure 3.3: (a) SEM image of device A with Pd electrodes deposited on a 23-nm-thick BST film. (b) SEM image of device B with Pd electrodes deposited on a 35-nm-thick BST film. (modified from [27])

Figs.3.3(a) and (b) show the scanning electron microscope (SEM) images of a Josephson junction (device A) and a SQUID (device B), respectively. The thickness of BST film in device A is 22 nm, and 15 nm of Pd was deposited by magnetron sputtering. In order to have a good contrast under SEM imaging, another 15 nm of Pd was deposited by thermal evaporation. Before Pd deposition, device A was cleaned in the RIE chamber at 10 W for 1 min to remove possible resist residues and oxide layer. The BST film in device B is 35 nm thick. 20 nm and 15 nm of Pd were deposited by magnetron sputtering and by thermal evaporation sequentially. The RIE cleaning was the same as device A.

3.2 Discovery of superconductivity

A wetting layer between superconductor and TI film can reduce the contact resistance, which is helpful to have a proximity-induced superconductivity in the TI [30, 31]. In the beginning, Pd is one of the candidates for suitable wetting layers. However, we occasionally observed superconductivity in BST films with Pd electrodes. As we know, neither BST nor Pd is a superconductor. There must be a new superconducting phase created in Pd/BST bilayer films. To identify the new SC phase, scanning transmission electron microscopy (STEM) and energy-dispersive X-ray spectroscopy (EDX) were employed. Finally, the superconductor in Pd/BST bilayer film is confirmed to $PdTe_2$ (see section 3.3).

$PdTe_2$ has been a long-known superconductor since 1961 [32], and the T_C of $PdTe_2$ ranges from 1.7 K to 2.0 K [33–35]. To characterize the properties of the $PdTe_2$ superconductor in our samples, Hall-bar shaped samples were fabricated using UV photolithography, as shown in the inset of Fig. 3.4(a). Fig. 3.4(a) shows a sharp superconducting transition with a T_C of 0.67 K. T_C is defined as the temperature when the resistance drops to 50% of the normal state value in R-T curves. The superconducting transition width [36] (ΔT_C) is the temperature interval of the superconducting transition. Here ΔT_C is the changes in the temperature corresponding to the normal-state resistance changed from 90% to 10%. Usually, a narrow transition width is an indication of high homogeneity in samples. Fig. 3.4(b) shows the magnetoresistance measured at T = 8 mK, and an out-of-plane magnetic field was applied. The upper critical field $\mu_0 H_{c2}$ of this sample was 1.09 T.

Four different samples of Pd/BST bilayer films with Hall bar patterns have been investigated. The parameters of nanofabrication and properties of superconductivity for all four samples are summarized in Table 3.1. The robust superconductivity of four samples has been observed, and T_C ranges from 0.67 K to 1.22 K. The difference of T_C can be due to the different thickness of the $PdTe_2$ layer. ΔT_C of sample 2 and sample 3 is lower than sample 1 and sample 4, but the T_C is higher. This means the $PdTe_2$ formed in samples 2 and 3 is more uniform, which is consistent with the result of lower $\mu_0 H_{C2}$ in samples 2 and 3. When disorder in superconductors is increases, the $\mu_0 H_{C2}$ will be larger.

The values of T_C mentioned above are lowerr than T_C in bulk $PdTe_2$. Such behavior of T_C has also been reported by C. Liu $et al.$ [37]. They have systematically studied the T_C of MBE grown $PdTe_2$ films, and found that T_C changes dramatically depending on the film thickness. The values of T_C gradually increase as the thickness of $PdTe_2$ increases. But the reason for the different thicknesses of $PdTe_2$ in our samples is not clear. We conjecture that the thickness depends on the morphology of the BST surface and the film quality. The Pd was deposited by magnetron sputtering for all the four samples shown in Table 3.1. While at the same time, we have prepared some samples in which the Pd layer was deposited by thermal evaporation. The superconducting transition was also observed. However, there is no sufficient statistics data to compare the two Pd deposition methods. We expect that the Pd diffusion process could be stronger in thermal evaporation due to the heating of the BST surface. This is an interesting topic for future research and will be discussed in the next chapter.

$PdTe_2$ was recently reported as a type-II Dirac semimetal [38–40] and was also proposed as a candidate to realize topological superconductivity [40]. But some recent experiments about the tunneling spectroscopy of $PdTe_2$ suggest that it is most likely a conventional s-wave superconductor [41, 42]. As shown in the inset of Fig. 3.4(b), the theoretical zero-temperature value of $\mu_0 H_{C2}$ can be calculated from the slope $(d\mu_0 H_{C2}/dT)_{T=T_C} = -2.44$ T/K by using the Werthamer-Helfand-Hoenberg theory [43]. The theoretical zero-temperature value of $\mu_0 H_{C2}$ = 1.13 T agrees well with the 1.09 T measured at 8 mK, indicating the nature of the conventional s-wave superconductivity. The s-wave superconductor is applicable for making the SC/TI hybrid devices that are used to explore topological superconductivity.

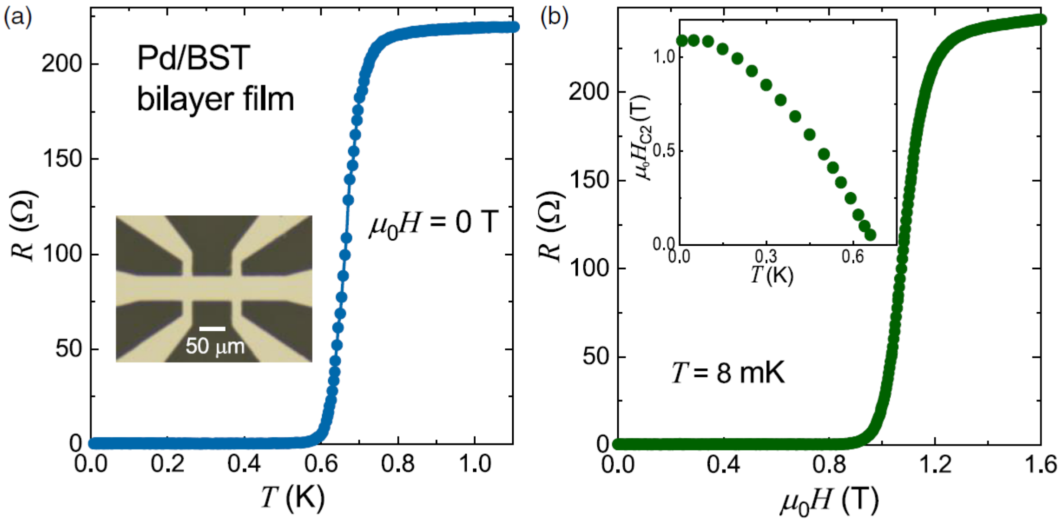

Figure 3.4: Superconducting transition of Pd/BST bilayer film in sample 1. (a) Temperature (T) dependence of the resistance (R), measured at zero magnetic field. Inset: optical image of the Hall bar. (b) Magnetic-field dependence of R, measured at T = 8 mK and magnetic field is perpendicular to sample 1. Inset: The temperature dependence of the upper critical field H_{C2}. (modified from [27])

Name	BST layer	Pd (sputt.)	Pd (evap.)	Ar-cleaning	T_c	ΔT_c	$\mu_0 H_{c2}$
Sample 1	68 nm	8 nm	0	Yes	0.67 K	0.13 K	0.84 T
Sample 2	50 nm	20 nm	0	No	1.00 K	0.04 K	0.34 T
Sample 3	16 nm	8 nm	0	Yes	1.22 K	0.04 K	0.48 T
Sample 4	23 nm	10 nm	0	Yes	0.81 K	0.15 K	0.69 T
Device A	22 nm	15 nm	15 nm	Yes	0.90 K	-	-
Device B	35 nm	20 nm	15 nm	Yes	0.70 K	-	-

Table 3.1: Summary of the preparation parameters and properties of the samples and devices measured in this study. T_c of samples 1 – 3 is defined as the temperature at the midpoint of the resistive transition. For devices A and B, T_c is defined as the midpoint of the main resistance drop in the $R(T)$ curve. H_{c2} shown here is defined as the midpoint in the resistive transition measured at T = 280 mK. ΔT_c is the width of the temperature window in which the resistance changed from 90% to 10% of the normal-state resistance during the superconducting transition. "sputt." and "evap." stand for sputtered and evaporated, respectively. (modified from [27])

3.3 STEM results and self-epitaxy

3.3.1 A brief introduction to STEM and EDX

Scanning transmission electron microscope (STEM) has been widely used to characterize the structure of thin specimens in materials science. The first STEM was built by Baron Manfred von Ardenne in 1938 [44]. Fig. 3.5(a) shows a schematic diagram of an STEM instrument[45]. In STEM, an electron beam was focused to a very tiny spot by using a series of condenser lenses. Thanks to the shortness of the de-Broglie wavelength of the electrons, the typical spot size is only 0.05-0.2 nm. The accelerated electron beam will shoot on a very thin sample, and the direction of the electrons changes because they are scattered by the atoms inside the sample. These transmitted electrons can form a STEM image.

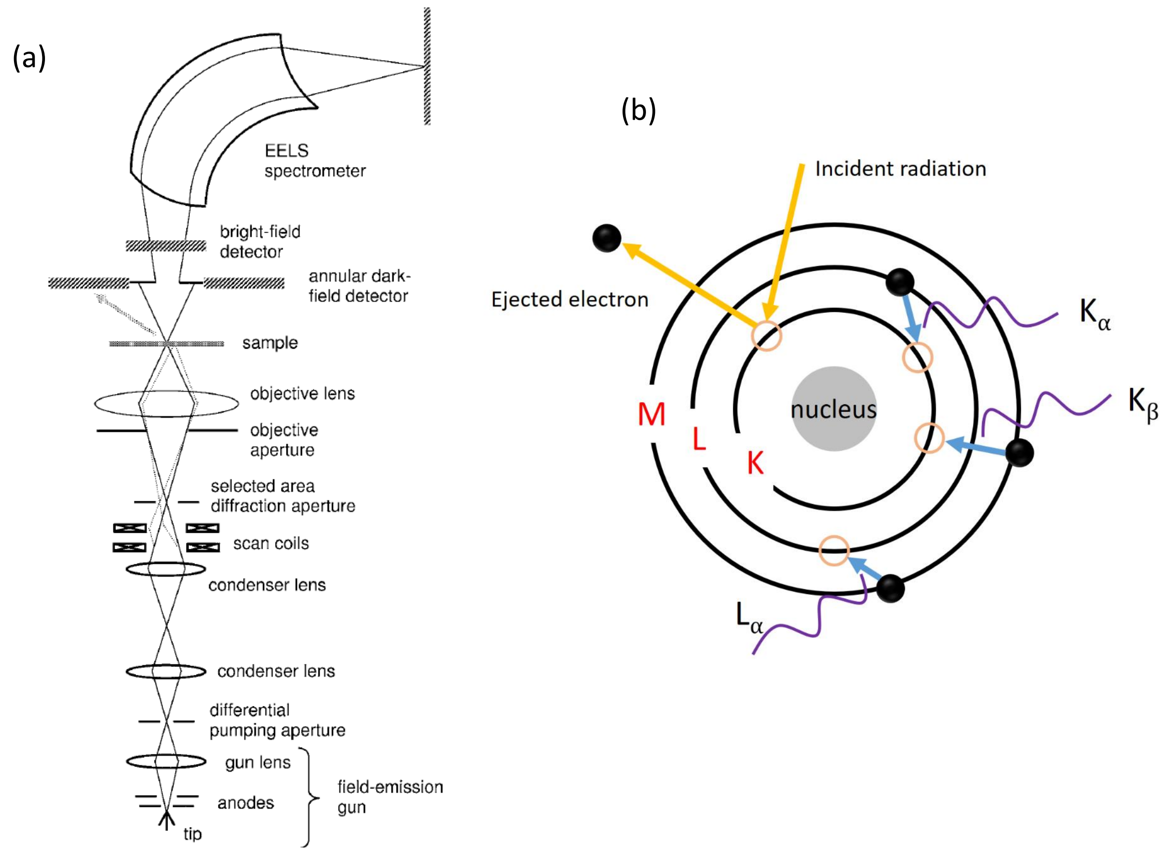

Figure 3.5: (a) Schematics of an STEM instrument, some of the most essential elements and their locations are included. (modified from [45]) (b) Illustration of the mechanism of energy dispersive X-ray analysis (EDX).

Here we introduce two essential concepts in STEM that are mentioned in this thesis.

Bright-field (BF): A bright-field detector is located in the center of the transmitted electron beam. Therefore, only transmitted electrons that have a relatively low angle with respect to the optic axis can be detected.

High-angle annular-dark field (HAADF): As shown in Fig. 3.5a, an annular dark-field detector is away from the optic axis. This detector receives transmitted electrons with high angles to the axis. The high-angle ADF detectors make it possible to get atomic resolution images [46].

The crystalline structure of the SC phase can be nailed down by the STEM facility, while another technique, the energy-dispersive X-ray spectroscopy (EDX), was needed for the elemental analysis. The principle of EDX is that each element has a unique emission spectrum which is irrelevant to the energy of incident electrons or X-rays. Fig. 3.5(b) shows the mechanism of the emission spectrum. An inner shell electron is kicked out by an excitation source, and an electron hole is created. An X-ray will be released if an electron at a higher-energy shell fills the electron hole, and the energy of the X-ray is the difference between the higher-energy shell and the lower energy shell. For example, a K_α ray is radiated when an L shell electron transitions to a vacancy in the K shell. Similarly, one can get K_β, L_α, and so on.

3.3.2 STEM and EDX analysis

A Pd/BST bilayer sample was designed for STEM studies: a 68-nm-thick BST film was epitaxially grown on a sapphire substrate, and 8-nm-thick of Pd was deposited by magnetron sputtering. Fig. 3.6(a) shows the line-scan spectra and a STEM image of the cross-section. The STEM image was taken in the HAADF mode and measured at V_{acc} = 80 kV. Two new phases were observed at the interface between Pd and QLs of BST. The phase close to BST is rich in Pd, while another phase close to the layer of deposited Pd is poor in Pd and Te. The thickness of these two phases is roughly the same, which is about 7 nm. Fig. 3.6(b) shows a dark-field STEM image for the same area in Fig. 3.6(a) but with a higher resolution. The STEM image was taken on the cross-section of Pd/BST bilayer samples. The quintuple-layers (QLs) of BST were epitaxially grown. The left phase has a crystalline structure, but the other phase is amorphous. The crystalline phase consisting of a triple-layer structure is shown in Fig. 3.6(d). We found there are different orientations of the triple layers, and the domain boundary in between is clear. There are at least two kinds of atoms distinguished by the scattering intensities. The crystalline phase was finally identified to be $PdTe_2$ by comparing the crystal structure and the lattice constants to known crystals.

Fig. 3.6(c) shows the CdI2-type crystal structure of $PdTe_2$. Hexagonal Te-Pd-Te triple layers were stacked along the c direction. The lattice constants a and c are 4.04 Å and 5.13 Å, respectively. To obtain the lattice constants in sample 1, a high-resolution STEM image of the $PdTe_2$ was shown in Fig. 3.7(a). Two kinds of atoms in different sizes are clearly observed. Te atoms are heavier than Pd atoms, so Te atoms are larger and brighter. A two-dimensional fast Fourier transform (2DFFT) was applied on a high-resolution STEM image of $PdTe_2$ for the calculation of lattice constants. The lattice constants of $PdTe_2$ in sample 1 are determined to be a= 4.07Å, and c = 5.44 Å. The lattice constant a is consistent with the MBE-grown $PdTe_2$ film very well, while lattice expansion of 6.0 % in the c direction. A possible reason for the lattice expansion is that Bi or Sb atoms intercalate into the van der Waals gap. We have observed such intercalation in Fig. 3.7(a), where an inserted atom is indicated by a thick arrow.

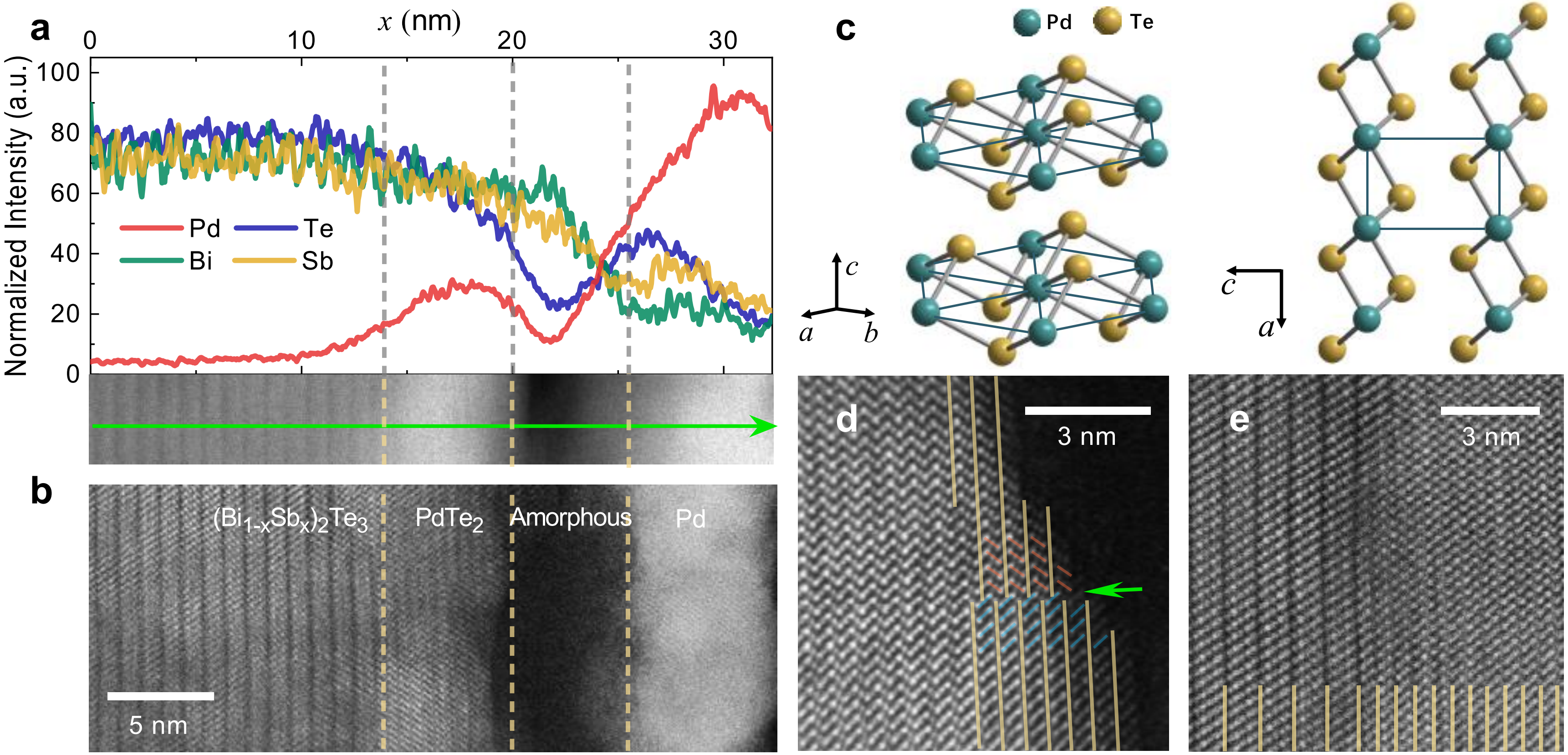

Figure 3.6: EDX and STEM data of sample 1. (a) Upper panel: EDX line-scan spectra across the interface, lower panel: a high-angle annular dark-field STEM image of the cross section of Pd/BST bilayer film. The green arrow shows the EDX scanning line in the upper panel.(b) A high-resolution STEM image of the cross section. Different phases in this image were labeled and separated by dashed yellow lines. (c) Left panel: crystal structure of $PdTe_2$, right panel: the pattern observed when viewed along the b direction. (d) A high-resolution STEM image was taken in the area of $PdTe_2$. In the top loft of the image, the zigzag patterns were seen due to the stacking of different domains in the thickness direction. (e) A high-resolution STEM image across the $PdTe_2$/BST interface. (modified from [27])

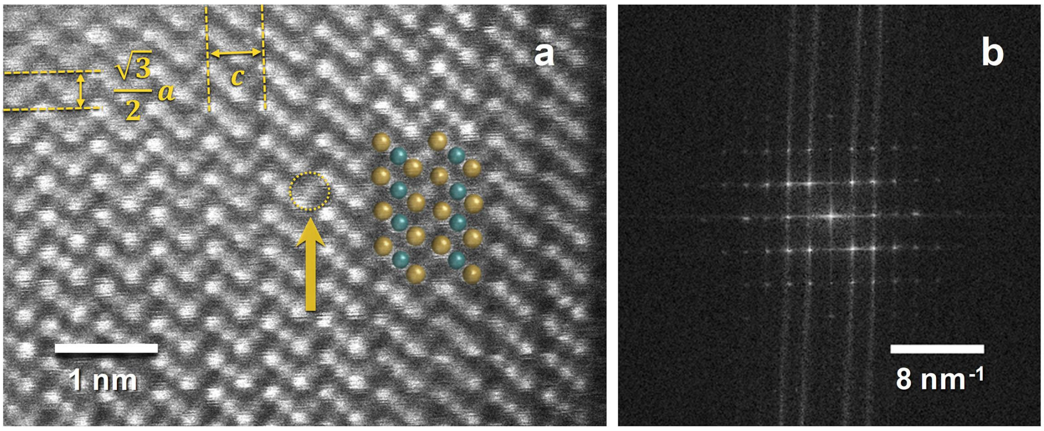

Figure 3.7: STEM data of the self-formed PdTe2 phase. (a) A high-resolution STEM image measured at V_{acc} = 200 kV. The Te and Pd atoms are indicated by dark yellow and dark turquoise colour balls separately. (b) The 2D FFT image of the $PdTe_2$ phase. (modified from [27])

3.3.3 Epitaxial growth of a $PdTe_2$ on the BST

Epitaxial is a kind of crystal growth where the new crystal layers are formed with one or more well-defined orientations with respect to the substrate. Fig.3.6(e) shows a high-resolution STEM image about the interface between BST and crystalline $PdTe_2$. The clear signatures of van der Waals epitaxy growth of $PdTe_2$ were observed. The gap between two adjacent layers of $PdTe_2$ were indicated by vertical yellow lines. Fig. 3.7(a) shows this van der Waals epitaxy growth of $PdTe_2$ with a higher magnification.

3.4 Theoretical background

3.4.1 Josephson equations

In 1962, B.D. Josephson predicted that if two superconductors are linked by a thin insulator (known as the S-I-S Josephson junction), there will be a supercurrent flows through the junction even without voltage applied [47, 48]. Now I briefly derivate the Josephson equations.

ψ_1 and ψ_2 are quantum mechanical wavefunctions in the two superconductors respectively, and ψ_i (i=1,2) denotes as the complex order parameter. This two wavefunctions follows the coupled Schrödinger equations.

$$i\hbar\frac{\partial\psi_1}{\partial t} = \mu_1\psi_1 + K\psi_2 \tag{3.1}$$

$$i\hbar\frac{\partial\psi_2}{\partial t} = \mu_2\psi_2 + K\psi_1 \tag{3.2}$$

where μ_i is the chemical potential of the superconductor i, and K is the coupling coefficient between two superconductors.

A solution of Eq. 3.2 can be written as:

$$\Psi_i = \sqrt{n_i}e^{i\phi_i}, \tag{3.3}$$

where n_i is the density of Cooper pairs and θ_i is the phase. Substituting Eq. 3.3 into Eq. 3.2 we can get:

$$\hbar\frac{\partial n_1}{\partial t} = 2\,K\sqrt{n_1 n_2}\sin(\phi_2 - \phi_1) = -\hbar\frac{\partial n_2}{\partial t} \tag{3.4}$$

$$-\hbar\frac{\partial}{\partial t}(\phi_2 - \phi_1) = \mu_2 - \mu_1 \tag{3.5}$$

The time derivative of the density of Cooper pairs $\frac{\partial n_1}{\partial t} = -\frac{\partial n_2}{\partial t}$ gives the supercurrent I. μ_2-μ_1 =2eV where V is the voltage difference between the junction. We can obtain the Josephson equations:

$$I = I_0 \sin\phi \tag{3.6}$$

$$\frac{d\phi}{dt} = \frac{2eV}{\hbar} \tag{3.7}$$

where I_0=2 $K\sqrt{n_1 n_2}/\hbar$ and ϕ is defined as ϕ_2-ϕ_1.

3.4.2 The Fraunhofer pattern

If we apply a perpendicular magnetic field on SIS JJ, the phase difference will change to:

$$\phi \rightarrow \phi_0 + 2\pi\frac{\Phi}{\Phi_0} \tag{3.8}$$

Where Φ_0 is the magnetic flux quantum. The additional term $\Phi = B \times S$ is the flux through the junctioin, where S is the junction area. According to the Josephson equations, the integral current across the junction is:

$$I = \int_S J_0 \sin(\phi) dS \tag{3.9}$$

and the critical current I_C is the maximum value of I. Substituting Eq. 3.8 into Eq. 3.9 we can get:

$$I_c = I_c(0) \left| \frac{\sin(\pi\Phi/\Phi_0)}{\pi\Phi/\Phi_0} \right| \tag{3.10}$$

The diffraction pattern described by Eq. 3.10 is the well known Fraunhofer pattern as shown in Fig. 3.8

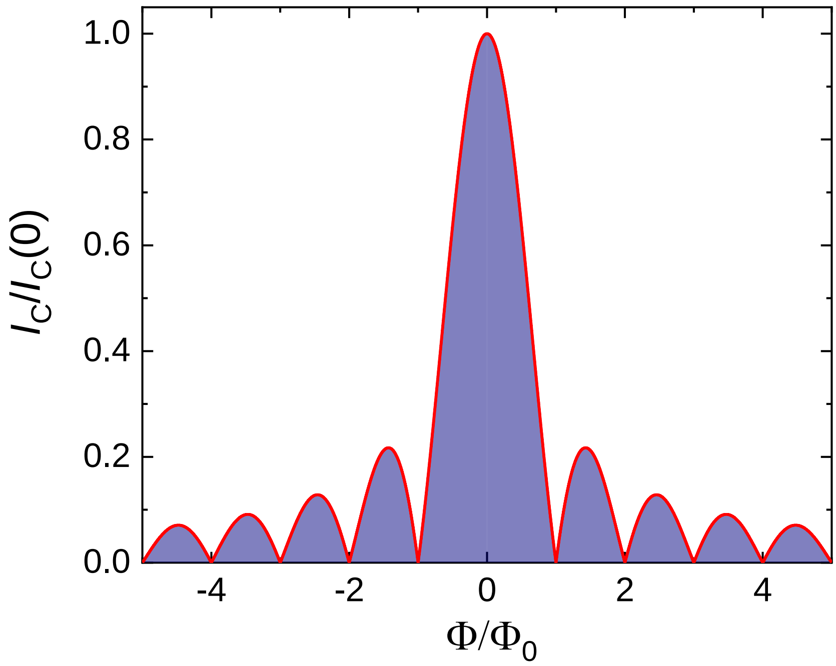

Figure 3.8: The normalized Josephson critical current $I_c/I_C(0)$ as a function of magnetic flux through the junction Φ/Φ_0.

3.4.3 Andreev reflections

In BCS theory the density of states (DOS) for quasi-particles are [49]:

$$\frac{N_s(E)}{N(0)} = \begin{cases} \frac{E}{(E^2-\Delta_0^2)^{1/2}} & |E| > \Delta_0 \\ 0 & |E| < \Delta_0 \end{cases} \tag{3.11}$$

Now let us consider a superconductor-metal-superconductor (SNS) JJ. As shown in Fig. 3.9, when an electron with a energy $E < \Delta$ from the normal metal (N) impinge to the superconductor, the electron will be reflected back into the metal because there is no possible states in

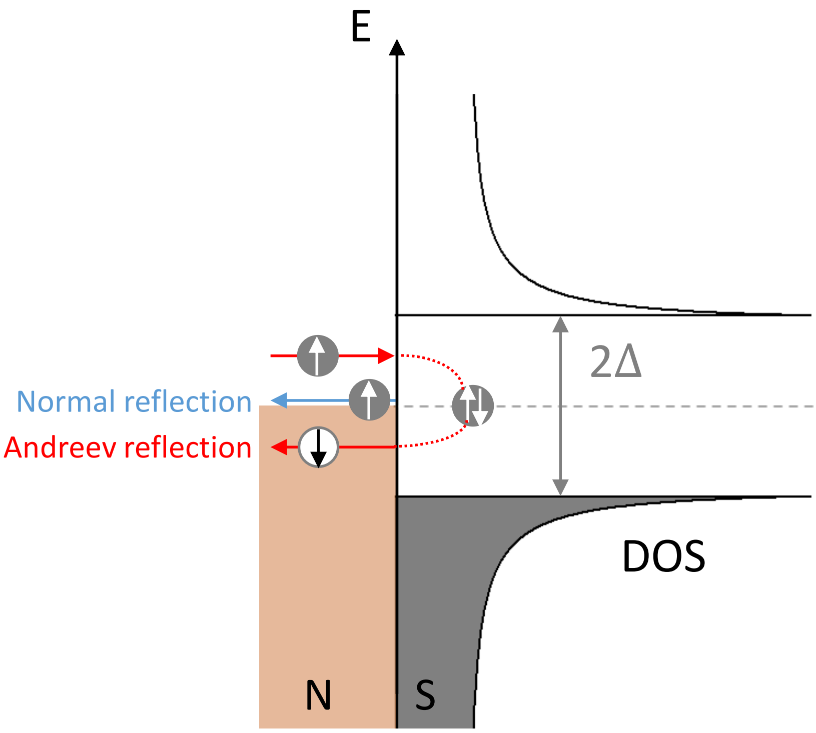

Figure 3.9: Right-hand side shows the DOS for quasi-particles as a function of energy (E) in the superconductor with a superconducting gap Δ. Two kinds of reflections happen in the N-S interface. One is the normal reflection that an electron from normal metal is reflected back into the metal. The other one called Andreev reflection that an electron from N is reflected as a hole with opposite spin and momentum, meanwhile, a Cooper pair formed in the superconductor.

the superconductor. However, two electrons effectively can transmit into the superconductor when the incident electron in N is retro-reflected as a hole. The reflected hole has opposite momentum and spin compared to the incident electron due to the momentum conservation and spin conservation. Besides, the reflected hole carries phase information of the incident electron:

$$\phi_h = \phi_e + \arccos(E/\Delta) + \phi_s \tag{3.12}$$

where ϕ_h, ϕ_e and ϕ_s are the hole phase, the electron phase and the superconductor phase, respectively [50]. This process is known as the Andreev reflection [51], as sketched in Fif. 3.9.

3.4.4 The Blonder–Tinkham–Klapwijk (BTK) theory

The Blonder–Tinkham–Klapwijk (BTK) theory [52] describes the electron behaviors on the NS interface. It is derived for zero temperature and the normal metal and superconductors are assumed to be ballistic. A dimensionless parameter Z represents the barrier strength between N and SC, the probability for Andreev reflection is 1 when $Z = 0$. We know there are four different processes: Andreev reflection (A), normal reflection (B), transmission without branch crossing (C) and transmission with branch crossing (D). The corresponding probabilities are shown in table 3.2, where the factors u_0, v_0 and γ are defined by equations:

$$u_0^2 = \frac{1}{2}\left(1 + \frac{\sqrt{E^2 - \Delta_0^2}}{E}\right) \tag{3.13}$$

$$v_0^2 = 1 - u_0^2 \tag{3.14}$$

$$\gamma^2 = \left[u_0^2 + Z^2\left(u_0^2 - v_0^2\right)\right]^2 \tag{3.15}$$

	A	B	C	D
$E < \Delta$	$\frac{\Delta^2}{E^2+(\Delta^2-E^2)(1+2Z^2)^2}$	$1 - A$	0	0
$E > \Delta$	$\frac{u_0^2 v_0^2}{\gamma^2}$	$\frac{(u_0^2-v_0^2)^2 Z^2(1+Z^2)}{\gamma^2}$	$\frac{u_0^2(u_0^2-v_0^2)(1+Z^2)}{\gamma^2}$	$\frac{v_0^2(u_0^2-v_0^2)Z^2}{\gamma^2}$

Table 3.2: The probability of transmission and reflection coefficients. Where A, B, C and D are the probability of Andreev reflection, normal reflection, transmission without branch crossing and transmission with branch crossing, respectively. (modified from [52])

In Fig. 3.10, the probalities of A ,B , C and D as a function of energy are plotted for three values of Z. For the energy is smaller than Δ only Andreev reflections occur when Z = 0, while only normal reflections happen when Z increasing to 3.

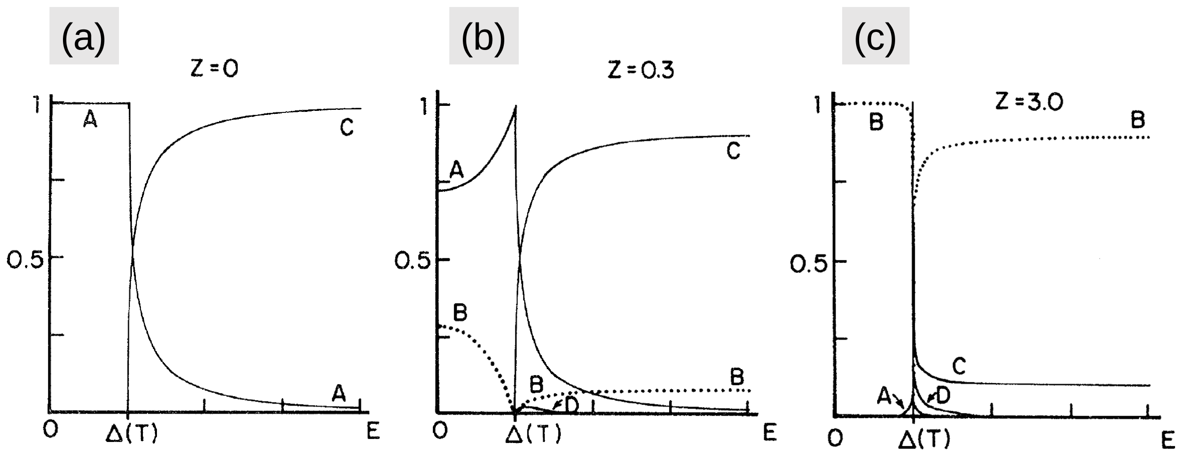

Figure 3.10: Probalities of reflections and transmissions for three different barrier strength. (modified from [52])

Andreev reflection contributes to the net current when a voltage is applied, resulting in an excess current I_e. In fact, the excess current is due to the Andreev reflection involving a charge transfer of 2e. And I_e can be written as [52]:

$$I_e = \frac{1}{eR_N[1 - B(\infty)]} \times \int_0^\infty [A(E) - B(E) + B(\infty)]dE \tag{3.16}$$

where R_N is the normal state resistence and $B(\infty)$ is the probability of normal reflection at very high energy. The Eq. 3.16 establishes a relation between I_e and Z where A and B are related to the barrier Z. Octavio, Tinkham, Blonder and Klapwijk (OTBK) [53] did calculations on the $I - V$ characteristics according to the BTK theory and predicted exhibition of subharmonic gap structures. Flensberg $etal$[54] corrected the calculations on the basis of OTBK model. And a quantitative description of I_e and Z is shown in Fig. 3.11 [54, 55]. Then the NS interface transparency (τ) is obtained by:

$$\tau = \frac{1}{1 + Z^2} \tag{3.17}$$

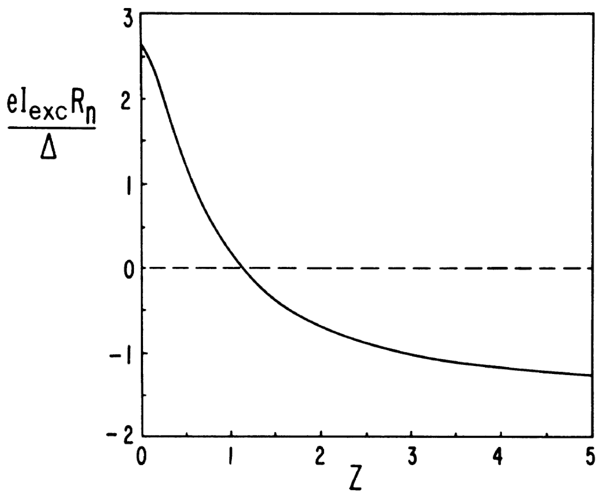

Figure 3.11: The normalized excess current eI_eR_N/Δ as a function of the barrier strength Z. (modified from [54])

3.5 A Josephson junction device

The idea for engineering topological superconductivity in hybrid structures based on TI was conceived by Fu and Kane [7]. The structure of a hybrid device is shown in Fig. 3.12, two *s*-wave superconductors separated by a small gap are located on the TI surface. The key idea of the Fu-Kane proposal is to induce superconductivity among electrons that are spin-nondegenerate ("spinless"). The "spinless "electrons can be provided by the 3D TI surface states where the spin degree of freedom is frozen due to spin-momentum locking [56–58].

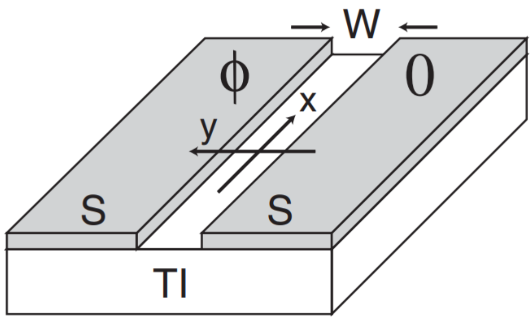

Figure 3.12: The sketch of a S-TI-S planar Josephson junction. A nonchiral one-dimensional wire for Majorana fermions was formed in such a junction. (modified from [7])

One of the obstacles for realizing proximity-effect-induced superconductivity in TI is the dirty interface between SC and TI. Usually, the surface of the TI can be polluted by oxygen and water when it is exposed to air. The surface can also be smudged by resist residues. An advantage of our self-formed superconductor is that the interface is beneath the TI surface. So it is immune to such pollution naturally.

To chararcterize the BST films are proximitized by the self-formed $PdTe_2$ superconductor, a Josephson junction device (device A) was fabricated. The SEM image of this device is shown in Fig. 3.3(a). To make the spatial distribution of the JJ more uniform, the width of the JJ is as wide as 3 μm. Since we know the wide SC film can have the flux-jump problem, the SC electrodes neighboured the JJ were designed to be narrow. To understand these flux jumps, we did a simple calculation. The magnetic flux quantum $\Phi_0 = h/(2e) \approx 2.07 \times 10^{-15}$ Wb. To create a flux in an area of 1 μm^2, one need to apply a magnetic field of $2.07 \times 10^{-15}/1\ \mu m^2 \approx 20$ mT. If the area is circular, the radius is about 560 nm. It suggests that the SC electrodes near the JJ should not be wider than this value. At last, the dimensions of the JJ are optimized.

3.5.1 Superconducting transition of device A

The device A was measured in a dry dilution refrigerator (Oxford Instruments Triton200) with a base temperature of ~ 20 mK. The Junction resistance of device A as a function of temperature is shown in Fig. 3.13. A sharp drop of resistance is observed at ~ 0.90 K. This drop corresponds to the superconducting transition of the self-formed $PdTe_2$ layer beneath the Pd electrode, and

0.90 K is the T_C of $PdTe_2$. As the temperature further decrease, a broad transition continues until T $\lesssim$ 150 mK. The broad transition is associated with the onset of Josephson coupling inside the junction. Zero resistivity at lower temperature was reached, which indicates that Josephson coupling between the two SC electrodes is established.

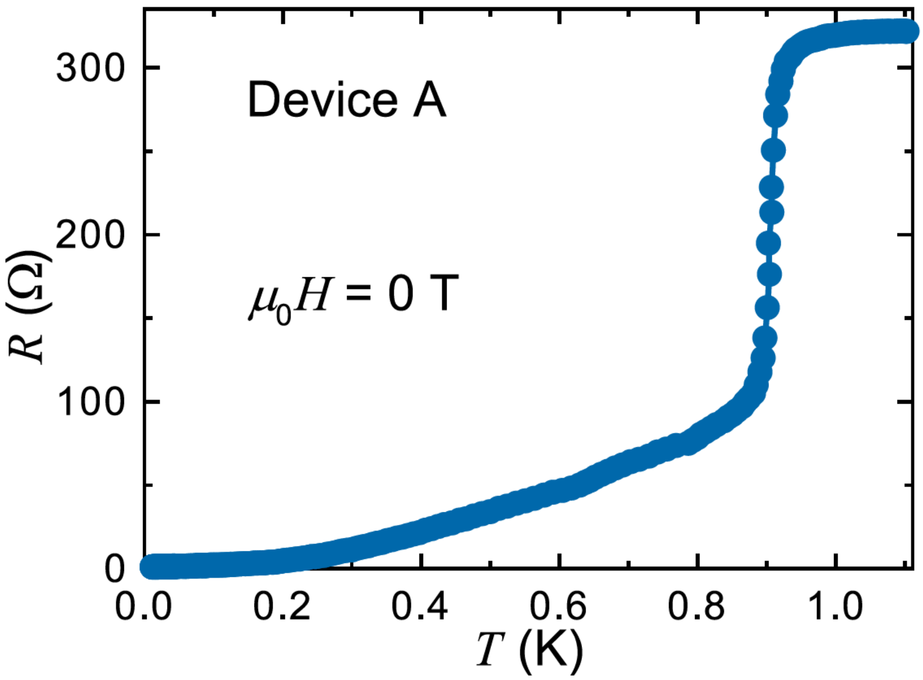

Figure 3.13: Temperature dependence of the zero-bias resistance of device A, measured at zero magnetic field. (modified from [27])

3.5.2 The Fraunhofer-like pattern

In Fig. 3.14, we present a two-dimensional plot of differential resistance (dV/dI) in the dc current bias (I_{dc}) vs. B plane. The zero-resistance state was indicated by the dark-blue colour. One can see that the critical current I_C is modulated by magnetic field, and the modulation of I_C roughly follows a Fraunhofer-like pattern. But it is not the standard pattern which is described by Eq. 3.10. We can obtain a period($\mu_0 \Delta H$) of $\approx$ 2.8 mT from the first lobe, which is the only standard one. While, the expected period $\mu_0 \Delta H_{cal} = \Phi_0 / S$ = 6.89 mT, where the area $S = L \times W$ = 0.3 μm^2. The expected period is about two and half times larger than what we observed. There are two reasons to increase the effective area, namely the London penetration depth of and the flux-focusing effect [59, 60]. The London penetration depth makes the effective length of the junction longer. And due to the diamagnetism of the superconductors, a portion of the magnetic flux will be expelled from the superconductors into the junction. So the actual magnetic flux in the junction can be larger.

As shown in Fig. 3.14, broadening, missing ,or drastically suppressed lobes are observed. The anomalous features of the Fraunhofer patterns in TI-based Josephson junctions have been reported before[30, 61–64]. The Fraunhofer patterns can deviate from a standard pattern if

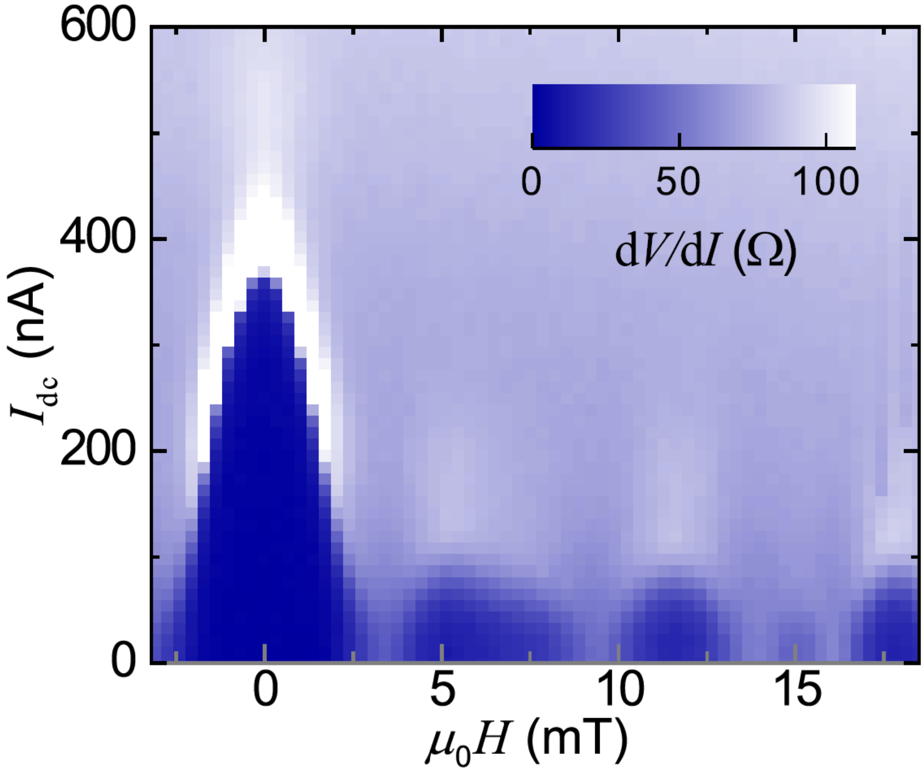

Figure 3.14: Two-dimensional plot of differential resistance dV/dI as a function of magnetic field B and d.c. current bias I_{dc}, measured at T = 8 mK in device A. (modified from [27])

there are Majorana modes formed in the junction. For example, the odd-numbered (first, third, fifth, etc.) lobes in the Fraunhofer patterns are suppressed due to the 4π periodicity [65], and the minimum of the first lobe is nonzero in the Josephson junctions where 1D Majorana modes are created [66].

However, there is no solid evidence that there are Majorana modes that appeared in the above papers [61–64], and their theoretical model does not explain the suppression of some particular lobes, even the even-numbered lobes. S. Ghatak *et al.*. attribute the anomalous Fraunhofer patterns to the inhomogeneous supercurrent distributions in the Josephson junctions without topologically-non-trivial phases [30]. They reconstruct the inhomogeneous supercurrent distributions by a series of discrete supercurrent densities along the width of the junction. The maximum entropy method in a Monte Carlo algorithm was employed to fit the data. The missing and suppressed lobes are well explained by their model. We did the same fitting on the anomalous Fraunhofer pattern of device A [1]. The red dashed line in the inset of Fig. 3.15 is the fitting curve. The corresponding inhomogeneous current density distribution is plotted by the red curve in Fig. 3.15, where the x-axis is the edge of the junction along the transverse direction.

The inhomogeneous supercurrent distributions is a probable origin of the anomalous

[1] Dr. Oliver Breunig did the fitting

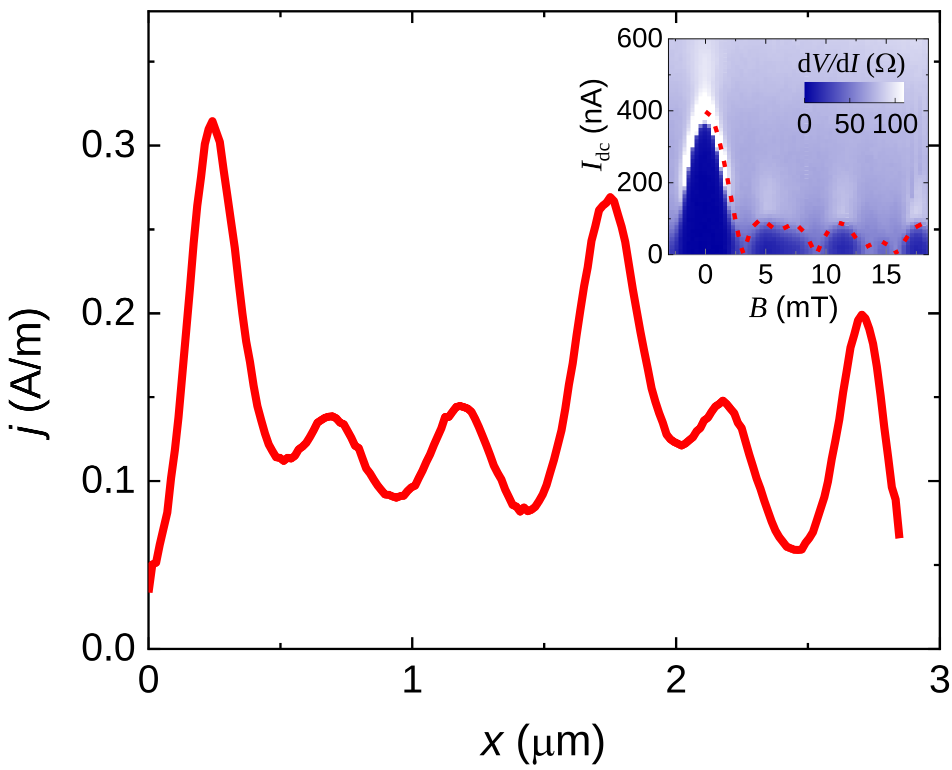

Figure 3.15: The inhomogeneous current density distribution which was obtained from the fittings. Inset: A fitting on the anomalous Fraunhofer pattern of device A.

Fraunhofer pattern in device A. We have studied the self-formed $PdTe_2$ along the c direction, while there is no STEM data about the Pd diffusion along the horizontal direction. So we have no idea how the $PdTe_2$ formed inside the junction's area. We leave this as an open question for future studies. If the Pd diffuses into the gap of the junction with different length, then the length of the Josephson junction varies along the transverse direction. In addition to this, the STEM images in Fig. 3.6(b) and (d) show the inhomogeneity of $PdTe_2$. This means the thickness of $PdTe_2$ was not well defined. Both the different lengths of the junction and the different thickness of $PdTe_2$ can give rise to the inhomogeneous supercurrent distributions.

3.5.3 Current–voltage characteristic of device A

Fig. 3.16 shows a dc current–dc voltage (I–V) curve of device A, measured at T = 8 mK and zero magnetic field. The Josephson supercurrent with a critical current $I_C(JJ) = 0.39$ μA appeared. There is no voltage drop on the junction when applied current is lower than $I_C(JJ)$. The critical current was more clearly to be identified in Fig. 3.17, where the corresponding peak is indicated by a red arrow in the differential resistance vs. dc bias current plot.

The horizontal jump starting from 1.1 μA is due to the superconducting critical current of the $PdTe_2$ electrodes being exceeded. The evidence is that the linear I–V curve at high V_{dc} reaches an asymptote that goes through the origin. One can judge that now device A is in the normal state that followed Ohm's law. As shown in Fig. 3.17, a blue arrow located at

1.1 μA indicates the critical current of $PdTe_2$ ($I_C(PdTe_2)$)electrodes, which is the same as the $I_C(PdTe_2)$ obtained from $I-V$ curve. There are some features between 1.1 μA and 1.9 μA due to the superconducting transition of $PdTe_2$. Above 1.9 μA, the normal state resistance of the junction is kept constant, as shown in Fig. 3.17.

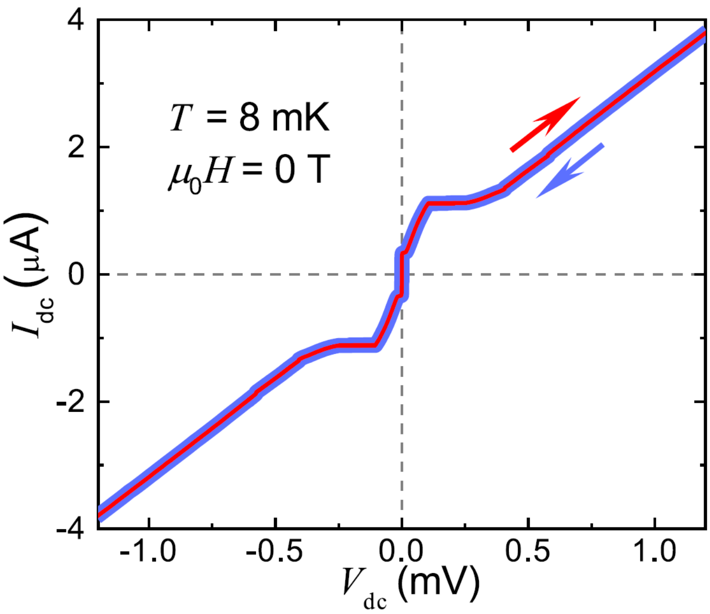

Figure 3.16: Dc current–dc voltage characteristic of device A. Forward and reverse sweeps are indicated by red colour and blue colour, respectively. (modified from [27])

One of our goals is to acquire the knowledge of junction transparency to check whether the technique of self-formed $PdTe_2$ is promising for engineering a topological superconductivity device. According to the OTBK theory, the junction transparency can be estimated based on the excess current. The excess current is estimated from the intercept of a linear fit to the linear $I-V$ region when V_{dc} goes beyond $2\Delta_{SC}/e$ where no Andreev reflections anymore. Unfortunately, the superconductivity in the superconductor electrodes of device A is killed at a very low dc voltage $V_{dc}(JJ) \approx 0.11$ mV. As we know the transition temperature of $PdTe_2$ electrodes in device A is 0.90 K (Fig. 3.13). The superconducting gap $2\Delta(PdTe_2)$ can be estimated from BCS theory: $2\Delta(PdTe_2) = 3.5K_BT_C \approx 0.27$ meV. The $V_{dc}(JJ)$ is much lower than $2\Delta(PdTe_2)/e$.

Usually, in a high-transparency Josephson Junction device some subharmonic peaks of multiple Andreev reflections (MAR) are expected [30, 67]. The signatures of MAR can be obtained in the plot of differential conductance as a function of bias voltage. The dI/dV-*vs*-V_{dc} is plotted in Fig. 3.18. Even though the superconducting state was killed from 0.11 mV, there are two weak features at ~ 0.03 mV and ~ 0.08 mV which could be related to the multiple Andreev reflections. If the subharmonic peaks' position and the inverse peak index have a linear relation, one can confirm that they stem from subharmonic peaks of MAR. However, we can not do a linear fitting in device A for the lack of numbers of peaks in Fig. 3.18.

3.5.4 Stewart-McCumber parameter of device A

As shown in Fig. 3.16, both upward (red arrow) and downward (blue arrow) sweeps of bias voltage in device A were performed. The two curves are overlapped completely. There is no hysteretic behavior in the $I-V$ curve, suggesting that the junction is in the overdamped region.

According to the RCSJ model [68, 69], the Stewart-McCumber parameter [70] β_C is much smaller than one when the $I-V$ curves are non-hysteretic. The β_C is defined as $2\pi I_c R_N^2 C/\Phi_0$, where C is the shunt capacitance of the junction, and Φ_0 is the flux quantum. The critical current I_C and normal-state resistance R_N are 0.39 μA and 110 Ω, respectively. As we can not obtain the R_N by the fitting the $I-V$ curve, R_N is taken right after the first superconducting transition in the $R-T$ curve plotted in Fig. 3.13. In the planar Josephson junction of device A, the shunt capacitance C comes from the capacitor formed between the two Pd electrodes. This capacitor is a parallel-plate capacitor. The shunt capacitance C can be estimated from the formula $C = \epsilon_0 wd/l \approx 10^{-17}$ F, where w, d, and l are the width of the junction,the thickness of the Pd electrodes, and the length of the junction. According to the STEM result, we know that the thickness of the Pd layer becomes thinner due to the diffusion of Pd. However, the order of the calculation does not change. Put all the values in the formula, the Stewart-McCumber parameter of device A $\beta_C \sim 10^{-4} \ll 1$. The small β_C is consistent with the non-hysteretic $I-V$ curves of the Josephson junction in the overdamped limit.

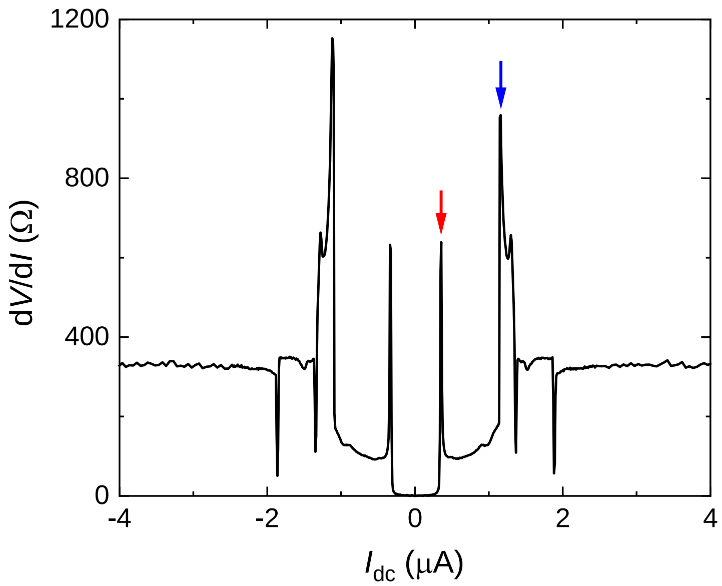

Figure 3.17: Differential resistance as a function of bias current. The critical current of the Josephson junction and the $PdTe_2$ electrodes are indicated by the red arrow and the blue arrow, respectively.

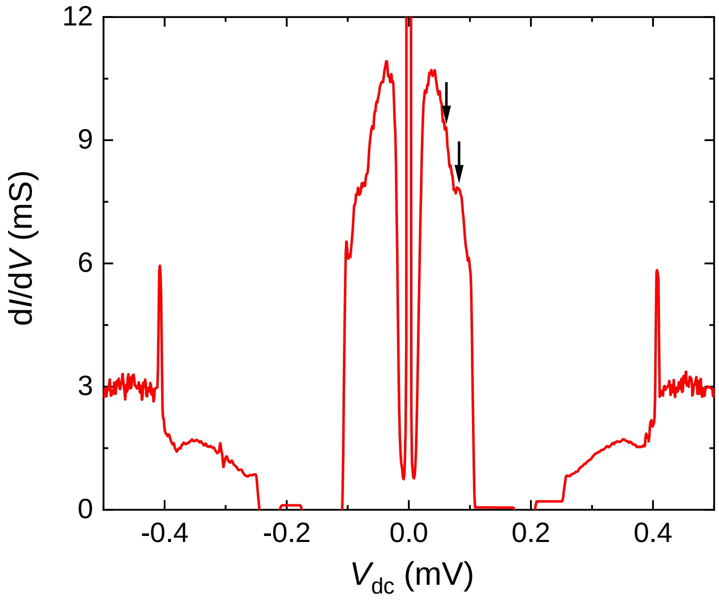

Figure 3.18: Differential conductance as a function of bias voltage of device A is obtained by the differential of $\mathrm{I}-\mathrm{V}$ function.

3.6 A SQUID device

Even though Josephson supercurrent was induced in device A, the excess current can not be obtained because of the small critical current in narrow SC electrodes. So we have to increase the width of SC electrodes. At the same time, flux jumps should also be considered. We designed some antidots inside the SC electrodes so that there is no enough area to trap a flux. Fig. 3.19 shows the SEM images of devices after unsuccessful lift-off processes. We try different methods to do the lift-off, such as ultrasonic treatment and keep stirring of acetone, but none of them works. We give up this design after a period of hard work. Meanwhile, we found that a SQUID is an excellent choice. The effective area of a SQUID is about 20 times larger than a Josephson junction. The magnetic field is 20 times smaller for measuring Fraunhofer patterns. So that we can have a much wider SC electrode but without flux trapped during measurement. The SEM image of the SQUID device is shown in Fig. 3.3(b).

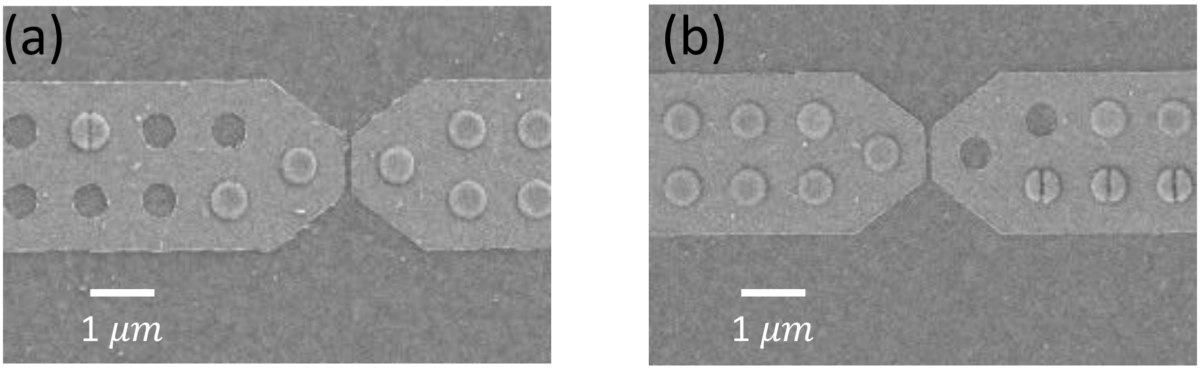

Figure 3.19: SEM images of superconductor electrodes with antidots. The diameter of the dots is about 550 nm. (a) Lift-off was done in an ultrasonic acetone bath. (b) Lift-off was done in an acetone bath, and the acetone was churned.

3.6.1 Superconducting transition of the SQUID

As shown in Fig. 3.20, there is also a sharp transition in the $R(T)$ curve in device B. The T_C of $PdTe_2$ is ≈ 0.7 K, which is a little bit smaller than the T_C in device A. That's may due to the thickness of the self-formed $PdTe_2$ layer in device B being thinner. The broad transition lasts even to the base temperature of the dilution fridage, and the finite resistance at T = 8 mK is about 25 Ω. The non-zero resistance is probably caused by noise. A SQUID device is very susceptible and sensitive. It can sense a tiny magnetic field and can pick up a very weak noise. The $I - V$ curve (Fig. 3.22) of device B shows a clear junction critical current, which is evidence that the junctions are essentially in zero-resistance state at T = 8 mK in zero magneti field.

3.6.2 A typical SQUID-type oscillations in device B

Fig. 3.21 shows the differential resistance of the SQUID as a function of both magnetic field and dc current bias. A clean SQUID-type oscillation is observed in device B. The zero-resistance

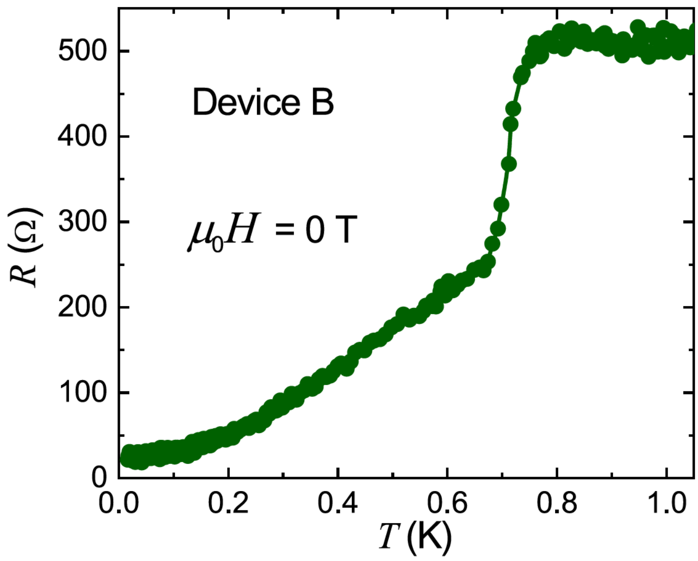

Figure 3.20: Temperature dependence of the zero-bias resistance of device B, measured at zero magnetic field. (modified from [27])

superconducting state corresponds to the dark-blue colour. The white colour indicates the highest differential resistance when one sweeps the bias current, and corresponds to the critical current at the fixed magnetic field.

The field dependence of critical current of a SQUID is described by the formula: $I_C(SQUID) = 2I_0 \cdot |\cos(\pi\Phi_{(SQUID)}/\Phi_0)|$ [71], where $\Phi_{(SQUID)}$ is the flux through the SQUID loop. The period of the SQUID-type oscillation is 0.36 mT that can be diagnosed from Fig. 3.21. The effective area of the SQUID was marked by the green dashed line in the SEM image of device B(Fig. 3.3). As mentioned above, because of the diamagnetism of the superconductor, half of the magnetic flux in the superconductor electrodes is compressed into the SQUID loop. The width and length of the green rectangle are 2 μm and 3 μm, respectively. Thus, one can calculate the expectant period $\mu_0\Delta H_{cal}(SQUID) = \Phi_0/S_{SQUID}$ = 0.34 mT, which is consistent with the period we measured.

In fact, the envelope of the SQUID-type oscillations is modulated by the Fraunhofer diffraction patterns of the Josephson junctions that make up the SQUID [72]. However, there is no signature about the modulating Fraunhofer patterns in Fig. 3.21. The SQUID has two identical Josephson junctions with the length of 50 nm and the width of 600 nm. The period of the Fraunhofer patterns of the two junctions is Φ_0/S_{JJ} = 68 mT, which is 200 times larger than the period of SQUID oscillations. That is why there is no Fraunhofer patterns that observed in such a small range of the magnetic field.

3.6.3 Current–voltage characteristic of device B

Fig. 3.22 shows the current–voltage characteristic of device B, taken at the base temperature without applying a magnetic field. Zoom-in of the $I - V$ characteristics in the low-bias region

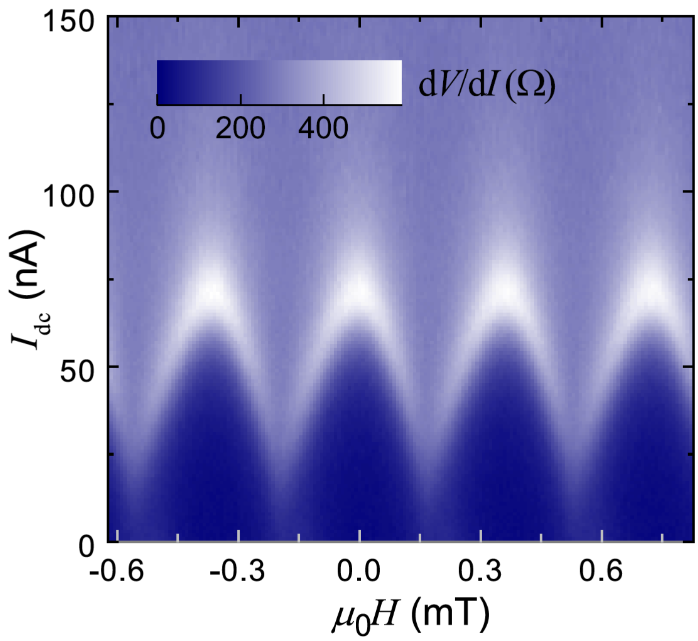

Figure 3.21: Two-dimensional map of the dV/dI as a function of I_{dc} and B, measured at T = 8 mK in device B. (modified from [27])

was shown in the inset of Fig. 3.22. Zero-resistance state occurs when I_{dc} is below the critical current $I_{C(SQUID)}$. The $I_{C(SQUID)}$ = 0.07 μ A is indicated by the blue arrow. Above the critical current of the SQUID, a finite voltage starts to develop, and the $I - V$ curve is nonlinear until V_{dc} is smaller than ~ 0.21 mV. While the $I - V$ curve becomes linear when V_{dc} increase continuously.

Compared to the Josephson junction device A, the linear $I - V$ curve was obtained without killing the superconductivity of the $PdTe_2$ layer. The superconducting gap of $PdTe_2$ can be estimated based on the BCS theory, where $\Delta_{PdTe_2} = 1.75\ k_B T_C \approx 0.105$ mV. The multiple Andreev reflection was expected inside the energy gap of $2\Delta_{PdTe_2} \approx 0.21$ mV. In order to study the quasiparticle processes inside the SQUID, dc bias voltage dependence of the differential conductance is shown in Fig. 3.23. However, there are no subharmonic peaks appeared inside $2\Delta_{PdTe_2}$ in Fig. 3.23. Only one kink is seen at V_{dc} = 0.2 mV, which is close to the $2\Delta_{PdTe_2}/e$. The kink is marked by the black arrow. It is probably related to the primary Andreev reflection, which corresponds to V_{dc} of $2\Delta_{SC}/e$. Another kink indicated by the blue arrow was shown at 0.33 mV, which is beyond the $2\Delta_{PdTe_2}/e$. Such anomalous behaviors has been reported in a semiconductor-superconductor hybrid system by M. Kjaergaard $etal.$ [73]. This can be explained by the geometry of the planar Josephson junctions, before undergoing the Andreev reflections, several times of the quasiparticles scattering at the superconductor interface happened [74, 75]. What's more, at a much higher bias voltage, a series of periodic peaks occurred. We have not understood the origin of such periodic peaks. More experiments are needed for future studies. For example, the temperature dependence of the subharmonic peaks can help us to tell whether these features are related to the superconductivity or not.

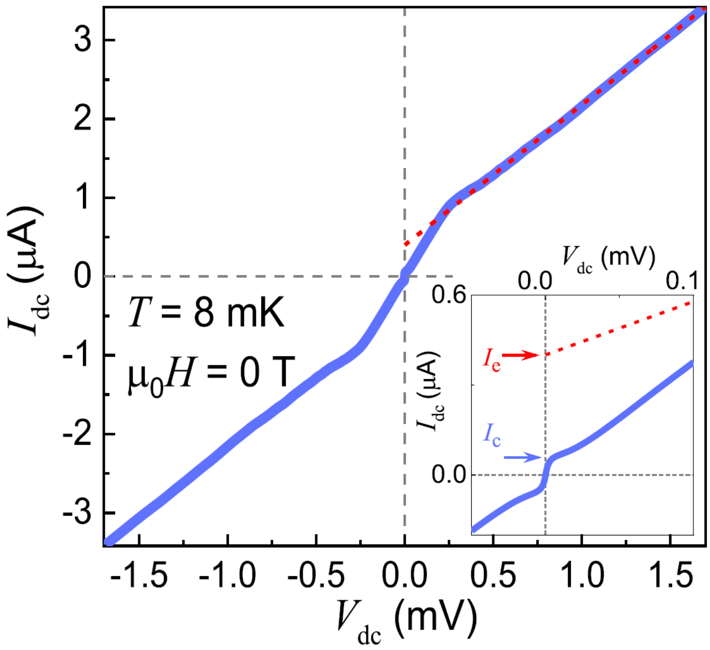

Figure 3.22: Current-voltage characteristics of device B, measured at 8 mK and zero magnetic field. Inset: zoom in of the $I-V$ characteristics in low-bias region. (modified from [27])

3.6.4 Estimation of the transparency of device B

According to the OTBK theory [53, 54], the transparency can be obtained by the ratio of eI_eR_N/Δ_{SC}. I_e and R_N are the excess current and the normal-state resistance of Josephson junctions, respectively. To get the values of I_e and R_N, a linear fit was performed for the $I-V$ curve in high bias region where $eV_{dc} \gg 2\Delta_{PdTe_2}$. The linear fitting curve was plotted by the red dashed line in Fig.3.22. The inverse of the slope of the fitting curve gives the normal-state resistance of the SQUID $R_N(SQUID)$ = 562 Ω. The excess current $I_{e(SQUID)}$ = 0.40 μA was obtained from the y-intercept, as shown in the inset of Fig. 3.22. The non-zero y-intercept indicates that the $PdTe_2$ electrodes remain in the superconducting state.

As the clear SQUID-type oscillation shown in Fig. 3.21, we can assume that the two Josephson junctions in the SQUID are identical. And the two junctions are joined in parallel, so the resistance of junctions is two times the resistance of the SQUID, while the excess current of junctions is half of the SQUID. The I_eR_N product for each junction is obtained as $I_e(JJ)R_N(JJ)$ = $(I_e(SQUID)/2)\cdot(2R_N(SQUID)) = I_e(SQUID)R_N(SQUID) \approx 0.23$ mV. Together with the superconducting gap, the ratio of $eI_e(JJ)R_N(JJ)/\Delta_{PdTe_2} \approx 2.19$. As shown in Fig. 3.11, the relation between the ratio of I_eR_N/Δ and the barrier strength Z is numerically calculated. The I_eR_N/Δ of 2.19 gives a barrier strength $Z \approx 0.19$. The transparency of the Josephson junction is calculated as $\tau = 1/(1+Z^2) \approx 0.96$, which is among the highest transparency of the Josephson junctions based on TI have been reported [30, 67, 76–80].

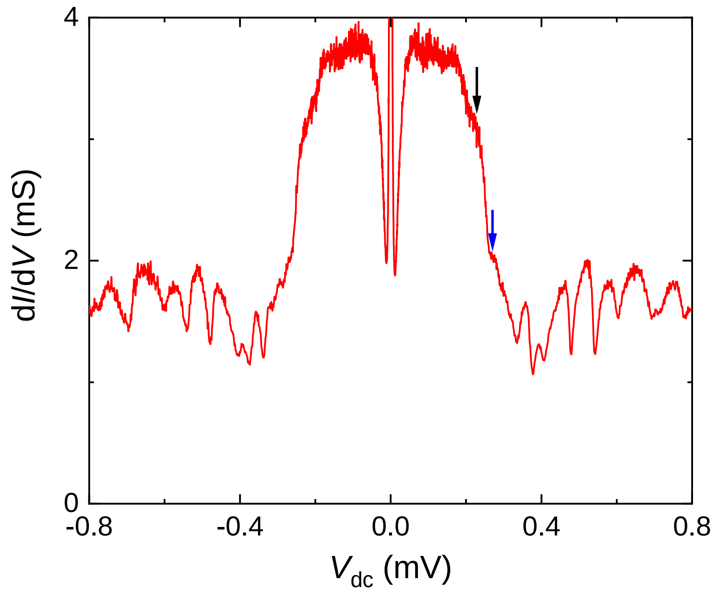

Figure 3.23: Plot of differential conductance as a function of the bias voltage obtained in device B.

3.7 Discussion of the data

According to the EDX analysis (see Fig. 3.5(a)),in the amorphous region, the normalized intensity of Pd and Te have the minimum value. However, the normalized intensity of Sb changes smoothly and the intensity of the Bi even have a small peak in this region, which suggests that the Bi and Sb atoms were accumulated from the $PdTe_2$ phase. There are some Bi and Sb atoms incorporated as intercalant in the crystalline $PdTe_2$ phase.

There is a concern that the homogeneity of superconductivity in the $PdTe_2$ layer and the topological surface states of BST could be affected by the Bi and Sb intercalation. The sharp superconducting transition of the Pd/BST bilayer film (see Fig. 3.4(a))confirms that superconductivity in the $PdTe_2$ layer is homogeneous, otherwise there should be several transitions or the transition should broad. The topological surface states of BST are topologically protected by the bulk band structure of BST. Therefore, the possible topological superconductivity at the surface of the BST film will not be destroyed by the Bi/Sb intercalation.

The superconductivity in the $PdTe_2$ layer is homogeneous but the critical current of the $PdTe_2$ electordes in device A is only about 1 μA. Such a small critical current was problematic for the excess current estimation. The junction transparency can not be characterized because the superconductivity in electrodes is lost before reaching the linear $I-V$ region. The reason of the small critical current density for the self-formed $PdTe_2$ layer is due to the low bulk carrier density of $PdTe_2$, which is $\sim 5.5\times 10^{21}$ cm^{-3} [38]. In contrast, the widely used superconductor Al has a bulk carrier density of $\sim 1.8\times 10^{23}$ cm^{-3} [81]. For the purposes of making promising devices in the future, we need to enlarge the critical current of $PdTe_2$. To avoid the flux jumps we can not ennlarge the critical current by making a wider SC electrode. However, this potential problem can be solved by depositing another layer of superconductor (such as Al and Nb) on top of the thin Pd layer as the source of Cooper pairs.

As shown in Fig. 3.6(d), the zigzag patterns were observed. At the beginning, this patterns were explained by the stacking of different domins in the thickness diretion. Later the zigzag patterns has been identified by atomic-resolutionHAADF images and simulations based on this images (see the section of 4.2). We found that the zigzag patterns correspond to a PdTe-like phase.

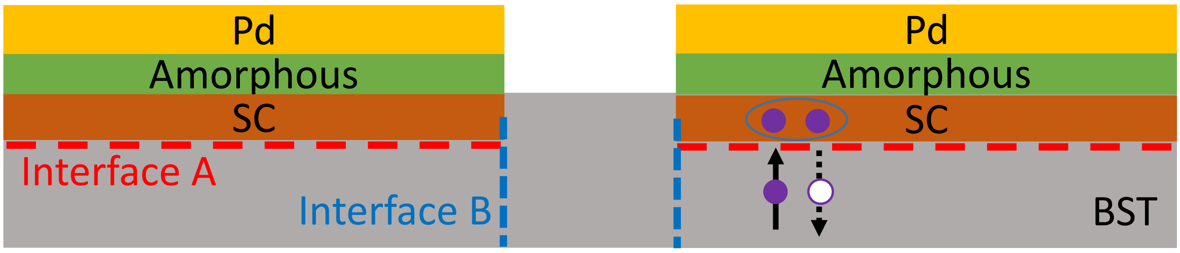

Figure 3.24: Cross-sectional schematic of the planar Josephson junction. (a) Resistance of the Josephson junctions as a function of time, measured at room temperature in a vacuum chamber with the pressure of $\sim 10^{-1}$ mbar. (b) and (c) SEM images of device A and device B.

In device B the junction transparency has been estimated to be 0.96. Usually the subgap features in the conductance spectra can be observed in JJs with a high transparency. These subgap features are related to the multiple Andreev reflections. However, there is lack of signatures for MAR in our devices. To figure the possible reasons, the schematic cross section of a planar Josephson junction was shown in Fig. 3.24. In fact, a planar JJ is not a SNS junction but a SS′NS′S junction, where S′ is the proximitized TI underneath the SC electrodes. There are two interfaces in the JJ, the interface A between SC and S′ and the interface B between S′ and BST in the gap.

Estimation of the junction transparency by excess current based on the OTBK theory [53] was used quite often in the planar junctions [30, 77, 80]. However, the interface has not been specified. It's more likely the excess current value is related to the transparency of the second interface. The signatures of MAR can be detected only when both of the two interfaces are highly tranparent [82, 83]. The data showed here is not enough to clearly anwser the question. We need more data from some new devices, such as the temperature dependence of the critical current of the JJs, which gives the junction transparency in a different way.

3.8 Conclusion on the planar junction device

We have invented a novel method to fabricate the hybrid S-TI-S Josephson junctions devices by simply depositing Pd on thin films of BST. The epitaxial self-formed $PdTe_2$ superconductor has been idetified by STEM and EDX analyses. This kind of devices have promising potentials for the realization of the Fu and Kane proposal where a topological superconducting state can be engineered, and the Majorana fermions are predicted to be created. Majorana fermions are of particular interest because they are building blocks for topological quantum computing [10, 84]. There are many researchers working on a variety of materials, but growth of a superconductor on the surface of a topological insulator with a good proximity effect has been a challenge still. Epitaxial growth of TI on the surface of a superconductor has been reported [85–88], but there is no JJ devices fabricated based on this technique. To the best of our knowledge, epitaxial growth of a superconductor on the TI surface has been reported only once by Xue $etal$. where the $PdTe_2$ was epitaxially grown on Bi_2Te_3, but the superconducting property of $PdTe_2$ was poorly characterized and lack of device fabrication.

The superconducting property of self-formed $PdTe_2$ has been characterized in the section of 3.2. A sharp superconducting transition was observed, suggesting that $PdTe_2$ is reasonably homogeneous. So, it is possible to fabricate a high quality S-TI-S JJ by using the self-formed $PdTe_2$ superconductor.

The Fraunhofer-like pattern in device A and especially a standard SQUID-type oscillations in device B comfirm that the junctions are not shorted and the supercurrent distribution in the JJ is also homogenous.

However there are some problems which have not been understood well. We have studied the Pd diffusion in the thickness direction by STEM and EDX, while we have no idea about the Pd diffusion along the lateral direction. We know that the self-formed $PdTe_2$ can be obatined when Pd is deposited either by magnetron sputtering or by thermal deposition. Whether the Pd diffusion process is the same for two deposition methods need to be checked by STEM and EDX measurements on two kinds of Pd/BST bilayer films.

Even though the transparency in device B is as high as 0.96, the subgap features result from the multiple Andreev reflection have not been observed, suggesting that the devices based on the self-formation of $PdTe_2$ need to be promoted further. In summary, we have developed a novel and flexible technique to get the hybrid S-TI-S Josephson junctions. The self-fromed superconducting phase has been identified by STEM and EDX and the transport properties of the JJ devices have been characterized. By means of such previous studies, we have prepared for further researches about Majorana physics, such as the missing of odd Shapiro steps due to the appearance of the Majorana modes.

4

Sandwich Josephson junction fabricated with $Pd/(Bi_{1-x}Sb_x)_2Te_3$ bilayer

In this chapter, I discuss the self-formed superconductor that is epitaxially grown on the $(Bi_{1-x}Sb_x)_2Te_3$ (BST) thin film. To characterize how the superconductor grows and to identify the SC phase, Pd/BST bilayer samples were specially designed for STEM and EDX studies. According to the STEM results, a BST nanowire sandwiched by SCs was created. This nanowire and SCs can constitute an SNS-type sandwich Josephson junction, which allows us to study the superconducting proximity effect and characterize the electronic transparency of the TI/SC interface. Magnetic field dependence of the critical current and $I - V$ characteristics were measured. At last, the missing of the first Shapiro step is discussed. It turns out that a 4π-periodic contribution to the current-phase relation (CPR) exists in our sandwich JJ devices. The 4π-periodicity may be caused by topological Majorana bound states.

The following chapter is based on a paper published as:
Mengmeng Bai, Xian-Kui Wei, Junya Feng, Martina Luysberg, Andrea Bliesener, Gertjan Lippertz, A. A. Taskin, Joachim Mayer, and Yoichi Ando; *Novel realization of superconducting topological-insulator nanowires*; arXiv preprint arXiv:2108.08559, (2021).

Dr. Xian-Kui Wei, Dr. Martina Luysberg and Prof. Dr. Joachim Mayer performed the STEM analyses on the devices that were prepared by Mengmeng Bai.

4.1 Device fabrication

4.1.1 Sandwich Josephson junction

The $(Bi_{1-x}Sb_x)_2Te_3$ (BST) films mentioned in this chapter were grown with a molecular beam epitaxy (MBE) technique on sapphire substrates from Knudsen cells. High-purity Bi, Sb, and Te were simultaneously evaporated. The Sb/(Bi+Sb) flux ratio of film 1 (used for device 1) and film 2 (used for device 2 and device 3) were 0.84 and 0.90, respectively. As there are no capping layers on the BST surface, nanofabrication of devices was performed immediately after the BST films were taken out from MBE chambers.

A standard electron-beam lithography technique was used to transfer small patterns on the BST films coated with PMMA A4 resist. In order to have a small undercut structure, the development was done with IPA/DI water (= 1:3) rather than the well-known Methyl isobutyl ketone (MIBK)/IPA. Then the samples were moved into an RIE system to remove the possible oxidie layer and resist residues. The surface of the BST films was cleaned by Ar-plasma etching at 10 W for 2 minutes.

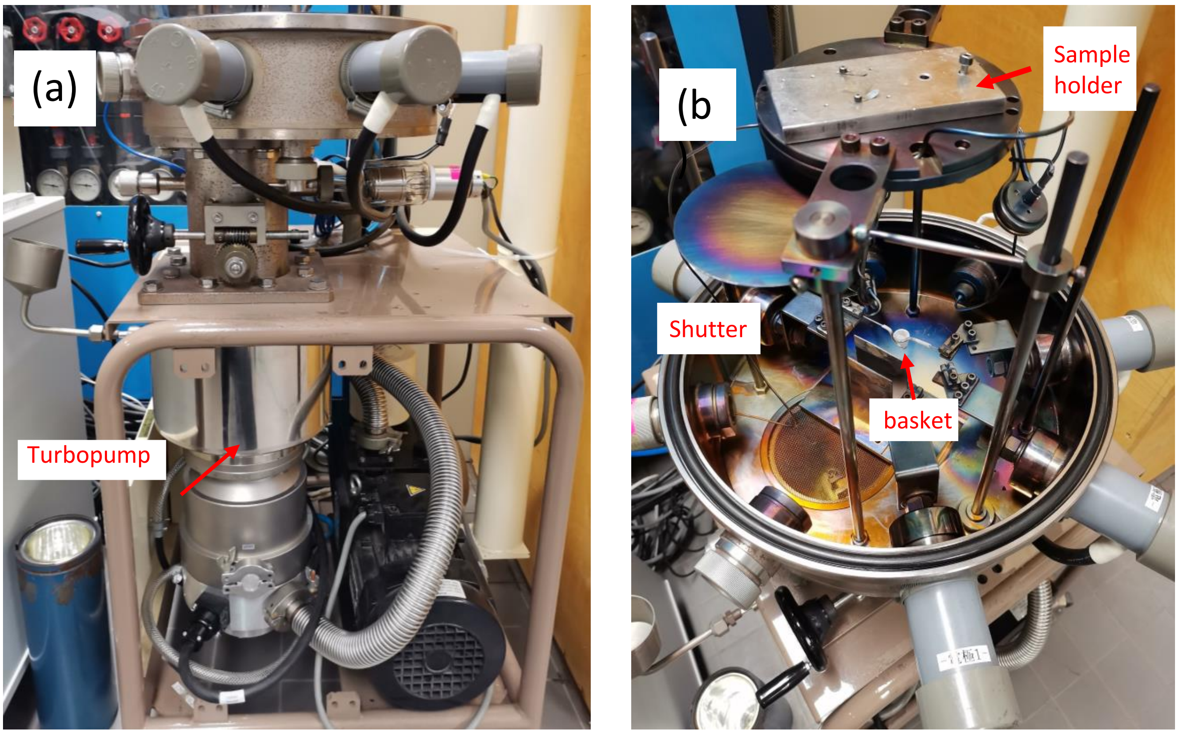

Figure 4.1: Pictures of the thermal evaporation system. (a) A turbopump and an oil pump was used to obtain a high vacuum. (b) Picture of the core components inside the chamber.

To fabricate a sandwich Josephson junction device, a thermal evaporation system is the only facility used for metalization. As shown in Fig. 4.1(a), a high vacuum is obtained by an oil pump and a turbopump. It is worth mentioning that a liquid nitrogen cold trap is equipped for the turbopump, which can make the limit pressure one order lower, because the pumping speed of the liquid nitrogen cold trap is much higher than the turbopump. Fig. 4.1(b) shows the alumina crucible mounted between the anode and the cathode. A large current of about 25 A was applied through the alumina crucible when the pressure is close to 1×10^{-7} mbar. The Pd atoms evaporated out from the crucible and move towards the substrate ballistically.

As shown in Fig. 4.2(a), after the lift-off process, the Pd electrodes were deposited on a continuous BST film, which means they are short connected by the BST film. To electrically separate the Pd electrodes, the BST films were partially dry-etched by Ar plasma at 50W for 3 minutes. The dark-blue areas are the etched part of the BST films as shown in Fig. 4.2(a). They corresponds to the dark-black region in Fig. 4.2(b), which was taken at a lower magnification. The length of Josephson junctions is an important parameter for classification. The short junction and long junction are defined by the comparison between junction length (L) and superconducting coherence length ϵ_N. When the mean free path l_e is smaller than L, the Josephson junction is diffusive. When $l_e > L$, the junction is ballistic. Besides, the critical current of Josephson junctions also depends on the junction length. So the gap L is systematically tuned from 100 to 150 nm, as shown in Fig. 4.1(a).

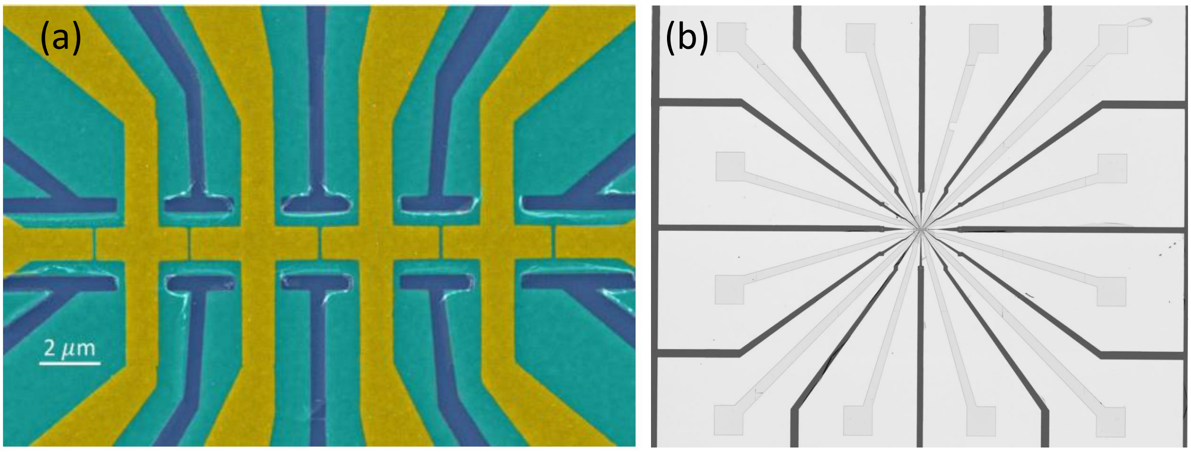

Figure 4.2: False-color SEM image and laser microscope image of the wafer including device 1 (2nd left junction). (a) False-color SEM image of the wafer. Pd electrodes, BST film, and sapphire substrate are coloured by dark-yellow, turquoise and dark-blue, respectively. The five junctions pictured here were fabricated with the Pd gap ranging from 100 to 150 nm (from left to right). (modified from [89]) (b) Laser microscope image of the wafer at a lower magnification. The Pd electrodes (gray) were isolated by the dry-etched BST films (black).

The Pd pads to define the JJs have a width of 1 μm. The turquoise area is the BST film (see Fig. 4.2(a)), the Pd electrodes in dark-yellow colour were deposited onto BST film. Fig. 4.2(b) shows a laser microscope picture at a lower magnification. We see the Pd electrodes (gray) were separated by the etched BST films (black). In the center of the sample, some resist residues were observed, even though the sample was bathed in N-Methyl-2-pyrrolidone (NMP) at 70°C for ~ 3 hours. Because the PMMA becomes very hard after a relatively long period of time of high-power dry etching. However, this insulating PMMA does not affect the measurement.

4.1.2 Samples prepared for STEM experiments.

As mentioned in the Chapter 3, the superconducting transition was also observed when Pd was deposited by thermal evaporation. To study whether the methods of Pd deposition can affect the Pd diffusion process, we prepared two samples for STEM analysis. A ~ 30-nm-thick BST film was epitaxially grown on sapphire (0001) substrate with the Sb/(Bi+Sb) flux ratio of 0.85. Ten nm of Pd was deposited by magnetron sputtering in sample 1, while 15 nm of Pd was deposited by thermal evaporation in sample 2.

The sapphire substrate is very hard to cut for preparing the lamella specimens, so the sapphire is replaced by InP (111)A substrates for the next batch of samples. A ~ 30-nm-thick BST film was epitaxially grown with the Sb/(Bi+Sb) flux ratio of 0.67. Two different types of samples are shown in Fig. 4.3. Six square Pd pads were thermally-deposited on BST film that aligned along $\langle 110 \rangle$ (sample 3) direction and $\langle 1\bar{1}0 \rangle$ (sample 4) direction, respectively. The gap between two adjacent Pd pads is ~ 200 nm.

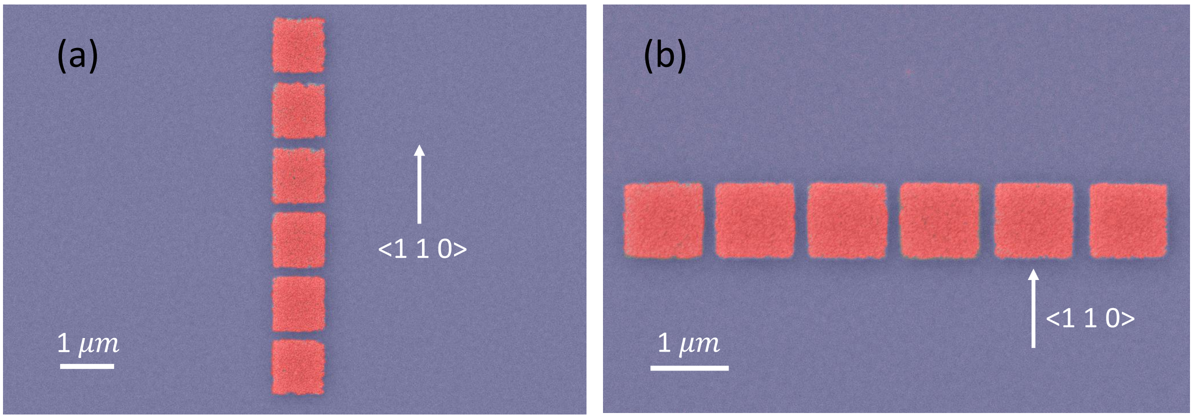

Figure 4.3: (a) and (b) Top view SEM images of Pd-pad arrays along $\langle 110 \rangle$ direction and $\langle 1\bar{1}0 \rangle$ direction, respectively.

The Pd/BST/InP multilayer lamella specimens were prepared by using the focused ion beam (FIB) system (FEI Helios Nanolab 400s). In order to protect the specimens from damage by the Ga ions that were used to cut the samples, ~ 160 nm of carbon and ~ 2 nm Pt were deposited on the surface of the samples. Afterward, the surface contamination was cleaned by plasma. An FEI Titan 80-200 ChemiSTEM microscope, which is equipped with a Super-X EDX spectrometer and STEM annular detectors, was used to collect HAADF images at an acceleration voltage of 200 kV. HAADF image simulation was done by the Dr. Probe software package [90], and the crystal structure was drawn by the VESTA software.

4.2 STEM results

STEM is one of the best techniques to characterize the morphology and to identify the unknown phases assisted by EDX spectroscopy. Here, at first, we compared the results from two samples with Pd layers deposited by magnetron sputtering and by thermal evaporation. We found that the BST film beneath the Pd will be completely transformed when Pd was thermally deposited. Next, to study how the new phases formed in the horizontal direction, we did the STEM measurement on the edges of Pd pads. Furthermore, in case that the self-formation of new phases is anisotropic in-plane, we prepared two Pd-pad arrays that are orthogonal to each other.

4.2.1 Comparison between the two methods of Pd deposition

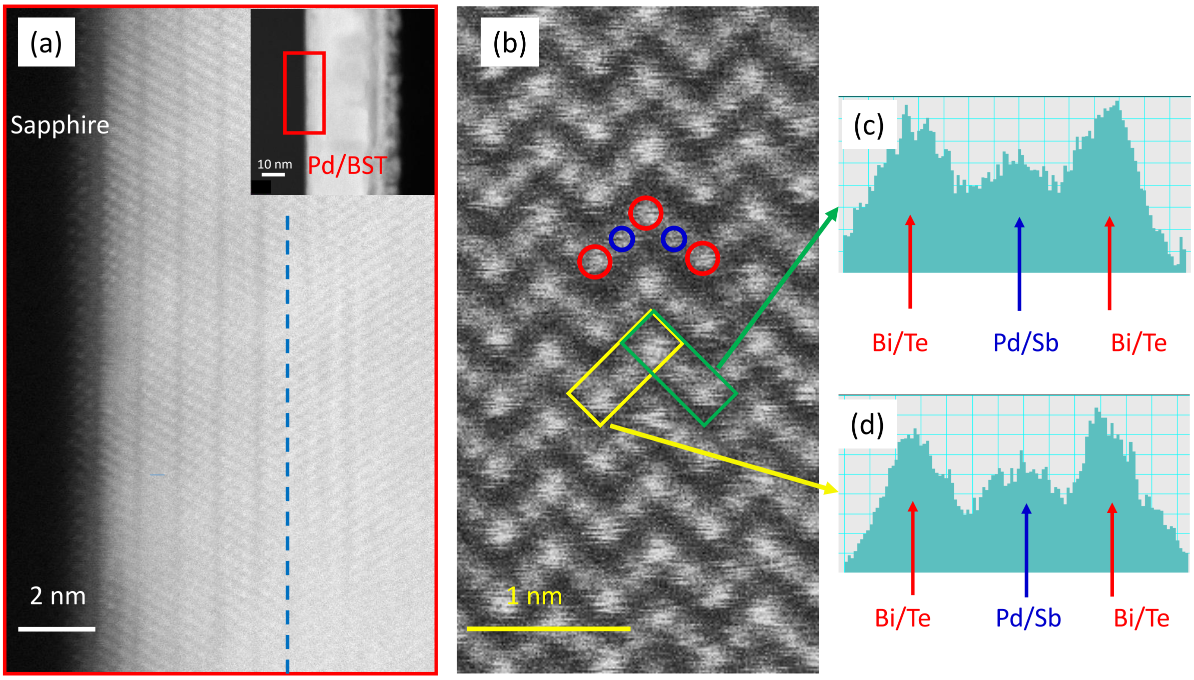

Figure 4.4: Inset in (a): HAADF-STEM image of the cross-section of sample 1. (a) Zoom-in of the interface between quintuple-layers of BST and zigzag-structured phase. (b) High-resolution HAADF image of the new phase, two kinds of atoms are labled by red and blue circles. ((c)-(d)) The intensity profiles correspond to the green rectangle and yellow rectangle in (b).

Fig. 4.4(a) shows a STEM image of sample 1, five quintuple-layers of BST was epitaxially grown on the sapphire substrate. Before Pd deposition, the thickness of BST film was ~ 30nm, suggesting that most of the BST films are converted to some new crystalline phases. In Chapter 3, we have reported that the new phase is the self-formed $PdTe_2$ superconductor by comparing the crystal structure and the lattice constants to known materials. Here the new phases are identified in a more advanced and reliable way. The epitaxial horizontal interface is indicated by the blue dashed line. A cross-section of the Pd/BST bilayer system shown in the inset of Fig.4.4(a) is the zoom-in of the red rectangle marked.

An atomic-resolution HAADF-STEM image of the new phase was shown in Fig. 4.4(b). The self-formed phase has a clear and homogeneous crystalline structure. Two kinds of atoms constitute a zigzag pattern, and the two atoms are labeled by red and blue colours individually. Atomic contrast of HAADF image is approximately proportional to Z^2 [91], where Z is the atomic number. Fig. 4.4(c) and (d) show the intensity profiles that were measured along with the green box and the yellow box in Fig. 4.4(b), respectively. The ratio of the intensity for the red atoms and the blue atoms both in Fig. 4.4(c) and (d) is ~ 1.05. The atomic numbers of Bi, Sb, Te and Pd are 83, 51, 52 and 46, respectively. The intensity ratio of Pd and Te Z^2_{Pd}/Z^2_{Te} is ~ 1.28, which reasonably consistent with the measured intensity profiles. The ratio of other atoms is far from the measured value (~ 1.05). So the new phase is identified to be a PdTe-like structure. It is prudent to mention that the zigzag pattern was also observed in the previous chapter, where we explain the appearance of the zigzag pattern is due to the stacking of different domains in the thickness direction. According to the analysis on the intensity, in fact, there is not only a $PdTe_2$ phase formed in the Pd/BST bilayer system but also a concomitant PdTe phase.

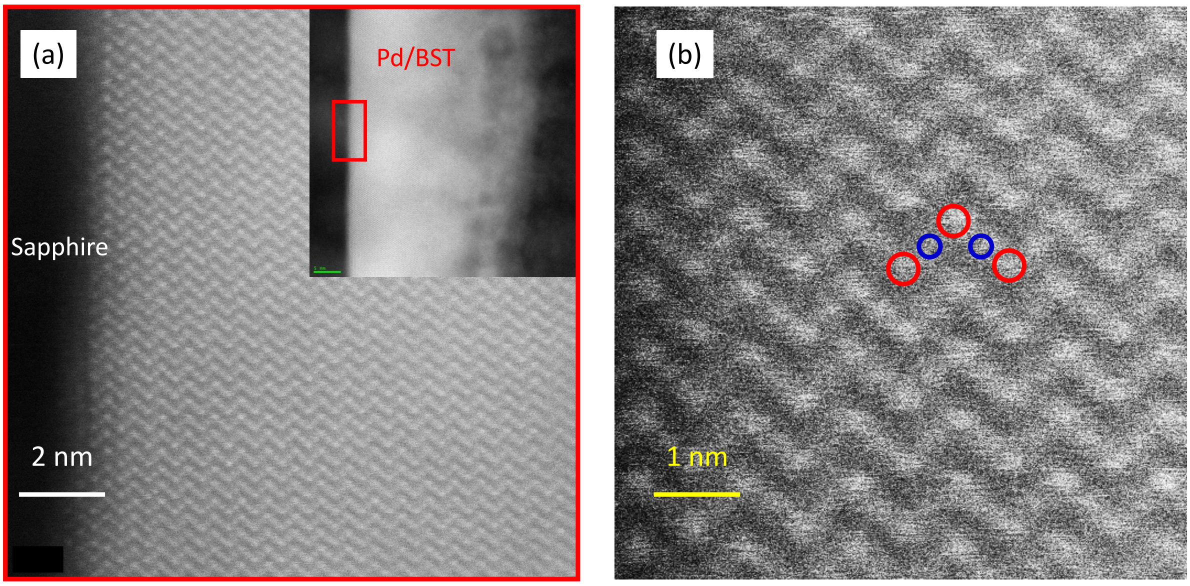

Figure 4.5: HAADF-STEM image of the cross-section of sample 2. (a) Zoom-in of the interface between sapphire and zigzag-structured phase. (b) High-resolution HAADF image of the zigzag pattern.

When Pd was deposited onto the BST film by thermal evaporation, the corresponding atomic-resolution HAADF-STEM image is shown in Fig. 4.5. Different from sample 1, there is no quintuple-layer of BST on the sapphire substrate. All the BST was completely transformed to other phases. Fig. 4.5(b) shows the zoom-in of an area in the new phase region. The zigzag patterns observed here are the same to the patterns in sample 1.

If we fabricate a Josephson junction whose Pd electrodes was made by thermal evaporation, the geometry of the junction will be different from what we reported in the Chapter 3. Since the

BST film beneath Pd is gone, the pristine TI is sandwiched between the newly formed phases. A sandwich Josephson junction is created. Besides, this finding provides the possibility to create a topological insulator nanowire. Until now all the STEM analyses are about the structure along the c direction (thickness direction). How does the Pd diffuse along the horizontal direction? To answer this question, sample 3 and sample 4 were prepared and the results will be presented below.

4.2.2 STEM analysis of Pd-array arranged along $\langle 110 \rangle$ direction

The STEM study for sample 3 mainly focuses on the region near the junction. Fig. 4.6(a) shows a high-angle annular-dark-field (HAADF) STEM image of the cross section of one junction. One can see that the distance between two Pd pads is ~ 231.7 nm, while the width of the pristine BST film is only ~ 40 nm. Not only the BST film beneath the Pd pads but also the film about ~ 90 nm outward from each edge of Pd pads are transformed in to another phase, which is labeled by Pd-BST. The thickness of Pd-BST is apparently thicker than the BST film. The swelling of Pd was absorbed by BST. It is prudent to note that the STEM measurement was done about 3 months after the Pd deposition and the Pd may diffuse along $\langle 110 \rangle$ direction continuously during this period. So the length of the pristine BST could be longer in devices that were fabricated soon after the Pd deposition.

The corresponding energy-dispersive X-ray (EDX) spectroscopy maps of Pd, Bi, Sb and Te are shown in Fig. 4.6((b)-(e)), respectively. Pd atoms are observed both in the BST film beneath Pd pads and the BST film in between two Pd pads. The inset of Fig. 4.6(e) shows the top-view SEM image of sample 3, the outward diffusion of Pd is along $\langle 110 \rangle$ direction. In Fig. 4.6(b) there seems also Pd atoms inside the pristine BST region. This is due to the background signal, judging by the fact that the signal intensity in the pristine BST and in the InP substrate are the same. So we claim that the disorder of the pristine BST does not increase by the Pd atoms. There is always a Pd-free region in between the Pd-BST parts(see Figs. 4.7((b)-(e))), forming a BST nanowire. The width of the nanowire changes from ~ 40 nm to 77 nm as the distance of the Pd-pads increase from ~ 191-239 nm.

According to the STEM analyses, it is clear that topological insulator nanowires sandwiched by superconductors is formed by simply depositing Pd on thin films of BST. The width and thickness of the nanowires are ~ 40 nm and ~ 30 nm, respectively, as shown in Fig. 4.6(a). The width of the nanowires can be further narrowed down by decreasing the distance between two Pd pads to guarantee a quantization of transverse-momentum states. Due to the V-shaped interface between BST and Pd-BST, the cross section of the TI nanowires is not a regular polygon but a concave hexagon. There are several advantages to this kind of TI nanowires. Such as the dimensions of the nanowires can be changed systematically and the chemical potential for both top and bottom surfaces can be adjusted by using the dual-gating technology, and nanofabrication is reproducible and straightforward.

Next, we identify the converted phase of Pd-BST and characterize the morphology of the system. Fig. 4.6(f) shows the atomic-resolution examination of the pristine BST region, high-quality epitaxial growth of BST film with quintuple-layers of TI were obtained on the InP

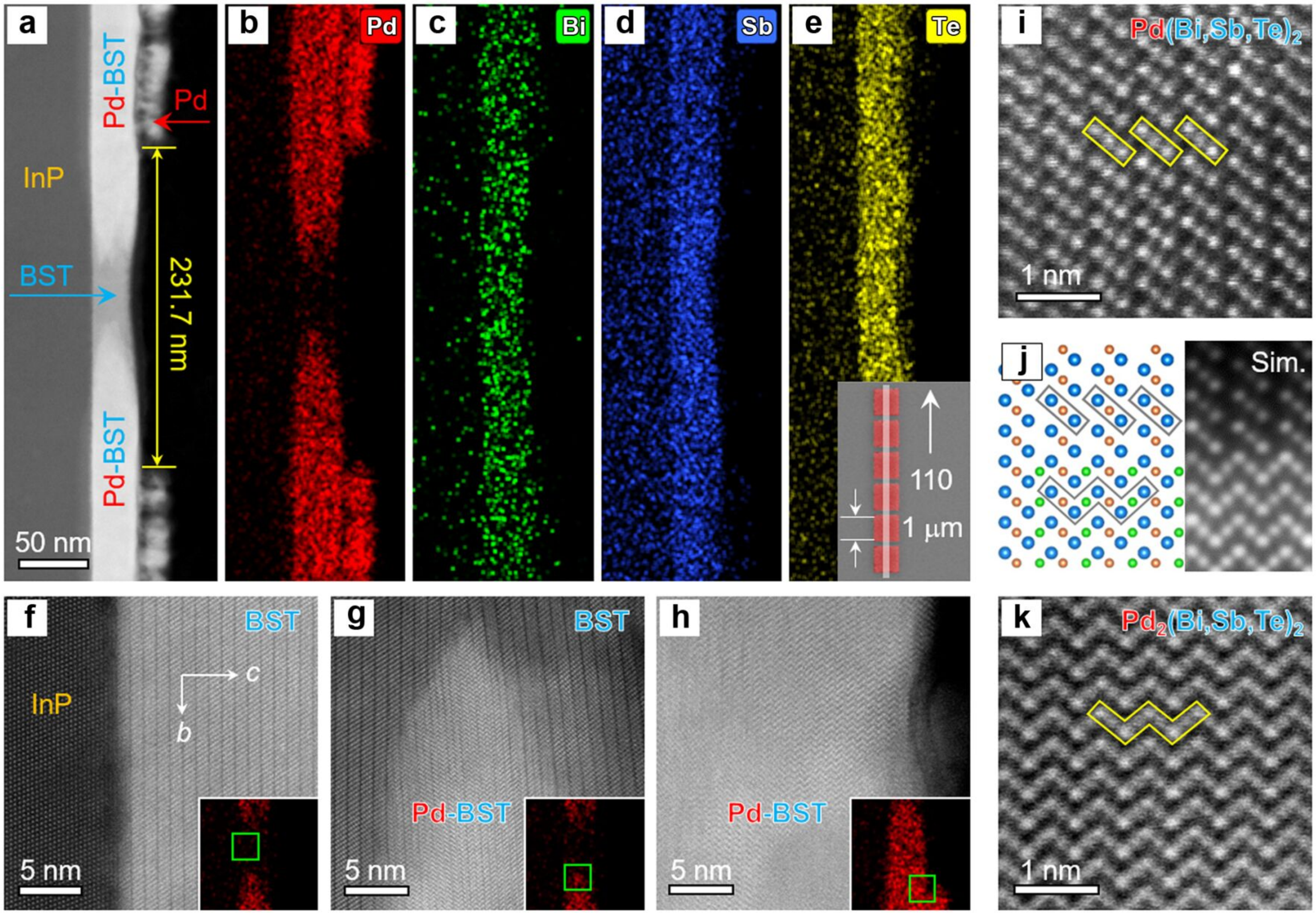

Figure 4.6: Cross-section of a sandwiched Josephson junction. (a) HAADF-STEM image of cross-section of Pd-BST/BST/Pd-BST hetrojunction. ((b)-(e)) corresponding EDX spectroscopy maps of Pd, Bi, Sb and Te, respectively. (e) Inst: A top-view SEM image of the Pd-pad array; the lamella specimen shown in (a) was cut out as as depicted by the light-gray stripe. ((f)-(h)) Atomic-resolution morphology of three regions in the specimen. The green squares in the insets illustrate locations of the characteristic regions. ((i)-(k)) High-resolution HAADF image of $PdTe_2$-like (i) and PdTe-like (k) structure of Pd-BST. (j) Schematic structural model and simulated HAADF image (thickness ~ 39 nm). The atomic sites coloured in blue, orange, and green may be occupied by Te/Bi/Sb, Pd/Sb, and Pd, respectively. Additional Pd atoms intercalated into the PdTe-like structure are coloured by green in (j). According to the atomic contrast in (i), one can see that Bi atoms are found only on the Te sites of the $PdTe_2$ structure. (modified from [89])

(111) surface. Atomic-resolution image near the interface bewtten Pd-BST and BST was shown in Fig. 4.6(g). The "epitaxial" interface has a V-shaped geometric structure. The triple-layer structure inside the V-shaped is $PdTe_2$ phase that was introduced in the previous chapter. While in the Pd-BST region closer to the Pd pads side, a zigzag pattern instead of TL structure is observed in Fig. 4.6(h).

Atomic-resolution HAADF images were to help to identify the TL phase and the zigzag phase (see Fig. 4.6((i)-(k))). It turns out that the TL- and zigzag-structured Pd-BST correspond to $PdTe_2$ like and PdTe-like phases [92], respectively, according to the image-simulation-based atomic structure analysis. A simulated HAADF image is shown in Fig. 4.6(j), the TL structure and zigzag pattern are reproduced well by the simulation. And the green balls are the additional Pd atoms intercalated into the PdTe-like structure. At different locations, the chemical formula may vary between $Pd(Bi, Sb, Te)_2$ and Pd(Bi, Sb, Te).

To make sure this phenomenon is not occasional, three more JJs with different Pd-pad gaps were characterized by STEM. Fig. 4.7(a) shows the HAADF-STEM image of a short junction. The EDX spectroscopy maps of Pd show that there is always a narrow BST nanowire sandwiched by Pd-BST (see Fig. 4.7). Pd propagates outward with different lengths in different JJs. To better understand the interface between BST and Pd-BST and the converted Pd-BST structure, atomic-resolution HAADF-STEM images were taken in the different locations on the interface. As shown in Fig. 4.7(g), the QLs of BST were appeared in the bottom left corner, while the $PdTe_2$-and PdTe- like structure occupied the other regions. Due to the Van-der-Waals gaps, the $PdTe_2$-like TL structure can be recognized by a dark contrast, while the PdTe-like structure has a continuous lattice image. So one can see that the $PdTe_2$-like structure is dominated near the "epitaxial" BST/Pd-BST interface. The structural models and simulated HAADF image are illustrated in the inset of Fig. 4.7(g). Fig. 4.7(h) show an atomic-resolution HAADF-STEM image of R2 close to the Pd pads. The PdTe-like structure without dark Van-der-Waals gaps tends to dominate near the top surface.

4.2.3 In-plane anisotropy of thermally deposited Pd samples

Before making JJ devices by using these self-formed PdTe or $PdTe_2$ superconductors, it is necessary to check whether the diffusion of Pd is isotropic. According to the hexagonal structure of BST, we prepared sample 4 that the Pd pads arranged along $\langle 1\bar{1}0\rangle$ direction, which is orthometric to the Pd pads in sample 3.

Fig. 4.8(a) shows a HAADF-STEM image of the cross-section of one junction in sample 4. A significant difference is that the diffused Pd connects the two Pd-BST parts that can be distinguished more clearly in the corresponding EDX spectroscopy map of Pd in Fig. 4.8(e), even though the length between two Pd pads is $\sim$ 210 nm. Figs. 4.8((b)-(d)) show the EDX spectroscopy of Pd in another three specimens for the $\langle 1\bar{1}0\rangle$ cases. The Pd-BST is not gapped at the center of the junction, and the QLs of BST only appeared in very small areas. It shows that the diffusion of Pd atoms in BST is anisotropic, the difussion constant in the $\langle 1\bar{1}0\rangle$ direction is faster than the $\langle 110\rangle$ direction.

Figs. 4.8(g) and (h) show atomic-resolution HAADF-STEM images of the regions that correspond to R3 and R4 in Fig. 4.8(f), respectively. QLs of BST is observed close to the bottom surface. $PdTe_2$- and PdTe-like structures observed here are similar to sample 3. The structural models and simulated HAADF image are illustrated in the insets of Figs. 4.8 (g) and (h).

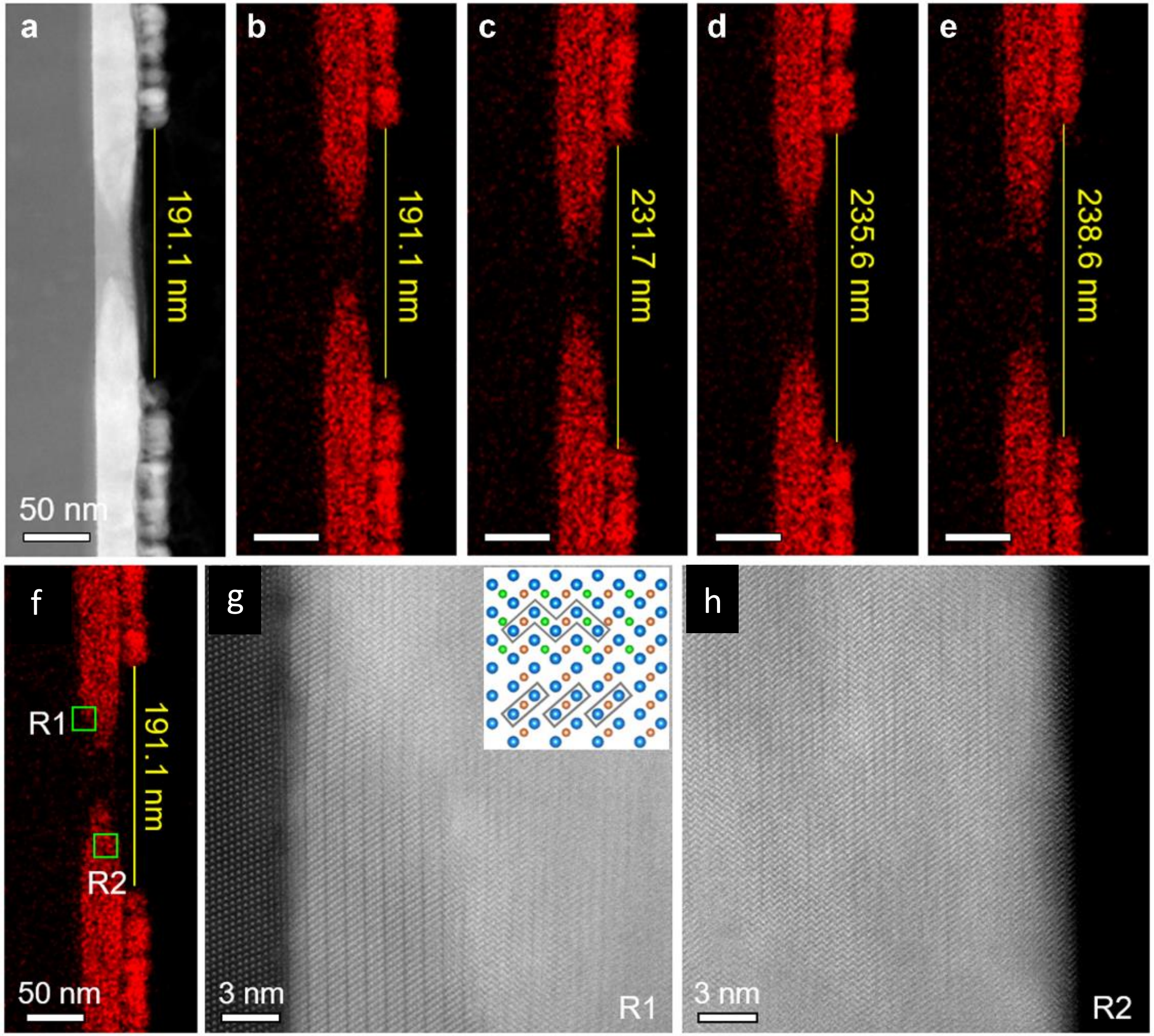

Figure 4.7: (a) HAADF-STEM image of junctions in sample 3. ((b)-(e)) EDX spectroscopy maps of Pd for four junctions with various distances of the thermally-deoposted Pd pads. (f) Reproduction of (b) with two marked region, R1 and R2. ((g)-(h)) Atomic-resolution HAADF-STEM images of the regions R1 and R2 indicated in (a), the atomic arrangements in BST indicates electron-beam incident direction of ⟨100⟩ and ⟨110⟩. Inset of (g) shows the structural models and simulated HAADF image. (modified from [89])

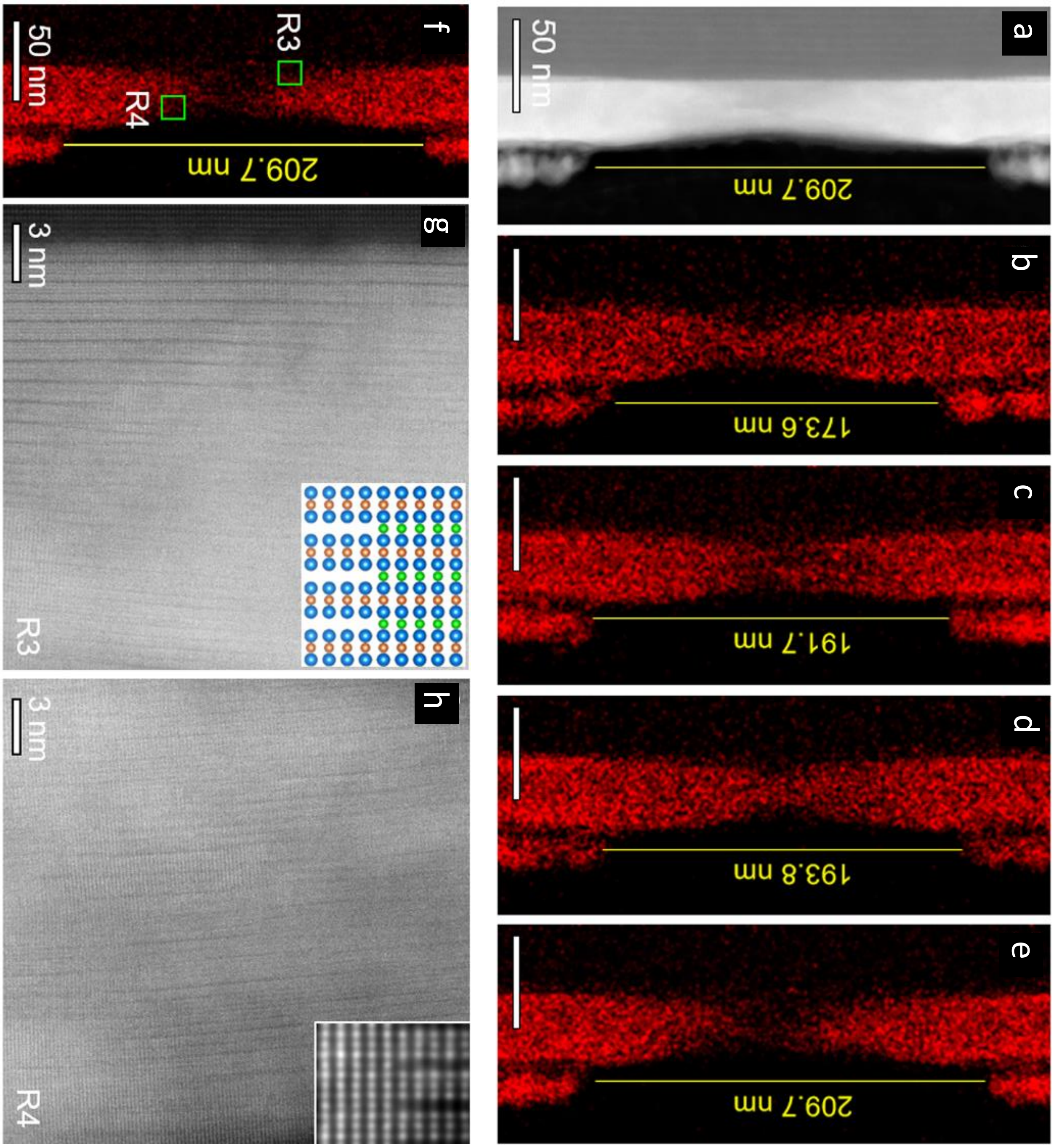

Figure 4.8: (a) HAADF-STEM image of a junction in sample 4. ((b)-(e)) EDX spectroscopy maps of Pd for four junctions with various distances of the sputtered-deposted Pd pads. (f) Reproduction of (e) with two marked region, R3 and R4. ((g)-(h)) Atomic-resolution HAADF-STEM images of the regions R1 and R2 indicated in (a), the atomic arrangements in BST indicates electron-beam incident direction of ⟨100⟩ and ⟨110⟩. Insets of (g) and (h) show the structural models and simulated HAADF image. (modified from [89])

4.3 Data and discussion of the Pd diffusion

The self-formed superconducting phases have been identified by STEM, however, the dynamic process of Pd diffusion is still unclear. The devices shown in Figs. 4.9(b) and (c) are designed to study the Pd diffusion process. The devices were fabricated the same to device 1 in section 4.1. As the Pd diffusion is anisotropic, we made the JJs either parallel to the $\langle 110 \rangle$ direction (Figs. 4.9(c)) or parallel to the $\langle 1\bar{1}0 \rangle$ direction(Figs. 4.9(b)). The width and the length of the junctions are 1 μm and ~200nm, respectively. Here we measured two Josephson junctions with a quasi-four-terminal configuration. The data I present here were taken on the fourth junction from each device. Device A and device B are indicated by a red rectangle and a blue rectangle in the SEM images (Figs. 4.9(b) and (c)).

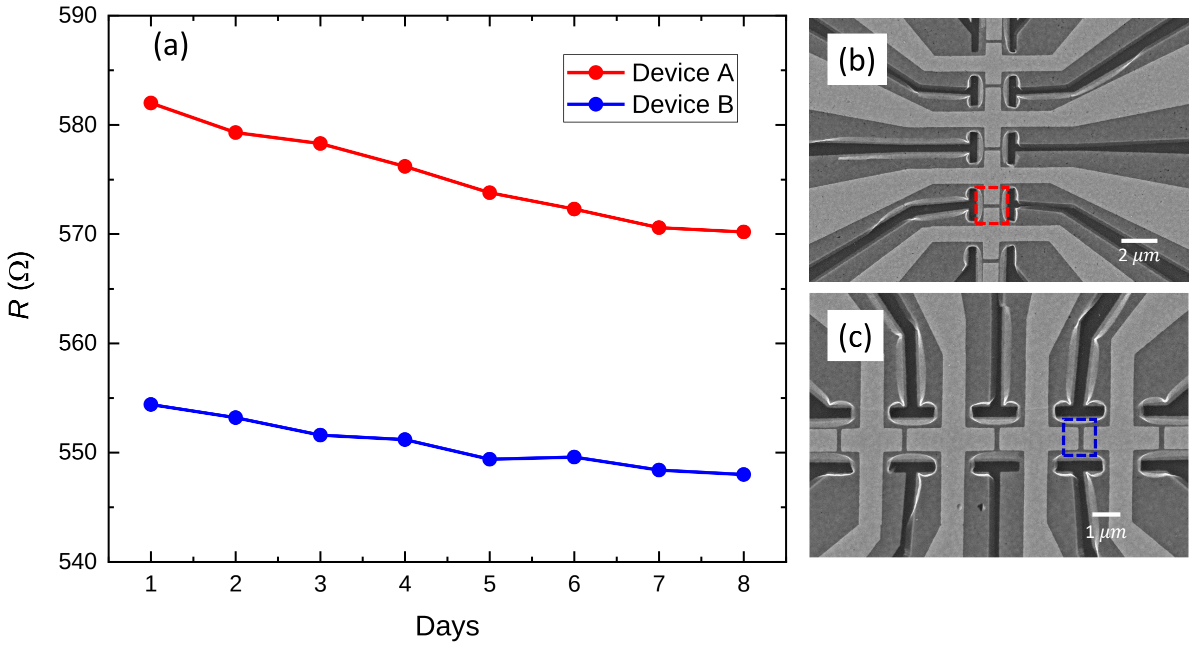

Figure 4.9: Time dependence of the junction resistance and the SEM images of the Josephson junctions. (a) Resistance of the Josephson junctions as a function of time, measured at room temperature in a vauum chamber at the pressure of ~ 10^{-1} mbar. (b) and (c) SEM images of device A and device B.

If the Pd-BST superconductors are formed, the resistance of the junctions will decrease beacause a semiconductor is transformed to a metal. So the junction resistance can be taken as a parameter reflecting the Pd diffusion process. The devices were kept in a vacuum chamber during the measurement to prevent the BST surface oxidation. Fig. 4.9(a) shows the time dependence of the resistance. The resistance decreases by about 2% for both devices after one week. Suggesting that the Pd is diffused at a relatively low speed. Therefore, the devices should be measured after fabrication as soon as possible.

Next, junction resistance were measured as a function of temperature in an annealing oven (MBE-Komponenten GmbH). The inset of Fig. 4.10 shows the annealing oven which has six wiring terminals and a heating plate. A diaphragm pump was applied to keep the sample in vacuum condition. The $R-T$ curves of device A and device B are shown in Fig. 4.10(a). When temperature is below ~ 420 K, the resistance is stable at a given temperature. The resistance decreases with increasing temperature, because the bulk-insulating BST film behaves like a semiconductor.

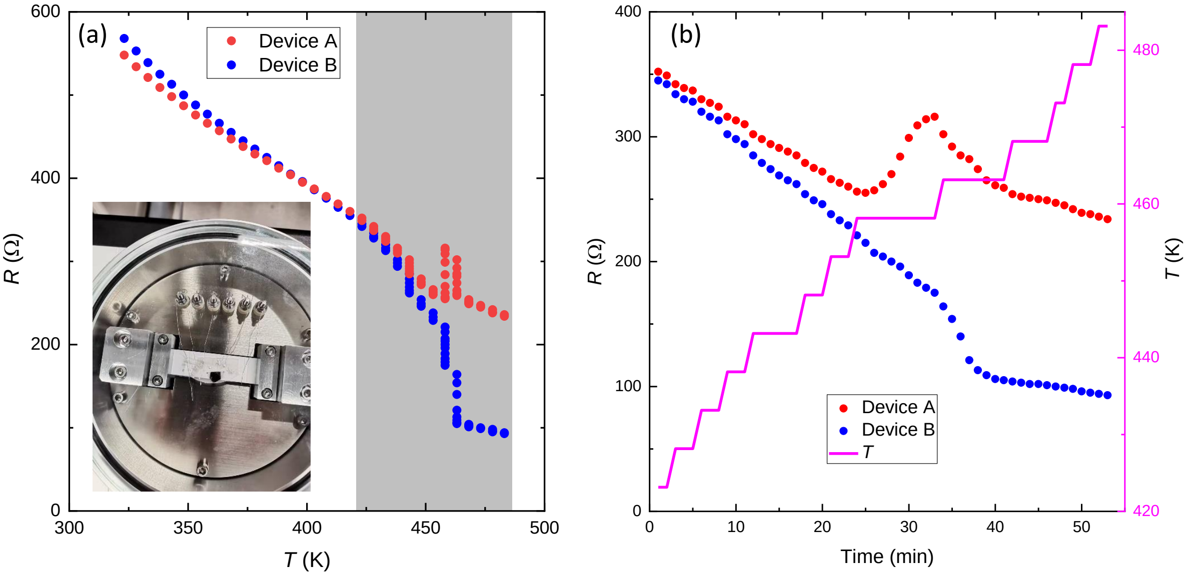

Figure 4.10: Temperature and time dependence of the junctions resistance. (a) Resistance as a function of temperature. Inset: Photo of the annealing oven. (b) Time dependence of resistance correponding to the data in the grey region in (a). Temperature as a function of time was plotted in pink colour.

However, when temperature is higher than ~425 K, the resistance decreases continuously even temperature is stable. This can be explained by the formation of Pd-BST alloys. The Pd diffusion begins when the threshold value of the temperature is achieved, the resistance of the junctions will reduce until all of the BST films inside the gap are gone. As shown in Fig. 4.10(a), the R-T curves in the grey region are not monodrome functions. We replot the data in the grey region in Fig. 4.10(a), the time dependence of the resistance is shown in Fig. 4.10(b). The temperature is scaled by the right Y-axis. For both device A and device B, we can see that the resistance drops much faster from ~ 450 K, indicating that the Pd diffusion is accelerated at high temperatures. However, the decreasing speed of the resistance suddenly retarded at a higher temperature about 461 K. The resistance of the junctions become singled again at a fixed temperature (Fig. 4.10(a)). The reason is that almost all of the BST film has been replaced by the Pd-BST.

There is another convincing evidence that the BST film inside the gaps has been converted to Pd-BST totally. We found that when the devices were cooled down to room temperature, the resistance of device A and device B did not recover but decreasd by ~ 2Ω. This behavior is consistent with the properties of metals of Pd-BST. It is prudent to mention that in Fig. 4.10(b), there is an abnormal peak of device A at 30 min. The origin of the peak is not clear. For future studies, we need to check whether the peak is reproducible and then try to figure out its origin. Besides, we get the knowledge that temperature is an additional tuning knob to control the width of the BST nanowire. We can narrow the nanowire in situ by mounting a heater on the sample holder. This can be a very useful technique. After judging by the experiments such as the Aharonov–Bohm effect[93, 94], we can narrow the nanowire by heating the device for a while if it is too wide.

We know that the Pd diffusion process is different when the Pd is deposited using different methods, such as magnetron sputtering and thermal evaporation. In this section, we proved that the Pd diffusion process could be accelerated by heating up the sample. The BST surface was irradiated by the melted high-temperature Pd materials in the boat during thermal evaporation. That's why the Pd diffused further in the case of thermal evaporation deposition. However, there is a lack of data related to the in-plane anisotropy of Pd diffusion.

4.4 Josephson junction properties

4.4.1 Transport characterization of $(Bi_{1-x}Sb_x)_2Te_3$ thin films

To characterize the transport properties of the BST films, Hall bars were made with a part of the film. As shown in the insets of Figs. 4.11(a) and (b), the Hall bars were scratched by hand with a sharp needle. The transport measurements were performed in a Quantum Design Physical Properties Measurement System (PPMS) with the base temperature of 2-3 K. Fig. 4.11(a) shows the temperature dependence of the sheet resistance of film 1. The sheet resistance decreases with decreasing temperature, suggesting that the film is bulk-conducting. Magnetic field dependence of the Hall resistance R_{yx} was shown in the lower inset of Fig. 4.11(a). The 2D carrier density of the film (n_{2D}) was estimated using the formula $n_{2D} = \frac{a}{eR_H}$, where a and R_H are the film thickness and the Hall coefficient, respectively. R_H is equal to the product of a and the slope of the $R_{yx}(B)$ data at $B = 0$. The n_{2D} of film 1 is $2.05 \times 10^{13} cm^{-2}$, the $R_S(T)$ behavior and the n_{2D} value of film 1 consistently show that this film is bulk-conducting.

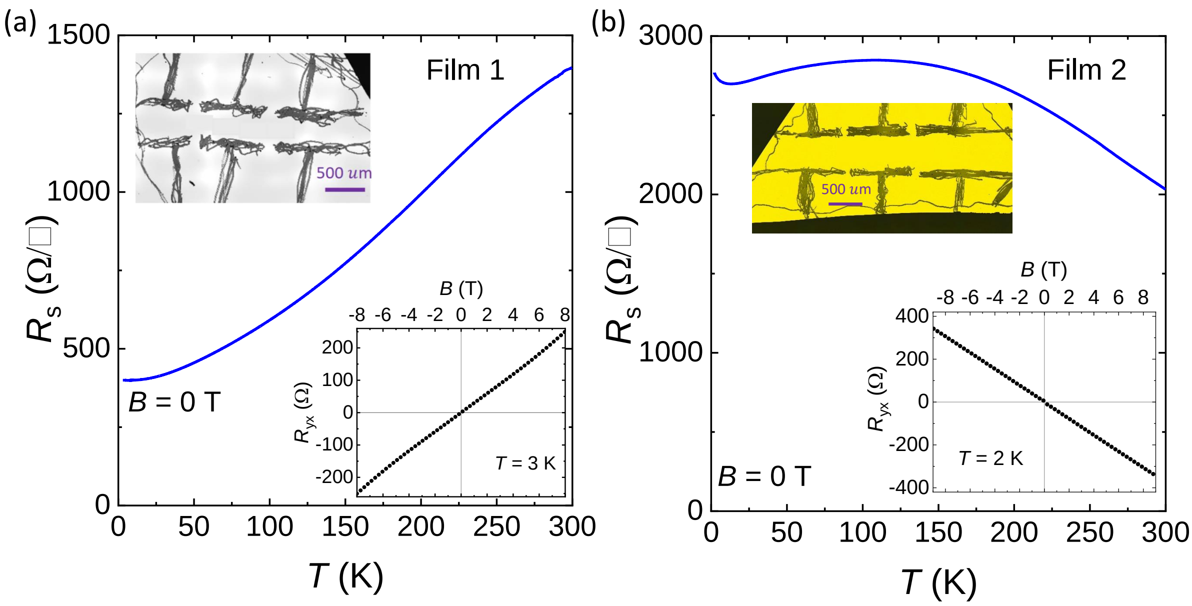

Figure 4.11: $R_S(T)$ data for film 1 used for device 1 (a) and film 2 used for devices 2 and 3 (b). Insets show their $R_{yx}(B)$ data at the base temperature and the laser microscope images of Hall-bar devices. (modified from [89])

However, in film 2, the $R_S(T)$ behavior shows that this film is bulk-insulating. A BST film is generally considered to be bulk-insulating when the carrier concentration is in the order of $\sim 10^{12} cm^{-2}$ [95]. However, the Hall data in the lower inset of Fig. 4.11(b) gives an n_{2D} of 1.63 $\times 10^{13} cm^{-2}$, which is too large for a bulk-insulating film. This inconsistency may come from the fact that the chemical potential of the BST is close to the Dirac point. The R_H value shows a zero-crossing if the chemical potential is swept across the Dirac point [96]. One can get an unphysically enormous n_{2D} value when the R_H value is near this zero-crossing region. Hence, based on the discussion above, we conclude that film 2 is bulk-insulating and has a chemical potential relatively close to the Dirac point.

4.4.2 Superconducting transition in the Josephson junction.

As discussed above, the Josephson junctions discussed in this chapter are all sandwich junctions. They have advantages as a potential platform for Majorana physics compared to the planar Josephson junctions. Observations of supercurrents in TI-based planar JJs have been reported in lots of previous works [30, 60, 61, 67, 76–80, 97–99]. A planar junction is actually a SS′NS′S junction. The TI beneath the electrodes, namely S′, was first proximitized by SC. Andreev bound states are formed between the S′/TI interfaces, not the interfaces between surface of TI and SC. Because S′ can have a soft gap, the effective superconducting gap relevant to Andreev bound states is usually smaller than the gap in the SC. In fact, to the best of our knowledge, an effective superconducting gap in TI-based planar junctions as large as the SC itself has been reported only once [30]. Besides, the additional in-gap states due to the S′ can also scatter the Majorana bound states.

However, in the sandwich JJs, the Andreev bound states are formed directly between the TI/SC interfaces. The superconducting proximity effect in our sandwich-type junctions is strong, and the effective superconducting gap is the same to the gap in SC estimated by $\Delta_{BCS} = 1.76\ k_B T_C$.

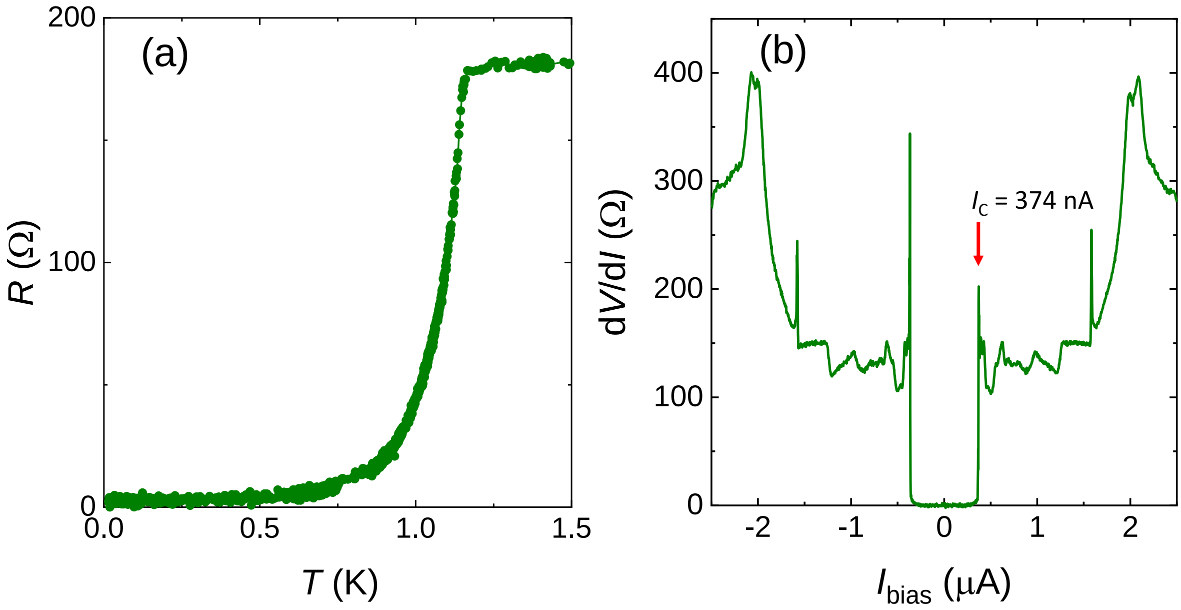

Figure 4.12: Temperature and time dependence of the junctions resistance. (a) Resistance as a function of temperature. (modified from [89]) (b) Differential resistance as a function of bias current.

Temperature dependence of the resistance in device 1 is shown in Fig. 4.12(a). One can see a sharp drop in R at T = 1.16 K, which corresponds to the superconducting transition of Pd-BST. The Δ_{BCS}(Pd-BST) is calculated to be 176 μeV. After a broad transition, zero resistance state is observed at $T \lessapprox 0.65$ K. Fig. 4.12(b) shows the differential resistance as a function of bias current (I_{bias}). A dissipationless supercurrent is observed when I_{bias} is below the critical current (I_C) of 374 nA. Except for the innermost two peaks that are due to the superconducting transition of JJ, there are a series of peaks between the critical current and $I_{bias} \sim 2$ μA. In Section 4.7, these peaks due to MAR will be discussed in detail.

4.4.3 Temperature dependence of the critical current.

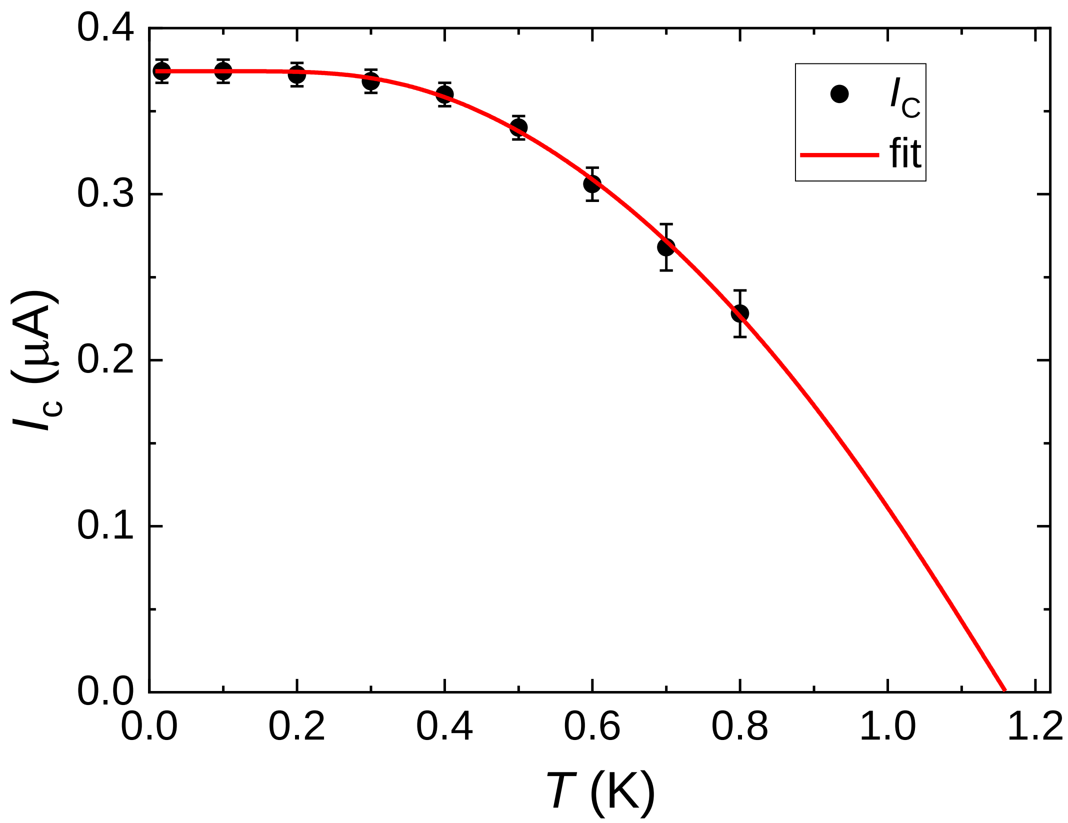

Figure 4.13: Temperature dependence of critical current of device 1. The black dots with error bars are experimentally measured I_C at different temperature. The red line is the best fit to the Galaktionov and Zaikin's model. (modified from [89])

The temperature dependence of the critical current of device 1 is shown in Fig. 4.13. The error bars in I_C are defined by the larger of (i) the amplitude of the ac excitation current (± 5 nA) or (ii) Half width at half maximum (HWFM) of the peak in dV/dI vs I_{bias} at the breakdown of superconductivity. I_C is clearly defined up to 0.8 K either by the temperature dependence of the dV/dI VS I_{Bias} or by the temperature dependence of the $I - V$ characteristics. The convex-shaped $I_C(T)$ curve shown in Fig. 4.13 is a signature for JJ in the short-junction limit [100, 101].

The $I_C(T)$ data are fitted by using the model proposed by Galaktionov and Zaikin [102]. This model was suitable for short ballistic JJs with arbitrary transparency. Then the supercurrent in the JJs is given by:

$$I_{JJ} = \frac{e\Delta}{2}\frac{\mathcal{T}\sin(\chi)}{\mathcal{D}}\tanh\frac{\mathcal{D}\Delta}{2T} \tag{4.1}$$

where Δ is the superconducting gap, $\mathcal{T}$ is the junction transparency, and χ is the phase difference between the two superconducting electrodes in the JJs. $\mathcal{D}$ is defined by

$$\mathcal{D} = \sqrt{1 - \mathcal{T}\sin^2(\chi/2)} \tag{4.2}$$

Here χ is arbitrary in current-biased JJ. The maximum value of I_{JJ} with respect to χ gives the critical current I_C = max[$I_{JJ}(\chi)$]. The red curve in Fig. 4.13 shows a good fitting for the $I_C(T)$ data. The best fit was obtained with the fitting parameters $\mathcal{T}_{crit} \simeq 0.7$ and Δ =174.4 μeV corresponding to a transition temperature of 1.15 K that agrees with the T_C of Pd-BST (see Fig. 4.12(a)).

Now let us check whether the applicable conditions for Galaktionov and Zaikin's model are satisfied by device 1. The distance between the two Pd electrodes in JJ of device 1 is ~ 100nm, and the Pd has diffused about 30 nm from both sides. Therefore, junction length L_J is shorter than 40 nm. The mean free path l_e in our BST film is about 10 nm. l_e is smaller than L_J but not too much. The JJ is close to the ballistic limit. The coherence length ξ can be estimated by the formula $\xi = \frac{\hbar v_F}{\pi\Delta_{SC}}$, where the Fermi velocity v_F is 3.68×10^5 m/s [103] and the superconducting gap Δ_{SC} = 184 μeV is introduced in Section 4.7. With these parameters we obtain $\xi \approx 390$ nm, which is much longer than L_J, suggesting that the junction is in the short-junction limit. So the conclusion is that the Galaktionov and Zaikin's model is suitable for our JJ which is in the short-junction limit and close to the ballistic limit.

4.5 Fraunhofer pattern

To study the properties of the spatial distribution of supercurrent in JJs and the current phase relation for JJs, we have measured the critical current response to an out-of-plane magnetic field. Fig. 4.14 shows a 2D map of the critical current as a function of the magnetic field for device 1. The critical current decays rapidly as the magnetic field increases in the low fields, and I_C drops to zero at $B \approx 3.8$ mT. We can estimate the effective junction area $S_{eff} = \Phi_0/3.8mT \approx 0.55\mu m^2$. This area should correspond to $W(L_J + 2\lambda)$, where W, L_J and λ are the junction width, junction length and London penetration depth, respectively. W and L_J are known, and $\lambda \approx 250nm$ is obtained.

However, when we increase the magnetic field further, the I_C does not drop to zero anymore. The $I_C(B)$ pattern is distorted from $B \approx 8$ mT, where I_C changed not smoothly but suddenly. Such anomaly can be caused by flux jumps, since the SC electrodes of our devices is as wide as 1 μm. To trap a magnetic flux quantum at B = 8 mT, the corresponding area is $\frac{\Phi_0}{B} = 0.26\ \mu m^2$. Considering the area is a circle, we get the radius of a magnetic flux quantum is ~ 300 nm. This estimation suggests that flux jumps can happen in our 1 μm wide Pd/BST electrodes, and in this case the Fraunhofer pattern will be destroyed.

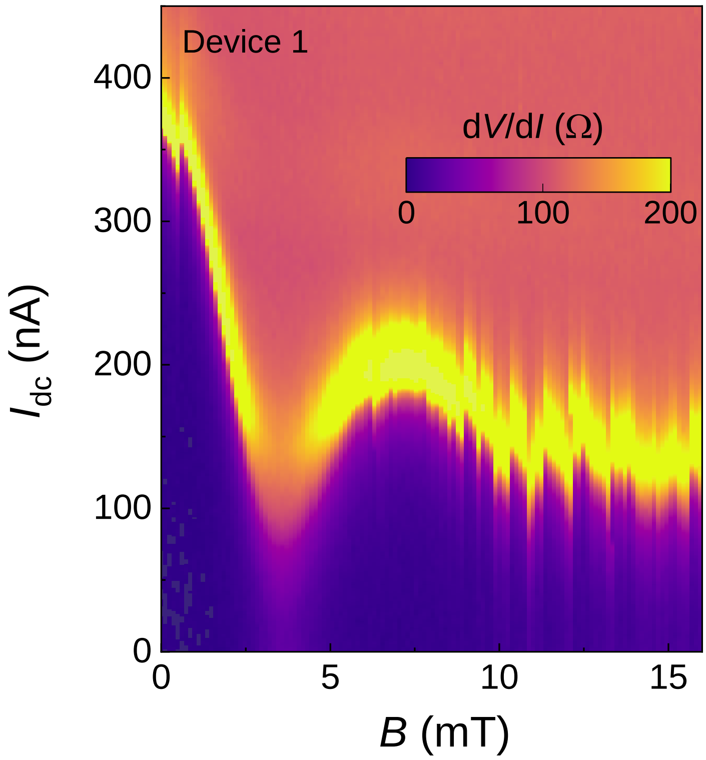

Figure 4.14: Fraunhofer-like pattern of device 1. 2D map of differential resistance as a function of dc bias current and magnetic field, measured at 8 mK. The discontinuous behaviour visible from ~ 8 mT is due to flux jumps. (modified from [89])

We also applied an out-of-plane magnetic field on device 2 and device 3. As shown in

Figs. 4.15(a) and (b), cleaner Fraunhofer-like patterns are observed in device 2 and device 3. The patterns are not distorted much by flux jumps, although the nanofabrication on all three devices is the same. There are two reasons why the flux-jump problem is particularly severe in device 1. First, the periodic in $I_C(B)$ for device 2 and device 3 is smaller. The flux jumps took place from ~ 7-8 mT in device 1 and device 2. Before 7.5 mT, there are about three lobes in device 2, while the second lobe does not complete in device 1 at ~ 10 mT. Second, according to our experience, the Fraunhofer patterns are sensitive to the measurement environment. For example, the quality of our data is bad when there are constructions and disturbances near our lab. The measurement environment for device 1 may be worse.

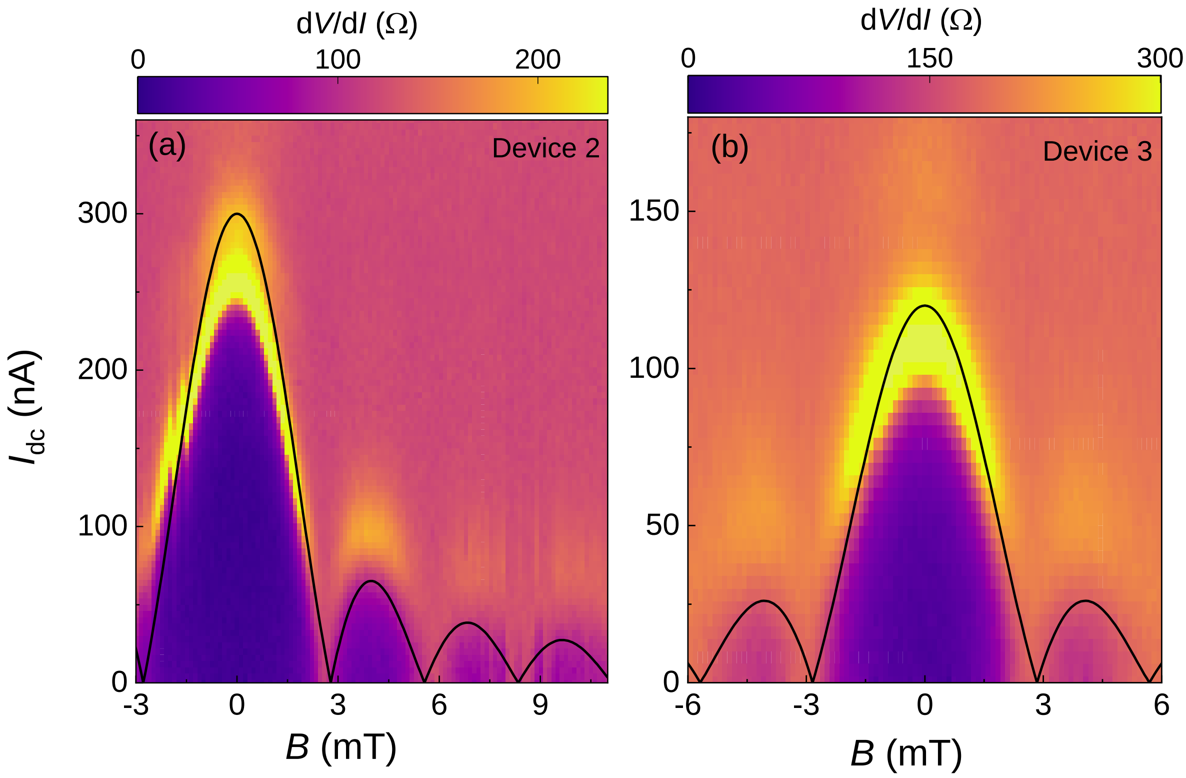

Figure 4.15: Fraunhofer patterns of device 2 and device 3. (a) and (b) 2D plots of differential resistance as a function of dc bias current and magnetic field. Standard Fraunhofer patterns are illustrated by the black lines. (modified from [89])

Black lines in Fig. 4.15 show the fits of critical current to the Eq. 3.10, this equation is used for JJs with a homogeneous supercurrent distribution. The good fittings suggest that our JJs are well defined in device 2 and device 3. From the magnetic field value of the first node, which is 3 mT in both devices, we obtain $S_{eff} \approx 0.7\mu m^2$ and $\lambda \approx 330nm$. The difference of the λ in two films is probably because the self-formed SC is not precisely the same in different batches of samples.

4.6 dc $I-V$ characteristics

To study the interface transparency and multiple Andreev reflection (MAR), the JJs were characterized by dc $I-V$ characteristics measurements in a pseudo-four-probe configuration. Fig. 4.16(a) shows a typical $I-V$ characteristic of device 1. When the dc bias current is smaller than the critical current (I_C) of 0.374 μA, the junction is in the superconducting state, and there is no voltage drop. The I_C is indicated by a blue arrow. The junction changes to a resistive state when the bias current is above I_C.

However, at low bias, the nonlinear $I-V$ curve doesn't follow the Ohm's law. That's due to the MAR processes when the bias voltage is lower than $2\Delta_{SC}$. The linearity of the $I-V$ curve gradually recovers when MAR is gone. An excess current (I_e) = 0.815 μA can be estimated by fitting the $I-V$ curve in the linear region. I_e is the y-intercept of the fitting curve. Also, the inverse of the slope for the fitting curve gives the normal-state resistance R_N = 266 Ω. Using Ic = 0.374 μA at 20 mK, we obtain the eI_CR_N product of 99.5 μeV, which gives an eI_CR_N/Δ_{SC} ratio of 0.54. This is among the largest ratio reported for a TI-based JJ.

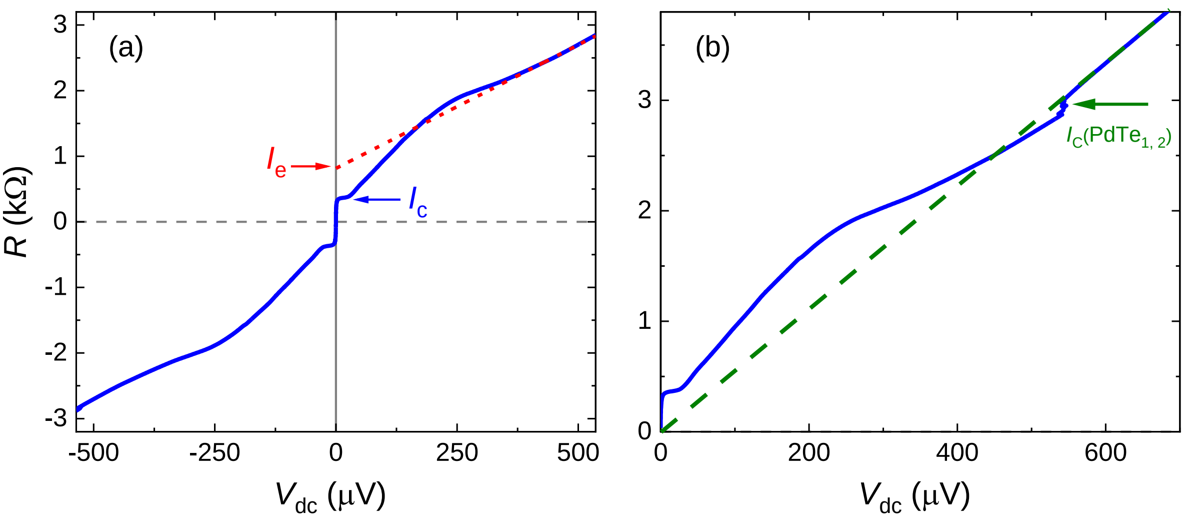

Figure 4.16: (a), (b)I-V characteristics of device 1. (a) The excess current I_e is estimated from the intercept of a linear fit to the high-bias region (red dashed line). (modified from [89])

Furthermore, as we have introduced in the planar JJ, the interface transparency $\mathcal{T}_{OTBK}$ can be estimated when we have I_e, R_N, and Δ_{SC}. The ratio eI_eR_N/Δ_{SC} = 1.18 gives the $\mathcal{T}_{OTBK} \approx$ 0.8. This $\mathcal{T}_{OTBK}$ is in reasonable agreement with the transparency $\mathcal{T}_{cirt} \approx 0.7$ that obtained from Ic(T) mentioned above.

To study the critical current of our self-formed SC phases. The dc bias current is swept to a larger value, as shown in Fig. 4.16(b), a linear fitting of the $I-V$ curve is performed in such a region. There is no excess current because of the fitting curve across the coordinate origin. Suggesting that the superconductivity of $PdTe_{(1,2)}$ is killed. The jump indicated by an olive arrow corresponds to the critical current of the SC electrodes $I_C(PdTe_{(1,2)})$, which is ~ 3 μA.

4.7 Multiple Andreev reflection

In the previous chapter, we introduced Andreev reflection at the N/S interface. Now let us consider a SNS junction applied by a dc bias voltage (V_{bias}) (see Fig. 4.17). A quasiparticle from the left SC can tunnel into the normal metal as an electron (hole), and the electron (hole) is retro-reflected as a hole (electron). Then the electron (hole) moves to the right NS interface with accumulating energy of eV_{bias}. Andreev reflections occur alternately between two interfaces n times until $neV_{bias} > 2\Delta$, and the particle leaves to the right SC. This process is the well-known multiple Andreev reflection (MAR) [104–106].

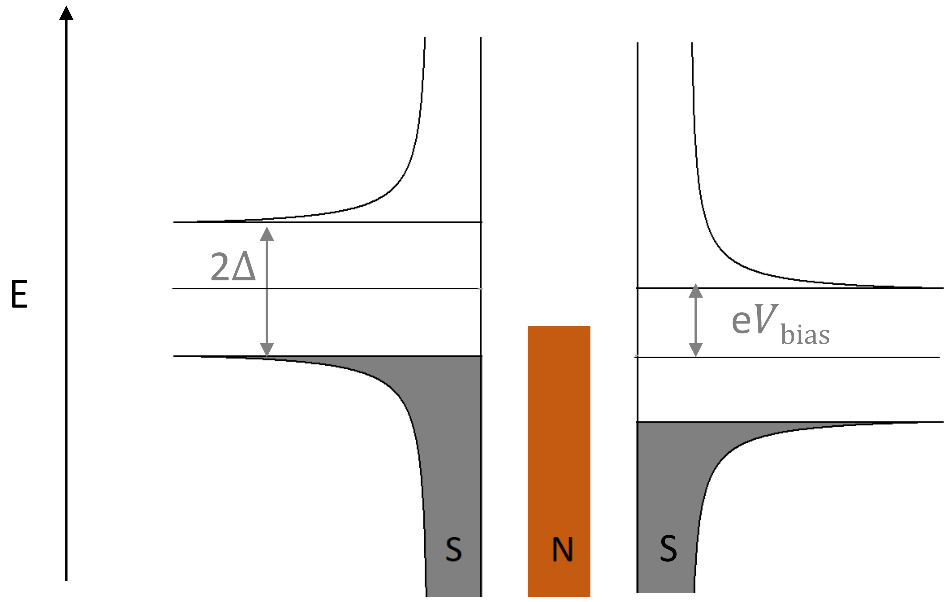

Figure 4.17: The density of states in the superconductor is that of quasiparticles and the density of states in the normal region is for electrons. A bias eV_{bias} is applied across the junction.

When $V_{bias} > 2\Delta/e$, an electron (hole) from left SC can be transferred to the right SC because the acquired kinetic energy is higher than the superconducting gap. As shown in Fig. 4.18(a), when $\Delta < eV_{bias} < 2\Delta/e$, an electron (hole) can not be transferred from left to right directly. Instead, an electron (hole) will Andreev reflect once . When V_{bias} is further decreased to $\frac{2\Delta}{3} < eV_{bias} < \Delta/e$, a particle can only get out after two times Andreev reflections (see Fig. 4.18(b)). So a nth order MAR involves n-1 times Andreev reflections. The MAR order is given by

$$n = \left[\frac{2\Delta}{eV_{bias}}\right] \tag{4.3}$$

According to the OTBK theory, resonance conductance peaks will occur at voltages $V_{bias} = \frac{2\Delta}{ne}$

[53, 107]. In principle, n can be arbitrarily large provided that V_{bias} is small enough. However, Andreev reflection is limited by the transparency (τ) where nth order MAR scales with τ^n. So the high order MAR can only be observed in JJs with high transparency.

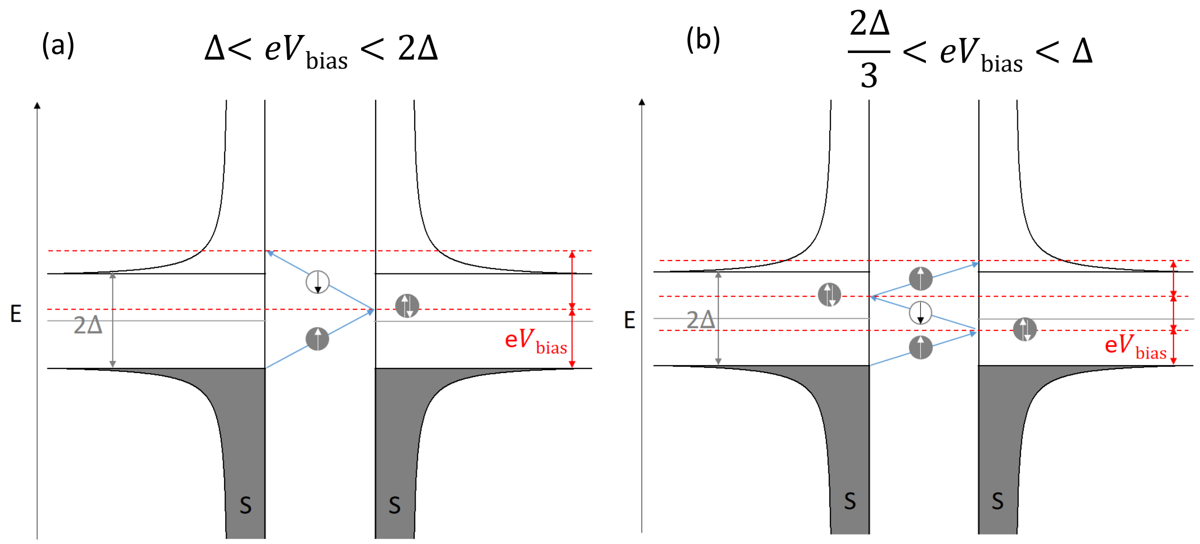

Figure 4.18: (a) and (b) panels show a 2nd and 3rd order multiple Andreev reflection process respectively.

Such subharmonic peaks are observed in device 1. Differential conductance as a function of dc bias voltage is shown in Fig. 4.19. The resonance peaks are labeled and indicated by black arrows. The n=1-5, and 9 order MAR are observed, and the amplitude of the ninth peak is the largest. The absence of higher-order peaks is expected of a JJ whose τ is smaller than 1 (which is $\tau \sim 0.8$ in device 1). Theoretically, the amplitude is expected to decrease with increasing n, because τ^n decay rapidly with n. Meanwhile, the amplitude of the first peak is the smallest. The reason for the abnormal amplitude is not clear. And the origin of the absence of peaks for n = 6-8 is unknown. Nevertheless, similar behaviors have been reported on different materials: $BiSbTeSe_2$ nanoflakes [30], $BiSbTeSe_2$ nanoribbons [67] and Ge/Si nanowires [108].

According to Eq. 4.3, the linear relation between $\frac{1}{n}$ and V_n is apparent. As shown in the inset of Fig. 4.19, the data points are located on a line, which agrees with Eq. 4.3 well. The induced superconducting gap $\Delta_{SC} = 184\mu eV$ is estimated from the slope of the linear fitting line.

4.7.1 Temperature dependence of the MAR

To clarify the nature of the induced superconducting gap, the temperature dependence of the differential conductance as a function of V_{dc} is shown in Fig. 4.20(a). The bias value of the subharmonic peaks decreases with increasing T. The temperature dependence for T < 0.5 K is very weak, and the MAR signatures are still distinguishable at T up to 1.0 K, which is close to

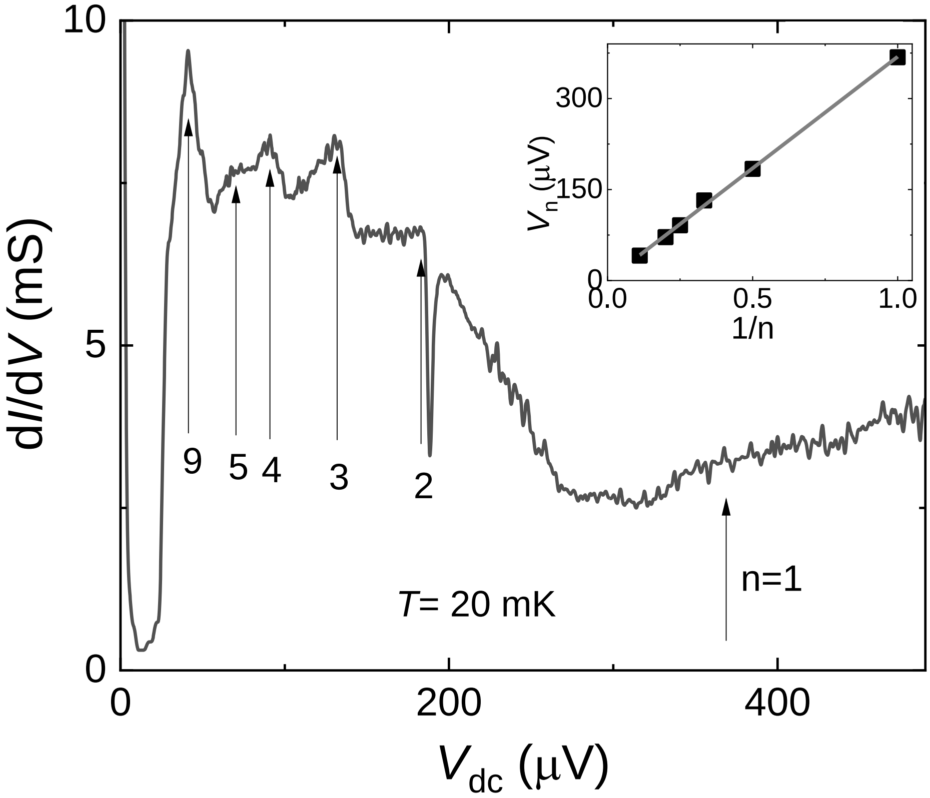

Figure 4.19: Plot of differential conductance dI/dV vs V_{dc}. Inset: Peak position V_n vs inverse peak index $1/n$. (modified from [89])

the $T_C(PdTe_{(1,2)})$ = 1.16 K. Suggesting that the superconducting proximity effect in device 1 is strong. Above $T_C(PdTe_{(1,2)})$, at 1.2 K, all the MAR signatures are gone. The peaks at around 400 μeV, T = 0.8, 0.9 and 1.0K and the peaks at around 200 μeV, T = 1.1 K correspond to the superconducting transition of the electrodes.

The linear fitting of V_n vs $1/n$ gives the superconducting gap at different temperatures. Fig. 4.20(b) shows the temperature dependence of the gap Δ. The experimental data $\Delta(T)$ can be fitted using the BCS expression [109, 110]:

$$\frac{\Delta(T)}{\Delta(0)} = \tanh\left\{\frac{T_c}{T}\frac{\Delta(T)}{\Delta(0)}\right\} \tag{4.4}$$

The good correspondence between Eq. 4.4 and our data suggesting that Pd-BST is a conventional BCS superconductor.

4.8 Reproducible results on device 2 and device 3

The observation of MAR is reproduced in two more devices (device 2 and device 3). Data in figs. 4.21(a)-(b) and Figs. 4.21(c)-(d) are taken from device 2 and device 3, respectively.

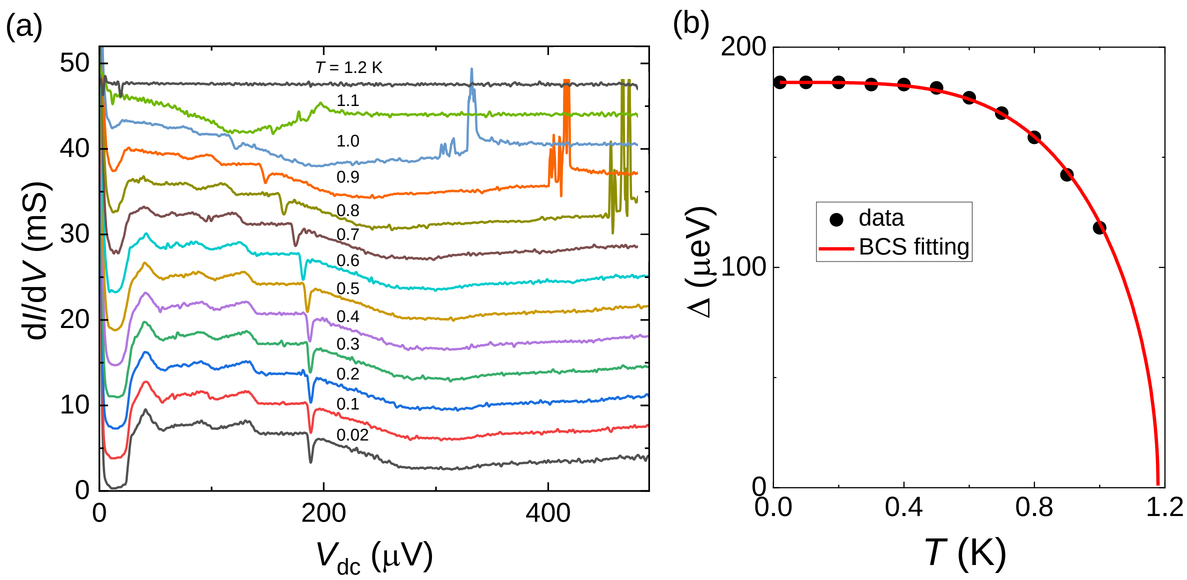

Figure 4.20: (a) dI/dV as a function of the dc bias voltage V_{dc} at various T; the curves are successively offset by 3.5 mS, except for the 20-mK data. (b) T dependence of the superconducting gap of device 1 with a theoretical fit (red solid line). (modified from [89])

In device 2, the resistance reaches zero when $T < \sim 0.6$K(see Fig. 4.21(a)). The inset of Fig. 4.21(a) shows the dc $I-V$ characteristic, where I_C = 346 nA, I_e= 815 nA and R_N=365 Ω. The differential conductance as a function of dc bias voltage is shown in Fig. 4.21(b). MAR resonance conductance peaks for $n = 1, 2, 3, 4, 6, 8$, and 13 are observed. The plot of the voltage at the peak (V_n) vs $\frac{1}{n}$ lies on a straight line (see inset of Fig. 4.21(b)). As described above, a superconducting gap of 145μeV is estimated. The ratio eI_CR_N/Δ of 1.03 gives a transparency of 0.75 according to the OTBK theory.

In device 3, the transition temperature of Pd-BST is the same to $T_C(PdTe_{1,2})$ in device 2 (see Fig. 4.21(c)). While the zero-resistance state is achieved only when T<0.1 K. And the I_C = 88 nA is much smaller than I_C of device 2. The subharmonic features of MAR in device 3 are weak shoulders rather than peaks, and the features are indicated by black arrows. The small $T_C(JJ)$, I_C, and weak signatures of MAR are due to the longer junction length in device 3.

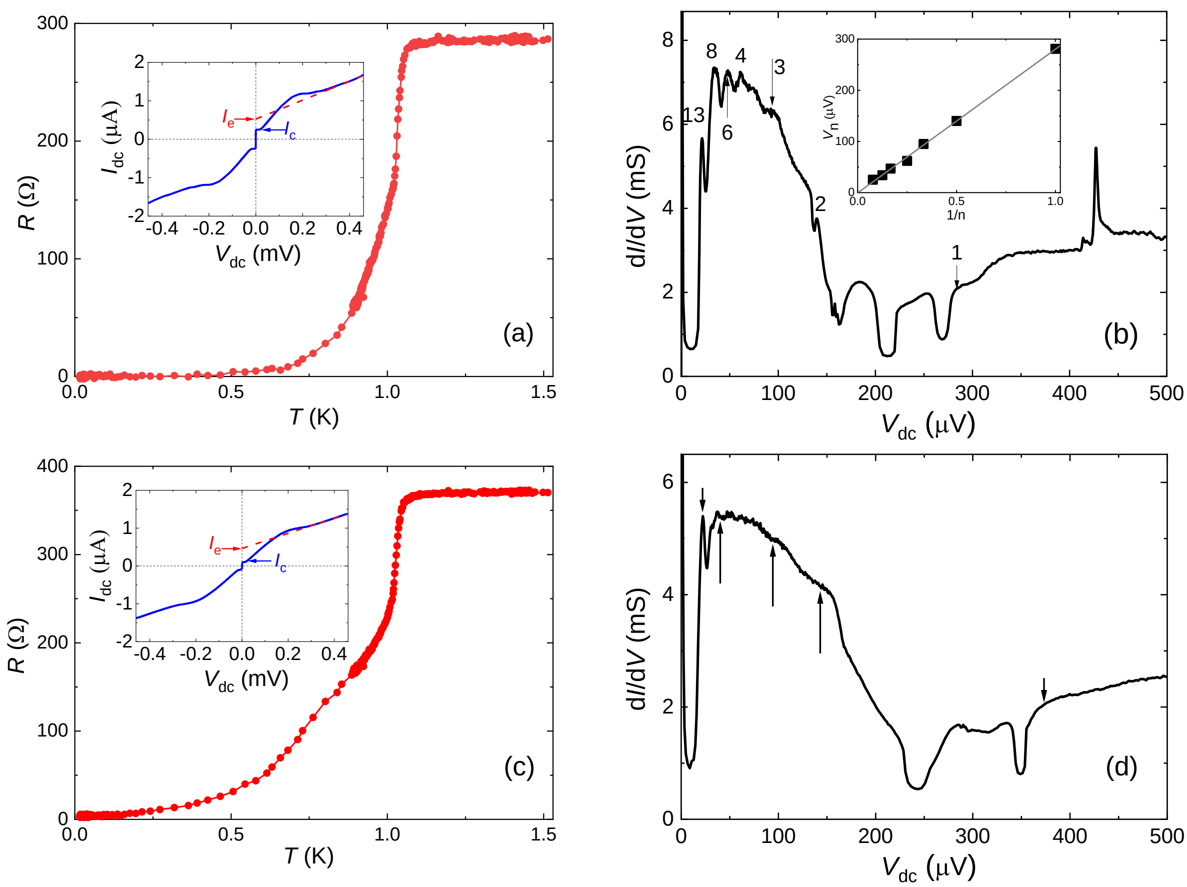

Figure 4.21: (a) T dependence of the junction resistance in device 2. Inset: $I - V$characteristics. (b) dI/dV as a function of the dc bias voltage V_{dc} in device 2. Inset: The voltage corresponding to the MAR peaks, V_n, plotted vs 1=n. (c) T dependence of the junction resistance in device 3. Inset: $I - V$characteristics. (d) dI/dV as a function of the dc bias voltage V_{dc} in device 3.

4.9 Shapiro-step data

4.9.1 Fractional ac Josephson effect

When an ac-driven Josephson junction is irradiated by an rf wave of frequency f, Shapiro steps [111] will be observed in the dc current–voltage curve at quantized voltages V_m equal to $\frac{mhf}{2e}$, where h is the Planck constant, and integer m is the step index (see Fig. 4.22(c)).

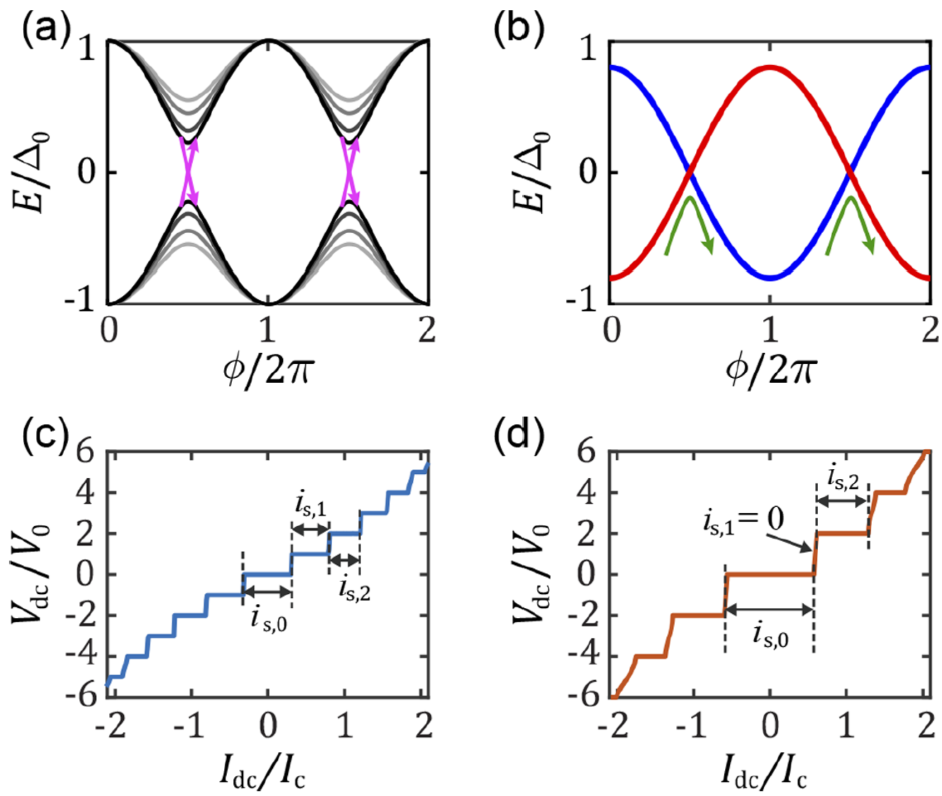

Figure 4.22: (a) Andreev bound states of a conventional Josephson junction with transparency $\tau = 0.7$, 0.8, 0.9, and 0.95. The higher the transparency, the smaller the gap size between two states. The magenta arrows represent the nonadiabatic transition between gapped ABSs. (b) The spectrum of MBS in a topological JJ. Example Shapiro steps under microwave irradiation for a JJ with 2π-periodicity (c) and 4π-periodicity (d). (modified from [112])

In an SNS JJ, Andreev reflections at the two SN interfaces share phase information if the coherence length is longer than the junction length. Thus a bound state called Andreev bound state (ABS) is formed in between the two SCs. The energy spectra of the ABS are

$$E_B(\phi) = \pm\Delta(T)\sqrt{1-\tau\sin^2\phi} \tag{4.5}$$

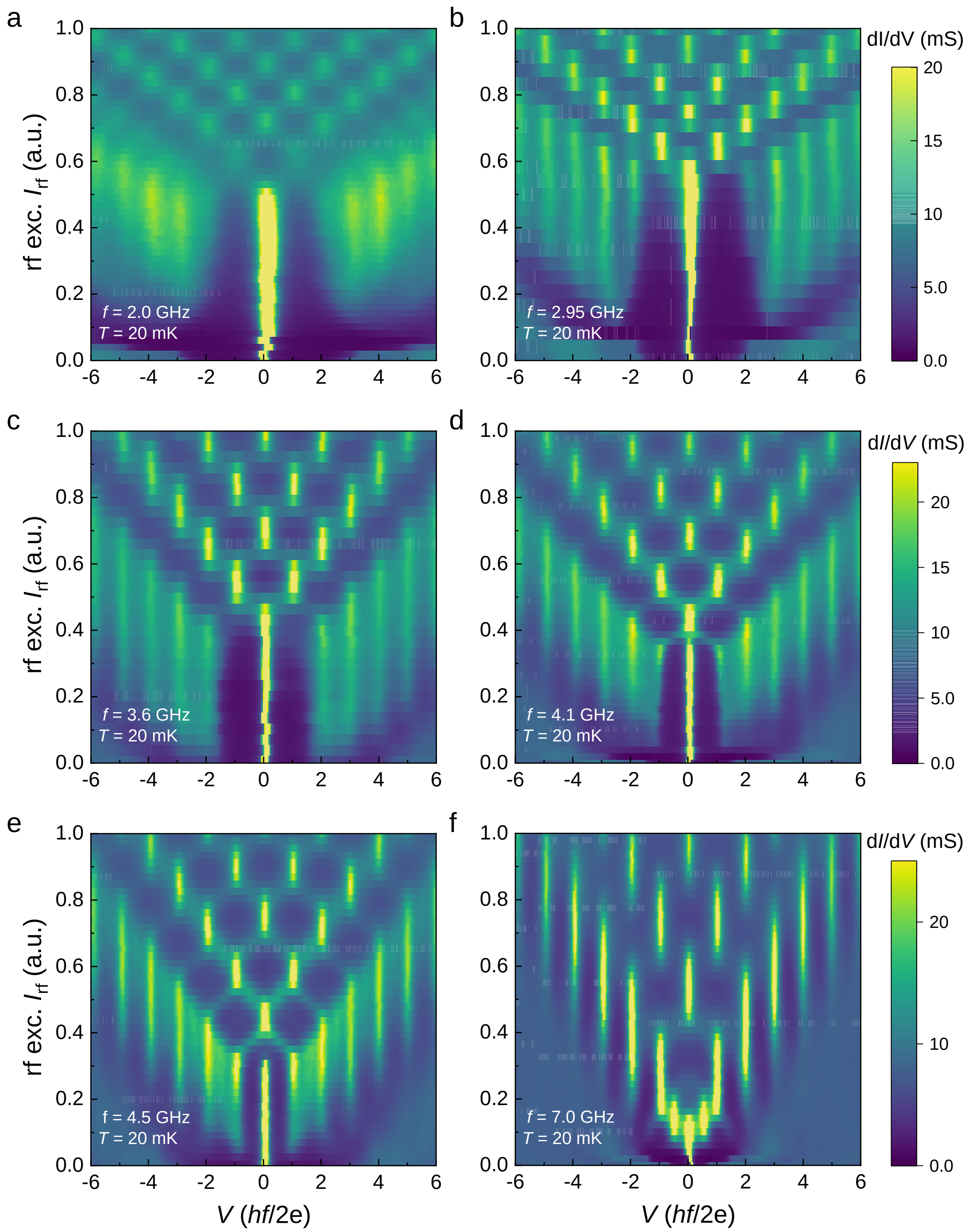

Figure 4.23: (a)-(f), Mapping of dI/dV measured under the irradiation of rf waves at various frequencies (2.0, 2.95, 3.6, 4.1, 4.5 and 7.0 GHz) as functions of rf excitation and the dc voltage V appearing on the JJ, which is normalized by $hf/2e$ to emphasize the Shapiro-step nature of the response.

where τ is the junction transparency, and Δ_T is the temperature-dependent superconducting gap. Fig. 4.22(a) shows the ABS spectra with transparency τ = 0.7, 0.8, 0.9, and 0.95. In a topological Josephson junction, Majorana bound states (MBSs) are expected [113–115]. The spectrum of MBS is gapless at $\phi = \pi$. Therefore the MBS is 4 π periodic, as shown in Fig. 4.22(b). In such a topological JJ with only a 4π periodicity, only even Shapiro steps are expected to be observed (see Fig. 4.22(d)). This is called the even/odd effect or fractional ac Josephson effect.

4.9.2 Frequency dependence of the Shapiro response

For Shapiro measurements, we did not measure the $I - V$ curves by dc multimeters but measured the differential resistance by lock-in amplifiers. Because the dc measurements have a low signal-to-noise ratio. When there is a plateau (Shapiro step) at V_m in the V vs I_{bias} curve, the slope of the curve, dV/dI, becomes zero at the plateau, which means that dI/dV diverges at V_m; therefore, as shown in Fig. 4.23 the yellow vertical lines occurring at regularly-spaced V are Shapiro steps.

As shown in Figs. 4.23(a)-(c), the $m = 1$ step is clearly missing at rf frequencies up to 3.6 GHz. The first Shapiro step is partially suppressed at f = 4.1 GHz (see Fig. 4.23(d)), while all the Shapiro steps are recovered starting from f = 4.5 GHz. As shown in Fig. 4.23(f), $m = 1/2$ step appears. Such subharmonic steps (for $m = p/q$ fractional value) have been reported [116, 117], the origins of this steps can be non-linearities, capacitance effects, or higher harmonics in the current-phase relation.

In device 1, the first Shapiro step is recovered as rf frequencies increases. Wiedenmann et al. [118] argued that the $m = 1$ step is missing only when f is smaller than the characteristic frequency $f_{4\pi} \equiv 2eR_N I_{4\pi}/h$, where $I_{4\pi}$ is the amplitude of the 4π-periodic current. The crossover frequency in our device 1 is around 4 GHz, suggesting $I_{4\pi} \approx 30$ nA. This gives the ratio $I_{4\pi}/\ I_C \approx 0.08$, where the 4π-periodic current is only a small part.

4.9.3 Temperature dependence of the Shapiro response

One can see that the $m = 2$ Shapiro step is also (partially) suppressed at low frequencies (see Figs. 4.23 (a) and (b)). This is due to the hysteretic $I - V$ characteristic of a JJ in the underdamped region [80]. This mechanism can also give rise to the missing of $m = 1$ Shapiro step. To rule out this mechanism, the data were taken at high temperatures. As shown in Fig. 4.25, differential resistance as a function of bias current was measured at 0.2 K, 0.4 K, 0.6 K and 0.8 K respectively. The curves were measured in two different sweep directions (up-sweep for red lines, down=sweep for blue lines). Hysteresis was observed at T = 0.2 K, 0.4 K, and 0.6 K, whereas it was gone at 0.8 K where the red curve and blue curve overlapped completely. We measured Shapiro data at T = 0.8 K, and f = 2.95 GHz, the $m = 1$ Shapiro step is still missing (see Fig. 4.24(d)). So, hysteresis is not the origin of the first step missing in our device.

The so-called quasiparticle-poisoning [119, 120] of the MBSs can be caused by thermal excitation. Therefore, the missing first Shapiro step is expected to be gradually recovered with increasing temperature [80, 121–123]. This behavior is observed in the temperature dependence

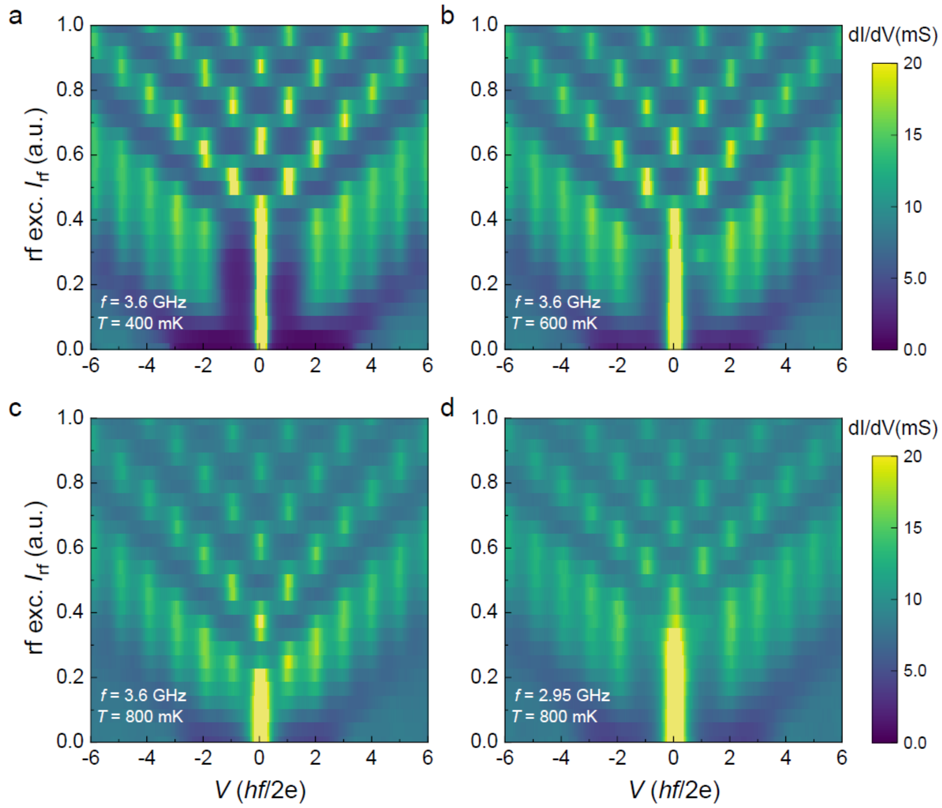

Figure 4.24: Shapiro response at higher temperatures. (a)-(c), Mapping of dI/dV as functions of rf power and observed voltage for the rf excitation with 3.6 GHz ((a), (b), (c)) and 2.95 GHz ((d)) at higher temperatures. At 800 mK, the dc $I-V$ characteristics is completely free from hysteresis. (modified from [89])

of f = 3.6 GHz Shapiro data, as shown in Figs. 4.24(a) - (c), giving support to the topological origin of the effect.

The missing Shapiro steps can also be due to Landau-Zener transitions (LZTs) [124]. And the probability of an LZT is

$$P = \exp\left(-\frac{\pi(1-\tau)\Delta}{eV}\right) \tag{4.6}$$

which is significant only when the junction transparency τ is close to 1 [125, 126]. However, our junction transparency is ~ 0.8, far from the ultra-high-transparency regime in which LZTs occur. Furthermore, the probabilities of Landau-Zener transitions increase with frequency, on the contrary, the first Shapiro step is missing only at low frequency [127]. Hence, the Shapiro-step data of our device strongly suggest a 4π-periodic contribution.

4.9.4 Reproducibity of the missing first Shapiro step

To reproduce the missing first Shapiro step, device 2 and device 3 are measured with a similar methodology as device 1. Fig. 4.26 (a) shows the Shapiro steps of device 2 measured at T =

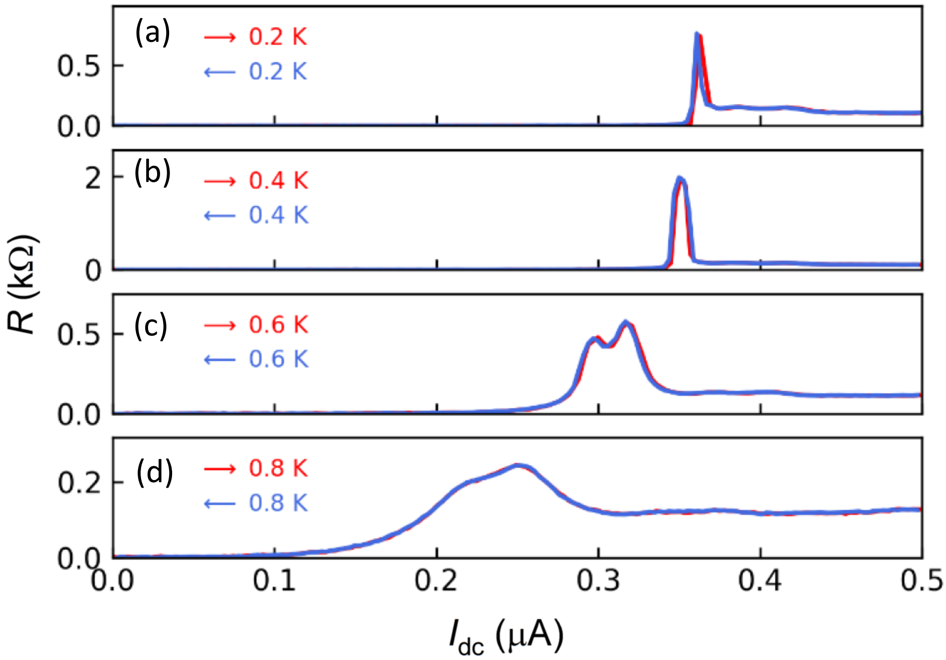

Figure 4.25: Hysteresis in the current response. a-d, Plots of dV/dI vs bias current I_{bias} at 0.2 K, 0.4 K, 0.6 K and 0.8 K, respectively. Red curves are sweep-up and blue curves are sweep-down. All curves were measured without magnetic field nor rf excitation. (modified from [89])

20 mK, f= 2.6 GHz. The m = -2 step is wider and brighter than the m = 2 step. This weak asymmetry at lower power is due to hysteretic $I-V$ characteristics. The asymmetry is no longer observed at T = 400 mK (see Fig. 4.26(b)), which means the hysteresis is gone. However, the first Shapiro step is still fully suppressed. In device 3, with the rf excitation at 2.3 GHz, even at T = 20 mK, the Shapiro steps are symmetric and there is no any hysteresis (Fig. 4.26(c)). The first Shapiro step is missing both at 20 mK and 400 mK. The phenomena of missing first Shapiro step is reproducible, which gives confidence in the intrinsic nature of the 4π-periodicity in our JJs.

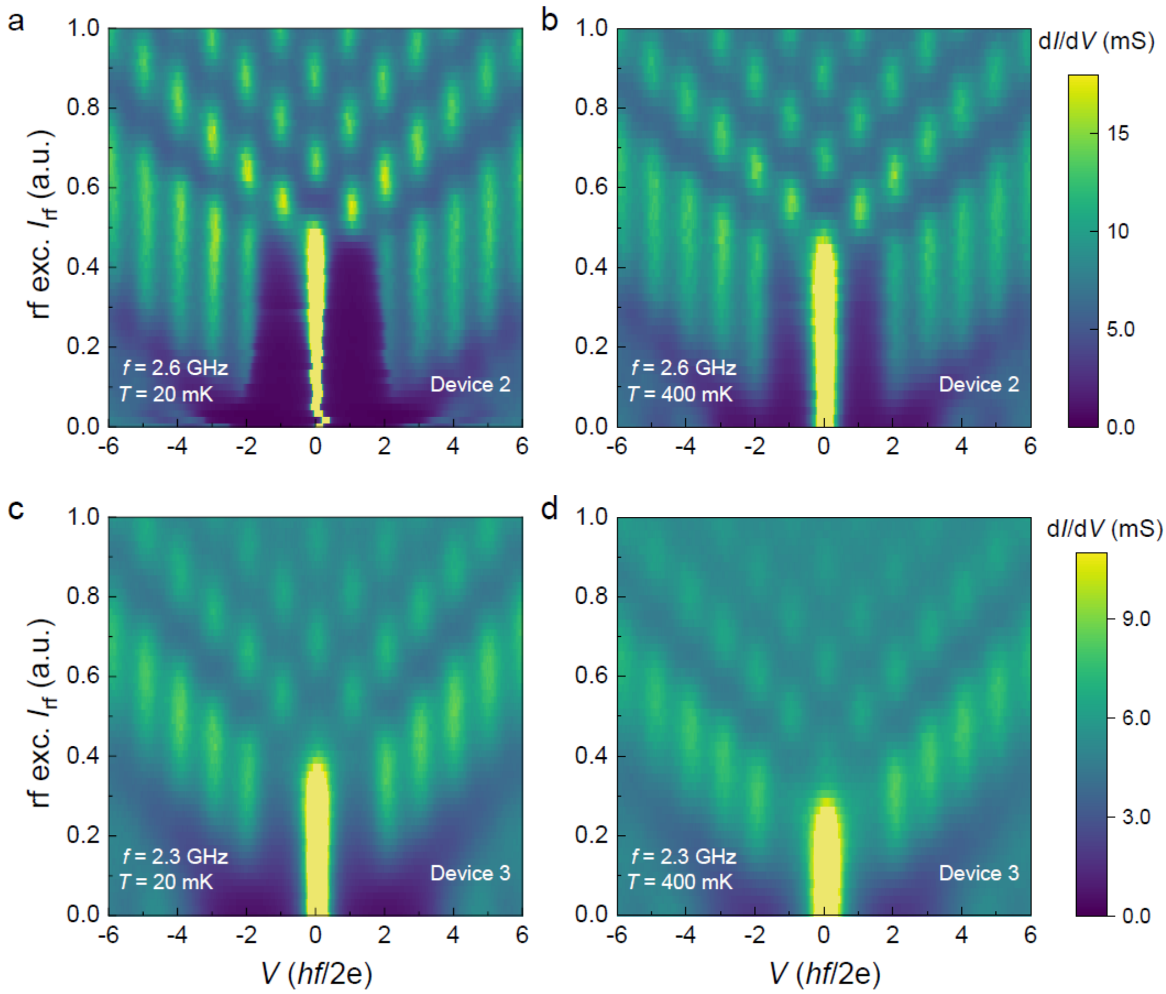

Figure 4.26: Shapiro response at higher temperatures. (a)-(c), Mapping of dI/dV as functions of rf power and observed voltage for the rf excitation with 3.6 GHz ((a), (b), (c)) and 2.95 GHz ((d)) at higher temperatures. At 800 mK, the dc I − V characteristics is completely free from hysteresis. (modified from [89])

4.10 Conclusion and outlook

In this chapter, we focused on the sandwich Josephson junctions. To characterize the Pd diffusion in the horizontal direction and the vertical direction in the BST film, we prepared specially designed Pd/BST bilayer samples for scanning tunneling electron microscope (STEM) measurements. The result is that Pd not only penetrates fully into the BST film beneath the Pd, but also propagates outward by ~90 nm from each edge. Which gives us the opportunity to fabricate sandwich JJs. The self-formed PdTe and $PdTe_2$ are confirmed by the image-simulation-based atomic structure analysis. And we got an "epitaxial" interface between BST and PdTe or $PdTe_2$.

The sandwich JJs have been charactrized by transport measurements. A robust proximity-induced superconductivity in the BST film is realized with a critical current of ~ 350 nA. As there is an "epitaxial" interface, the junction transparency is expected to be high. JJ transparency of 0.7 and 0.8 is estamited from Galaktionov and Zaikin's model and OTBK theory, respectively. Even though the transparency is not as high as in the planner JJs, the features resulting from multipe Andreev reflection (MAR) are observed. The MAR feature can still be observed at temperatures up to 1.0 K, which points to a strong superconducting proximity effect.

At the last part of this chapter, the Shapiro response is discussed. The missing first Shapiro step is observed in three devices. We proved that the origin of the missing first Shapiro step is neither hysteretic $I-V$ characteristic nor Landau-Zener transitions (LZTs). So the missing first Shapiro step can be evidence for topological Majorana bound states, although one can never nail them down with the Shapiro-step data alone.

In our STEM studies, we found that TI nanowires sandwiched by SCs are created. The width and thickness of the nanowires are smaller than 50 nm, which can be further decreased. Now, it remains a challenge to realize proximity-induced superconductivity in TI nanowires. Here, the characterization of the sandwich JJs shows that our TI nanowires are proximitized by the self-formed SCs successfully. Our superconducting TI nanowire provides a promising platform for researches on Majorana physics [128].

List of Figures

Bibliography

[1] M. König, S. Wiedmann, C. Brüne, A. Roth, H. Buhmann, L. W. Molenkamp, X.-L. Qi, and S.-C. Zhang, "Quantum spin Hall insulator state in Hgte quantum wells", Science **318**, 766 (2007) (cited on page 1).

[2] C. L. Kane and E. J. Mele, "Quantum spin hall effect in graphene", Physical review letters **95**, 226801 (2005) (cited on page 1).

[3] C. L. Kane and E. J. Mele, "Z_2 Topological order and the quantum spin Hall effect", Physical review letters **95**, 146802 (2005) (cited on page 1).

[4] B. A. Bernevig and S.-C. Zhang, "Quantum spin hall effect", Physical review letters **96**, 106802 (2006) (cited on page 1).

[5] L. Fu and C. L. Kane, "Topological insulators with inversion symmetry", Physical Review B **76**, 045302 (2007) (cited on page 1).

[6] D. Hsieh, D. Qian, L. Wray, Y. Xia, Y. S. Hor, R. J. Cava, and M. Z. Hasan, "A topological Dirac insulator in a quantum spin Hall phase", Nature **452**, 970 (2008) (cited on page 1).

[7] L. Fu and C. L. Kane, "Superconducting proximity effect and Majorana fermions at the surface of a topological insulator", Physical review letters **100**, 096407 (2008) (cited on pages 1, 25).

[8] J. Alicea, "New directions in the pursuit of majorana fermions in solid state systems", Reports on progress in physics **75**, 076501 (2012) (cited on page 1).

[9] F. Wilczek, "Majorana returns", Nature Physics **5**, 614 (2009) (cited on page 1).

[10] C. Nayak, S. H. Simon, A. Stern, M. Freedman, and S. D. Sarma, "Non-Abelian anyons and topological quantum computation", Reviews of Modern Physics **80**, 1083 (2008) (cited on pages 1, 38).

[11] N. Read and D. Green, "Paired states of fermions in two dimensions with breaking of parity and time-reversal symmetries and the fractional quantum Hall effect", Physical Review B **61**, 10267 (2000) (cited on page 1).

[12] J. Jang, D. Ferguson, V. Vakaryuk, R. Budakian, S. Chung, P. Goldbart, and Y. Maeno, "Observation of half-height magnetization steps in Sr_2RuO_4", Science **331**, 186 (2011) (cited on page 1).

[13] H. Zhang, C.-X. Liu, S. Gazibegovic, D. Xu, J. A. Logan, G. Wang, N. van Loo, J. D. Bommer, M. W. de Moor, D. Car, et al., "Retraction note: quantized majorana conductance", Nature **591**, E30 (2021) (cited on page 1).

[14] Q. L. He, L. Pan, A. L. Stern, E. C. Burks, X. Che, G. Yin, J. Wang, B. Lian, Q. Zhou, E. S. Choi, et al., "Chiral majorana fermion modes in a quantum anomalous hall insulator–superconductor structure", Science **357**, 294 (2017) (cited on page 1).

[15] A. Zorin, "The thermocoax cable as the microwave frequency filter for single electron circuits", Review of Scientific Instruments **66**, 4296 (1995) (cited on page 4).

[16] H. le Sueur and P. Joyez, “Microfabricated electromagnetic filters for millikelvin experiments”, Review of scientific instruments **77**, 115102 (2006) (cited on page 4).

[17] I. Jin, A. Amar, and F. Wellstood, “Distributed microwave damping filters for superconducting quantum interference devices”, Applied physics letters **70**, 2186 (1997) (cited on page 4).

[18] J. M. Martinis, M. H. Devoret, and J. Clarke, “Experimental tests for the quantum behavior of a macroscopic degree of freedom: The phase difference across a josephson junction”, Physical Review B **35**, 4682 (1987) (cited on page 4).

[19] K. Bladh, D. Gunnarsson, E. Hürfeld, S. Devi, C. Kristoffersson, B. Smålander, S. Pehrson, T. Claeson, P. Delsing, and M. Taslakov, “Comparison of cryogenic filters for use in single electronics experiments”, Review of Scientific Instruments **74**, 1323 (2003) (cited on page 4).

[20] A. Lukashenko and A. Ustinov, “Improved powder filters for qubit measurements”, Review of Scientific Instruments **79**, 014701 (2008) (cited on page 5).

[21] D. L.-I. Amplifier, “MODEL SR830”, Interface **4**, 24 (1993) (cited on page 6).

[22] H. Zhang, C.-X. Liu, X.-L. Qi, X. Dai, Z. Fang, and S.-C. Zhang, “Topological insulators in Bi_2Se_3, Bi_2Te_3 and Sb_2Te_3 with a single Dirac cone on the surface”, Nature physics **5**, 438 (2009) (cited on page 10).

[23] C. Weyrich, M. Drögeler, J. Kampmeier, M. Eschbach, G. Mussler, T. Merzenich, T. Stoica, I. Batov, J. Schubert, L. Plucinski, et al., “Growth, characterization, and transport properties of ternary $(Bi_{1-x}Sb_x)_2Te_3$ topological insulator layers”, Journal of Physics: Condensed Matter **28**, 495501 (2016) (cited on page 10).

[24] J. Zhang, C.-Z. Chang, Z. Zhang, J. Wen, X. Feng, K. Li, M. Liu, K. He, L. Wang, X. Chen, et al., “Band structure engineering in $(Bi_{1-x}Sb_x)_2Te_3$ ternary topological insulators”, Nature communications **2**, 1 (2011) (cited on page 10).

[25] J. Zhang, X. Feng, Y. Xu, M. Guo, Z. Zhang, Y. Ou, Y. Feng, K. Li, H. Zhang, L. Wang, et al., “Disentangling the magnetoelectric and thermoelectric transport in topological insulator thin films”, Physical Review B **91**, 075431 (2015) (cited on page 10).

[26] A. Bliesener, “Molecular beam epitaxy growth of topological materials”, PhD thesis (Universität zu Köln, 2020) (cited on page 10).

[27] M. Bai, F. Yang, M. Luysberg, J. Feng, A. Bliesener, G. Lippertz, A. Taskin, J. Mayer, and Y. Ando, “Novel self-epitaxy for inducing t superconductivity in the topological insulator $(Bi_{1-x}Sb_x)_2Te_3$”, Physical Review Materials **4**, 094801 (2020) (cited on pages 10, 12, 14, 15, 18, 19, 26, 27, 29, 33–35).

[28] N. Pala and M. Karabiyik, “Electron beam lithography (EBL)”, 2016 (cited on page 10).

[29] S. Yasin, D. Hasko, and H. Ahmed, “Comparison of MIBK/IPA and water/IPA as PMMA developers for electron beam nanolithography”, Microelectronic engineering **61**, 745 (2002) (cited on page 10).

[30] S. Ghatak, O. Breunig, F. Yang, Z. Wang, A. A. Taskin, and Y. Ando, "Anomalous Fraunhofer patterns in gated Josephson junctions based on the bulk-insulating topological insulator $BiSbTeSe_2$", Nano letters **18**, 5124 (2018) (cited on pages 13, 26, 27, 29, 35, 37, 55, 62).

[31] Ö. Gül, H. Zhang, F. K. de Vries, J. van Veen, K. Zuo, V. Mourik, S. Conesa-Boj, M. P. Nowak, D. J. van Woerkom, M. Quintero-Pérez, et al., "Hard superconducting gap in InSb nanowires", Nano letters **17**, 2690 (2017) (cited on page 13).

[32] J. Guggenheim, F. Hulliger, and J. Muller, "$PdTe_2$, a superconductor with CdI_2 structure", Helv. Phys. Acta **34**, 408 (1961) (cited on page 13).

[33] A. Kjekshus and W. Pearson, "Constitution and magnetic and electrical properties of palladium tellurides (PdTe–$PdTe_2$)", Canadian Journal of Physics **43**, 438 (1965) (cited on page 13).

[34] C. J. Raub, V. Compton, T. Geballe, B. Matthias, J. Maita, and G. Hull Jr, "The occurrence of superconductivity in sulfides, selenides, tellurides of Pt-group metals", Journal of Physics and Chemistry of Solids **26**, 2051 (1965) (cited on page 13).

[35] Y. Wang, J. Zhang, W. Zhu, Y. Zou, C. Xi, L. Ma, T. Han, J. Yang, J. Wang, J. Xu, et al., "De Hass-van Alphen and magnetoresistance reveal predominantly single-band transport behavior in $PdTe_2$", Scientific reports **6**, 1 (2016) (cited on page 13).

[36] V. Ginzburg, "Fiz. tverd. Tela & 2031 (1960)", Soviet Phys.-Solid State **3**, 1824 (1960) (cited on page 13).

[37] C. Liu, C.-S. Lian, M.-H. Liao, Y. Wang, Y. Zhong, C. Ding, W. Li, C.-L. Song, K. He, X.-C. Ma, et al., "Two-dimensional superconductivity and topological states in $PdTe_2$ thin films", Physical Review Materials **2**, 094001 (2018) (cited on page 13).

[38] H. Leng, C. Paulsen, Y. Huang, and A. De Visser, "Type-I superconductivity in the Dirac semimetal $PdTe_2$", Physical Review B **96**, 220506 (2017) (cited on pages 13, 36).

[39] F. Fei, X. Bo, R. Wang, B. Wu, J. Jiang, D. Fu, M. Gao, H. Zheng, Y. Chen, X. Wang, et al., "Nontrivial Berry phase and type-II Dirac transport in the layered material $PdTe_2$", Physical Review B **96**, 041201 (2017) (cited on page 13).

[40] H.-J. Noh, J. Jeong, E.-J. Cho, K. Kim, B. Min, and B.-G. Park, "Experimental realization of type-II Dirac fermions in a $PdTe_2$ superconductor", Physical review letters **119**, 016401 (2017) (cited on pages 13, 14).

[41] S. Das, A. Sirohi, L. Yadav, S. Gayen, Y. Singh, G. Sheet, et al., "Conventional superconductivity in the type-II Dirac semimetal $PdTe_2$", Physical Review B **97**, 014523 (2018) (cited on page 14).

[42] J. Voerman, J. De Boer, T. Hashimoto, Y. Huang, C. Li, and A. Brinkman, "Dominant s-wave superconducting gap in $PdTe_2$ observed by tunneling spectroscopy on side junctions", Physical Review B **99**, 014510 (2019) (cited on page 14).

[43] N. Werthamer, E. Helfand, and P. Hohenberg, “Temperature and purity dependence of the superconducting critical field, H_{C2}. III. Electron spin and spin-orbit effects”, Physical Review **147**, 295 (1966) (cited on page 14).

[44] M. Von Ardenne, “Das elektronen-rastermikroskop”, Zeitschrift für Physik **109**, 553 (1938) (cited on page 16).

[45] P. D. Nellist, “Scanning transmission electron microscopy”, in *Science of microscopy* (Springer, 2007), pp. 65–132 (cited on page 16).

[46] S. Findlay, N. Shibata, H. Sawada, E. Okunishi, Y. Kondo, and Y. Ikuhara, “Dynamics of annular bright field imaging in scanning transmission electron microscopy”, Ultramicroscopy **110**, 903 (2010) (cited on page 17).

[47] B. D. Josephson, “Possible new effects in superconductive tunnelling”, Physics letters **1**, 251 (1962) (cited on page 20).

[48] B. D. Josephson, “The discovery of tunnelling supercurrents”, Reviews of Modern Physics **46**, 251 (1974) (cited on page 20).

[49] M. Tinkham, “Introduction to superconductivity” (Courier Corporation, 2004) (cited on page 21).

[50] B. Pannetier and H. Courtois, “Andreev reflection and proximity effect”, Journal of low temperature physics **118**, 599 (2000) (cited on page 22).

[51] A. Andreev, “The thermal conductivity of the intermediate state in superconductors”, Soviet Physics Jetp-Ussr, **46**, 1823 (1964) (cited on page 22).

[52] G. Blonder, m. M. Tinkham, and k. T. Klapwijk, “Transition from metallic to tunneling regimes in superconducting microconstrictions: Excess current, charge imbalance, and supercurrent conversion”, Physical Review B **25**, 4515 (1982) (cited on pages 22, 23).

[53] M. Octavio, M. Tinkham, G. Blonder, and T. Klapwijk, “Subharmonic energy-gap structure in superconducting constrictions”, Physical Review B **27**, 6739 (1983) (cited on pages 24, 35, 37, 62).

[54] K. Flensberg, J. B. Hansen, and M. Octavio, “Subharmonic energy-gap structure in superconducting weak links”, Physical Review B **38**, 8707 (1988) (cited on pages 24, 35).

[55] G. Niebler, G. Cuniberti, and T. Novotny, “Analytical calculation of the excess current in the OTBK theory”, arXiv preprint arXiv:0905.4852 (2009) (cited on page 24).

[56] M. Z. Hasan and C. L. Kane, “Colloquium: topological insulators”, Reviews of modern physics **82**, 3045 (2010) (cited on page 25).

[57] X.-L. Qi and S.-C. Zhang, “Topological insulators and superconductors”, Reviews of Modern Physics **83**, 1057 (2011) (cited on page 25).

[58] Y. Ando, “Topological insulator materials”, Journal of the Physical Society of Japan **82**, 102001 (2013) (cited on page 25).

[59] P. A. Rosenthal, M. Beasley, K. Char, M. Colclough, and G. Zaharchuk, "Flux focusing effects in planar thin-film grain-boundary Josephson junctions", Applied physics letters **59**, 3482 (1991) (cited on page 26).

[60] F. Qu, F. Yang, J. Shen, Y. Ding, J. Chen, Z. Ji, G. Liu, J. Fan, X. Jing, C. Yang, et al., "Strong superconducting proximity effect in Pb-Bi_2Te_3 hybrid structures", Scientific reports **2**, 1 (2012) (cited on pages 26, 55).

[61] J. Williams, A. Bestwick, P. Gallagher, S. S. Hong, Y. Cui, A. S. Bleich, J. Analytis, I. Fisher, and D. Goldhaber-Gordon, "Unconventional Josephson effect in hybrid superconductor-topological insulator devices", Physical review letters **109**, 056803 (2012) (cited on pages 26, 27, 55).

[62] J. H. Lee, G.-H. Lee, J. Park, J. Lee, S.-G. Nam, Y.-S. Shin, J. S. Kim, and H.-J. Lee, "Local and nonlocal Fraunhofer-like pattern from an edge-stepped topological surface Josephson current distribution", Nano letters **14**, 5029 (2014) (cited on pages 26, 27).

[63] E. Bocquillon, R. S. Deacon, J. Wiedenmann, P. Leubner, T. M. Klapwijk, C. Brüne, K. Ishibashi, H. Buhmann, and L. W. Molenkamp, "Gapless Andreev bound states in the quantum spin Hall insulator HgTe", Nature Nanotechnology **12**, 137 (2017) (cited on pages 26, 27).

[64] H. Suominen, J. Danon, M. Kjaergaard, K. Flensberg, J. Shabani, C. Palmstrøm, F. Nichele, and C. Marcus, "Anomalous Fraunhofer interference in epitaxial superconductor-semiconductor Josephson junctions", Physical Review B **95**, 035307 (2017) (cited on pages 26, 27).

[65] B. Baxevanis, V. Ostroukh, and C. Beenakker, "Even-odd flux quanta effect in the fraunhofer oscillations of an edge-channel Josephson junction", Physical Review B **91**, 041409 (2015) (cited on page 27).

[66] A. C. Potter and L. Fu, "Anomalous supercurrent from majorana states in topological insulator Josephson junctions", Physical Review B **88**, 121109 (2013) (cited on page 27).

[67] L. A. Jauregui, M. Kayyalha, A. Kazakov, I. Miotkowski, L. P. Rokhinson, and Y. P. Chen, "Gate-tunable supercurrent and multiple Andreev reflections in a superconductor-topological insulator nanoribbon-superconductor hybrid device", Applied Physics Letters **112**, 093105 (2018) (cited on pages 29, 35, 55, 62).

[68] D. McCumber, "Effect of ac impedance on dc voltage-current characteristics of superconductor weak-link junctions", Journal of Applied Physics **39**, 3113 (1968) (cited on page 30).

[69] S. Chakravarty, G.-L. Ingold, S. Kivelson, and G. Zimanyi, "Quantum statistical mechanics of an array of resistively shunted Josephson junctions", Physical Review B **37**, 3283 (1988) (cited on page 30).

[70] W. Stewart, "Current-voltage characteristics of Josephson junctions", Applied physics letters **12**, 277 (1968) (cited on page 30).

[71] B. Chesca, R. Kleiner, and D. Koelle, “SQUID theory”, The SQUID Handbook: Fundamentals and Technology of SQUIDs and SQUID Systems **1**, 29 (2004) (cited on page 33).

[72] R. Cantor and D. Koelle, “The SQUID Handbook vol 1, ed J Clarke and AI Braginski”, 2004 (cited on page 33).

[73] M. Kjærgaard, H. J. Suominen, M. Nowak, A. Akhmerov, J. Shabani, C. Palmstrøm, F. Nichele, and C. M. Marcus, “Transparent semiconductor-superconductor interface and induced gap in an epitaxial heterostructure Josephson junction”, Physical Review Applied **7**, 034029 (2017) (cited on page 34).

[74] C. Nguyen, H. Kroemer, and E. L. Hu, “Anomalous Andreev conductance in InAs-AlSb quantum well structures with Nb electrodes”, Physical review letters **69**, 2847 (1992) (cited on page 34).

[75] C. Nguyen, H. Kroemer, and E. L. Hu, “Contact resistance of superconductor-semiconductor interfaces: The case of Nb-InAs/AlSb quantum-well structures”, Applied physics letters **65**, 103 (1994) (cited on page 34).

[76] M. Veldhorst, M. Snelder, M. Hoek, T. Gang, V. Guduru, X. Wang, U. Zeitler, W. G. van der Wiel, A. Golubov, H. Hilgenkamp, et al., “Josephson supercurrent through a topological insulator surface state”, Nature materials **11**, 417 (2012) (cited on pages 35, 55).

[77] J. B. Oostinga, L. Maier, P. Schüffelgen, D. Knott, C. Ames, C. Brüne, G. Tkachov, H. Buhmann, and L. W. Molenkamp, “Josephson supercurrent through the topological surface states of strained bulk HgTe”, Physical Review X **3**, 021007 (2013) (cited on pages 35, 37, 55).

[78] L. Galletti, S. Charpentier, M. Iavarone, P. Lucignano, D. Massarotti, R. Arpaia, Y. Suzuki, K. Kadowaki, T. Bauch, A. Tagliacozzo, et al., “Influence of topological edge states on the properties of Al/Bi_2Se_3/Al hybrid Josephson devices”, Physical Review B **89**, 134512 (2014) (cited on pages 35, 55).

[79] M. Snelder, C. Molenaar, Y. Pan, D. Wu, Y. Huang, A. de Visser, A. Golubov, W. van der Wiel, H. Hilgenkamp, M. Golden, et al., “Josephson supercurrent in a topological insulator without a bulk shunt”, Superconductor science and technology **27**, 104001 (2014) (cited on pages 35, 55).

[80] P. Schüffelgen, D. Rosenbach, C. Li, T. W. Schmitt, M. Schleenvoigt, A. R. Jalil, S. Schmitt, J. Kölzer, M. Wang, B. Bennemann, et al., “Selective area growth and stencil lithography for in situ fabricated quantum devices”, Nature nanotechnology **14**, 825 (2019) (cited on pages 35, 37, 55, 68).

[81] N. W. Ashcroft, N. D. Mermin, et al., “Solid state physics” (cited on page 36).

[82] A. Kleinsasser, R. Miller, W. Mallison, and G. Arnold, “Observation of multiple Andreev reflections in superconducting tunnel junctions”, Physical review letters **72**, 1738 (1994) (cited on page 37).

[83] B. Aminov, A. Golubov, and M. Y. Kupriyanov, "Quasiparticle current in ballistic constrictions with finite transparencies of interfaces", Physical Review B **53**, 365 (1996) (cited on page 37).

[84] R. M. Lutchyn, E. P. Bakkers, L. P. Kouwenhoven, P. Krogstrup, C. M. Marcus, and Y. Oreg, "Majorana zero modes in superconductor–semiconductor heterostructures", Nature Reviews Materials **3**, 52 (2018) (cited on page 38).

[85] M.-X. Wang, C. Liu, J.-P. Xu, F. Yang, L. Miao, M.-Y. Yao, C. Gao, C. Shen, X. Ma, X. Chen, et al., "The coexistence of superconductivity and topological order in the Bi_2Se_3 thin films", Science **336**, 52 (2012) (cited on page 38).

[86] E. Wang, H. Ding, A. V. Fedorov, W. Yao, Z. Li, Y.-F. Lv, K. Zhao, L.-G. Zhang, Z. Xu, J. Schneeloch, et al., "Fully gapped topological surface states in Bi_2Se_3 films induced by a d-wave high-temperature superconductor", Nature physics **9**, 621 (2013) (cited on page 38).

[87] J.-P. Xu, C. Liu, M.-X. Wang, J. Ge, Z.-L. Liu, X. Yang, Y. Chen, Y. Liu, Z.-A. Xu, C.-L. Gao, et al., "Artificial topological superconductor by the proximity effect", Physical Review Letters **112**, 217001 (2014) (cited on page 38).

[88] S.-Y. Xu, N. Alidoust, I. Belopolski, A. Richardella, C. Liu, M. Neupane, G. Bian, S.-H. Huang, R. Sankar, C. Fang, et al., "Momentum-space imaging of Cooper pairing in a half-Dirac-gas topological superconductor", Nature Physics **10**, 943 (2014) (cited on page 38).

[89] M. Bai, X.-K. Wei, J. Feng, M. Luysberg, A. Bliesener, G. Lippertz, A. Uday, A. Taskin, J. Mayer, and Y. Ando, "Novel realization of superconducting topological-insulator nanowires", arXiv preprint arXiv:2108.08559 (2021) (cited on pages 41, 46, 49, 50, 54–56, 58–60, 63, 64, 69–71).

[90] J. Barthel, "Dr. Probe: A software for high-resolution STEM image simulation", Ultramicroscopy **193**, 1 (2018) (cited on page 42).

[91] P. Nellist and S. Pennycook, "The principles and interpretation of annular dark-field Z-contrast imaging", Advances in imaging and electron physics **113**, 147 (2000) (cited on page 44).

[92] T. Finlayson, W. Reichardt, and H. Smith, "Lattice dynamics of layered-structure compounds: $PdTe_2$", Physical Review B **33**, 2473 (1986) (cited on page 47).

[93] R. A. Webb, S. Washburn, C. Umbach, and R. Laibowitz, "Observation of h/e Aharonov-Bohm oscillations in normal-metal rings", Physical Review Letters **54**, 2696 (1985) (cited on page 53).

[94] S. Cho, B. Dellabetta, R. Zhong, J. Schneeloch, T. Liu, G. Gu, M. J. Gilbert, and N. Mason, "Aharonov–Bohm oscillations in a quasi-ballistic three-dimensional topological insulator nanowire", Nature communications **6**, 1 (2015) (cited on page 53).

[95] M. Brahlek, N. Koirala, N. Bansal, and S. Oh, "Transport properties of topological insulators: Band bending, bulk metal-to-insulator transition, and weak anti-localization", Solid State Communications **215**, 54 (2015) (cited on page 54).

[96] F. Yang, A. Taskin, S. Sasaki, K. Segawa, Y. Ohno, K. Matsumoto, and Y. Ando, "Dual-gated topological insulator thin-film device for efficient fermi-level tuning", Acs Nano **9**, 4050 (2015) (cited on page 54).

[97] S. Cho, B. Dellabetta, A. Yang, J. Schneeloch, Z. Xu, T. Valla, G. Gu, M. J. Gilbert, and N. Mason, "Symmetry protected Josephson supercurrents in three-dimensional topological insulators", Nature communications **4**, 1 (2013) (cited on page 55).

[98] Y. Takeshige, S. Matsuo, R. S. Deacon, K. Ueda, Y. Sato, Y.-F. Zhao, L. Zhou, C.-Z. Chang, K. Ishibashi, and S. Tarucha, "Experimental study of ac josephson effect in gate-tunable $(Bi_{1-x}Sb_x)_2Te_3$ thin-film josephson junctions", Physical Review B **101**, 115410 (2020) (cited on page 55).

[99] M. P. Stehno, P. Ngabonziza, H. Myoren, and A. Brinkman, "Josephson effect and charge distribution in thin Bi_2Te_3 topological insulators", Advanced materials **32**, 1908351 (2020) (cited on page 55).

[100] I. Kulik and A. Omel'Yanchuk, "Properties of superconducting microbridges in the pure limit", Sov. J. Low Temp. Phys.(Engl. Transl.);(United States) **3** (1977) (cited on page 56).

[101] G.-H. Lee, S. Kim, S.-H. Jhi, and H.-J. Lee, "Ultimately short ballistic vertical graphene Josephson junctions", Nature communications **6**, 1 (2015) (cited on page 56).

[102] A. V. Galaktionov and A. D. Zaikin, "Quantum interference and supercurrent in multiple-barrier proximity structures", Physical Review B **65**, 184507 (2002) (cited on page 56).

[103] X. He, H. Li, L. Chen, and K. Wu, "Substitution-induced spin-splitted surface states in topological insulator $(Bi_{1-x}Sb_x)_2Te_3$", Scientific reports **5**, 1 (2015) (cited on page 57).

[104] T. Klapwijk, G. Blonder, and M. Tinkham, "Explanation of subharmonic energy gap structure in superconducting contacts", Physica B+ C **109**, 1657 (1982) (cited on page 61).

[105] E. Bratus, V. Shumeiko, and G. Wendin, "Theory of subharmonic gap structure in superconducting mesoscopic tunnel contacts", Physical review letters **74**, 2110 (1995) (cited on page 61).

[106] A. Zaitsev and D. Averin, "Theory of αc Josephson effect in superconducting constrictions", Physical review letters **80**, 3602 (1998) (cited on page 61).

[107] X. Du, I. Skachko, and E. Y. Andrei, "Josephson current and multiple Andreev reflections in graphene SNS junctions", Physical Review B **77**, 184507 (2008) (cited on page 62).

[108] J. Xiang, A. Vidan, M. Tinkham, R. M. Westervelt, and C. M. Lieber, "Ge/Si nanowire mesoscopic Josephson junctions", Nature nanotechnology **1**, 208 (2006) (cited on page 62).

[109] G. Rickayzen, "Theory of superconductivity", American Journal of Physics **33**, 978 (1965) (cited on page 63).

[110] U. S. Pracht, E. Heintze, C. Clauss, D. Hafner, R. Bek, D. Werner, S. Gelhorn, M. Scheffler, M. Dressel, D. Sherman, et al., "Electrodynamics of the superconducting state in ultra-thin films at THz frequencies", IEEE Transactions on Terahertz Science and Technology **3**, 269 (2013) (cited on page 63).

[111] S. Shapiro, "Josephson currents in superconducting tunneling: The effect of microwaves and other observations", Physical Review Letters **11**, 80 (1963) (cited on page 66).

[112] J. Park, Y.-B. Choi, G.-H. Lee, and H.-J. Lee, "Characterization of Shapiro steps in the presence of a 4π-periodic Josephson current", arXiv preprint arXiv:2103.16113 (2021) (cited on page 66).

[113] A. Y. Kitaev, "Unpaired Majorana fermions in quantum wires", Physics-uspekhi **44**, 131 (2001) (cited on page 68).

[114] L. Fu and C. L. Kane, "Josephson current and noise at a superconductor/quantum-spin-Hall-insulator/superconductor junction", Physical Review B **79**, 161408 (2009) (cited on page 68).

[115] R. M. Lutchyn, J. D. Sau, and S. D. Sarma, "Majorana fermions and a topological phase transition in semiconductor-superconductor heterostructures", Physical review letters **105**, 077001 (2010) (cited on page 68).

[116] P. Dubos, H. Courtois, O. Buisson, and B. Pannetier, "Coherent low-energy charge transport in a diffusive SNS junction", Physical review letters **87**, 206801 (2001) (cited on page 68).

[117] M. Chauvin, P. Vom Stein, H. Pothier, P. Joyez, M. Huber, D. Esteve, and C. Urbina, "Superconducting atomic contacts under microwave irradiation", Physical review letters **97**, 067006 (2006) (cited on page 68).

[118] J. Wiedenmann, E. Bocquillon, R. S. Deacon, S. Hartinger, O. Herrmann, T. M. Klapwijk, L. Maier, C. Ames, C. Brüne, C. Gould, et al., "4 π-periodic josephson supercurrent in HgTe-based topological Josephson junctions", Nature communications **7**, 1 (2016) (cited on page 68).

[119] P. Joyez, P. Lafarge, A. Filipe, D. Esteve, and M. Devoret, "Observation of parity-induced suppression of Josephson tunneling in the superconducting single electron transistor", Physical review letters **72**, 2458 (1994) (cited on page 68).

[120] L. Bretheau, Ç. Girit, C. Urbina, D. Esteve, and H. Pothier, "Supercurrent spectroscopy of Andreev states", Physical Review X **3**, 041034 (2013) (cited on page 68).

[121] K. Le Calvez, L. Veyrat, F. Gay, P. Plaindoux, C. B. Winkelmann, H. Courtois, and B. Sacépé, "Joule overheating poisons the fractional ac josephson effect in topological Josephson junctions", Communications Physics **2**, 1 (2019) (cited on page 68).

[122] B. De Ronde, C. Li, Y. Huang, and A. Brinkman, "Induced topological superconductivity in a $BiSbTeSe_2$-based Josephson junction", Nanomaterials **10**, 794 (2020) (cited on page 68).

[123] D. Rosenbach, T. W. Schmitt, P. Schüffelgen, M. P. Stehno, C. Li, M. Schleenvoigt, A. R. Jalil, G. Mussler, E. Neumann, S. Trellenkamp, et al., "Reappearance of first Shapiro step in narrow topological Josephson junctions", Science Advances **7**, eabf1854 (2021) (cited on page 68).

[124] F. Dominguez, F. Hassler, and G. Platero, "Dynamical detection of Majorana fermions in current-biased nanowires", Physical Review B **86**, 140503 (2012) (cited on page 69).

[125] D. Averin and A. Bardas, "Ac Josephson effect in a single quantum channel", Physical review letters **75**, 1831 (1995) (cited on page 69).

[126] M. C. Dartiailh, J. J. Cuozzo, B. H. Elfeky, W. Mayer, J. Yuan, K. S. Wickramasinghe, E. Rossi, and J. Shabani, "Missing Shapiro steps in topologically trivial Josephson junction on InAs quantum well", Nature communications **12**, 1 (2021) (cited on page 69).

[127] J. D. Sau, E. Berg, and B. I. Halperin, "On the possibility of the fractional ac Josephson effect in non-topological conventional superconductor-normal-superconductor junctions", arXiv preprint arXiv:1206.4596 (2012) (cited on page 69).

[128] H. F. Legg, D. Loss, and J. Klinovaja, "Majorana bound states in topological insulators without a vortex", arXiv preprint arXiv:2103.13412 (2021) (cited on page 72).

Acknowledgments

At first, I wish to express sincere thanks to **Prof. Dr. Yoichi Ando**. Thank you for giving me the opportunity to study and work with you. You have the endless enthusiasm and energy on science. As a professor of experimental physics, you have a strong theoretical background. You can always find the most important research topic and solve the main problems. Thank you for your patience on teaching and guiding me.
I also want to thank **Prof. Dr. Thomas Lorenz**. Thank you for being my second reviewer and attending ny thesis advisory committee.
I would like to thank the committee Chair **Prof. Dr. Petra Becker-Bohatý** for taking the time out of your schedules.
Prof. Dr. Fan Yang, I have learned a lot from you at the beginning of my first two years. Thank you for the many times of discussion with you, even you are in China.
Thanks to Dr. Junya Feng, Dr. Dingxun Fan and Dr. Yongjian Wang. Not only the help in physics but also the help in life.
Thank you, Dr. Oliver Breunig. You are kindly to help me solve the Labview and measurement equipmets problem in this five years.
I want to thanks my translator. Dr. Andrea Bliesener and Felix Münning.
Thanks to all the members in the Ando group. It's a happy experience work and study together with you.
And finally I would like to thank **my family** for the support and love they gave to me. Thanks to my two-moths-old daughter **Yuyu Bai** and to my beloved wife **Yuxi Shang**.

Abstract

The work in this thesis was motivated by the theoretical prediction that a pair of Majorana bound states (MBSs) will be formed in Josephson junctions (JJs), which consist of s-wave superconductors (SCs) and three-dimensional topological insulators (3D TIs). A fractional Josephson effect is expected in such JJs with a 4π-periodic current phase relation. Our JJs are based on the MBE-grwon $(Bi_{1-x}Sb_x)_2Te_3$ (BST) film. Both planar JJs and sandwich JJs were fabricated and characterized by transport measurements.

First, we discovered that SCs are formed by magnetron sputtering Pd onto BST film. The transition temperature (T_C) and the upper critical field (H_{C2}) of the SCs were characterized in Hall-bar devices based on Pd/BST bilayer films. To identify the SC phase in our samples, scanning transmission electron microscopy (STEM) Energy-dispersive x-ray spectroscopy (EDX) were performed. STEM and EDX analyses show the result that the self-formed $PdTe_{1,2}$ SCs are epitaxially formed on the BST film. A planar SC-TI-SC JJ is built when two Pd electrodes are deposited on BST film with a small gap. A supercurrent and a Fraunhofer-like pattern were observed on this JJ, suggesting that BST film is proximitized by self-formed SCs successfully. To characterize the junction transparency, a superconducting quantum interference device (SQUID) was fabricated. A high transparency ~ 0.96 is obtained based on the Octavio-Tinkham-Blonder-Klapwijk (OTBK) theory. For most of the planar JJs, the interface between SCs and TIs is on the surface of TI. The surface can be polluted by water and oxide layers during nanofabrication. While the interface is inside the TI film and the SCs are epitaxially grown in our device. These are possible reasons for the high junction transparency. However, there is a lack of features for the existence of multiple Andreev reflections, which is usually observed in high-transparency JJs. Epitaxial growth of a superconductor on the TI surface is still challenging. Our discovery of unexpected self-epitaxy to form SCs on the surface of BST makes the nanofabrication of devices with an epitaxial SC/TI interface much more straightforward. These devices provide a good platform to realize the Fu-Kane proposal in TIs to engineer a topological superconducting (TSC) state.

Second, we found that SCs can also form when Pd is thermally-deposited onto BST films. The SCs of PdTe and $PdTe_2$ with an "epitaxial" interface is confirmed by STEM and EDX analyses. It is different from the case of the sputter-deposited Pd. The Pd penetrates fully through the BST film when Pd was deposited by thermal evaporation. This finding opened the possibility to create a TI nanowire sandwiched by SCs, by converting the BST film into the SC and leaving only a narrow BST channel to remain as the pristine TI. TI nanowires are created in this way that is confirmed by STEM. The finding of the complete conversion of BST into SCs also opened the possibility to build SC-TI-SC sandwiched JJs. The TI nanowire was proximitized by self-formed SCs successfully. Standard Fraunhofer patterns were observed on such JJs, suggesting that the supercurrent is not due to a superconducting short-circuit and the distribution of the supercurrent is homogeneous. The junction transparency is about 0.8, and the resonance conductance peaks resulting from multiple Andreev reflection (MAR) were observed. The MAR feature observed with the index up to 9 and at temperatures up to 1.0 K which is close to the transition temperature of self-formed SCs, suggesting that the

superconducting proximity effect in JJs is strong. Finally, we did the Shapiro measurements. The $m = 1$ Shapiro step is clearly missing at low frequencies and low power. Two possible topologically trivial origins of the first step missing are Landau-Zener transitions (LZTs) and hysteretic $I-V$ characteristics. Temperature dependence of the Shapiro steps shows that the $m = 1$ step is still missing at a high enough temperature where the hysteretic $I-V$ behavior is completely gone. Landau-Zener transition is considered when the junction transparency is close to 1, but our junction transparency is not that high. We proved that the origin of the missing first Shapiro step is neither hysteretic $I-V$ characteristic nor Landau-Zener transitions. These phenomena are reproduced in another two devices. Hence, our Shapiro-step suggest that a 4π-periodic contribution in the sandwich JJs. This gives possible evidence for topological Majorana bound states.

Erklärung zur Dissertation

Hiermit versichere ich an Eides statt, dass ich die vorliegende Dissertation selbstständig und ohne die Benutzung anderer als der angegebenen Hilfsmittel und Literatur angefertigt habe. Alle Stellen, die wörtlich oder sinngemäß aus veröffentlichten und nicht veröffentlichten Werken dem Wortlaut oder dem Sinn nach entnommen wurden, sind als solche kenntlich gemacht. Ich versichere an Eides statt, dass diese Dissertation noch keiner anderen Fakultät oder Universität zur Prüfung vorgelegen hat; dass sie - abgesehen von unten angegebenen Teilpublikationen und eingebundenen Artikeln und Manuskripten - noch nicht veröffentlicht worden ist sowie, dass ich eine Veröffentlichung der Dissertation vor Abschluss der Promotion nicht ohne Genehmigung des Promotionsausschusses vornehmen werde. Die Bestimmungen dieser Ordnung sind mir bekannt. Darüber hinaus erkläre ich hiermit, dass ich die Ordnung zur Sicherung guter wissenschaftlicher Praxis und zum Umgang mit wissenschaftlichem Fehlverhalten der Universität zu Köln gelesen und sie bei der Durchführung der Dissertation zugrundeliegenden Arbeiten und der schriftlich verfassten Dissertation beachtet habe und verpflichte mich hiermit, die dort genannten Vorgaben bei allen wissenschaftlichen Tätigkeiten zu beachten und umzusetzen. Ich versichere, dass die eingereichte elektronische Fassung der eingereichten Druckfassung vollständig entspricht.

Teilpublikationen:

Mengmeng Bai, Fan Yang, Martina Luysberg, Junya Feng, Andrea Bliesener, Gertjan Lippertz, A. A. Taskin, Joachim Mayer, and Yoichi Ando; *Novel self-epitaxy for inducing superconductivity in the topological insulator* $(Bi_{1-x}Sb_x)_2Te_3$; Phys. Rev. Materials 4, 094801 (2020).
Mengmeng Bai, Xian-Kui Wei, Junya Feng, Martina Luysberg, Andrea Bliesener, Gertjan Lippertz, A. A. Taskin, Joachim Mayer, and Yoichi Ando; *Novel realization of superconducting topological-insulator nanowires*; arXiv preprint arXiv:2108.08559, (2021).

Datum / Unterschrift

CV

Curriculum Vitae

❖Personal data

First name: Mengmeng
Surname: Bai
Data of birth: 19.08.1989
Place of birth: Henan, China
Citizenship: Chinese
Address: Luxemburger Str. 124-136, 50939 Cologne
Phone: +49-02214707944
E-mail: bai@ph2.uni-koeln.de

❖Education

12/2016-Present: **Ph. D. student in Physics**, Institute of Physics II, University of Cologne, Germany.
09/2013-07/2016: **Master of Engineering,** Institute of Physics, Chinese Academy of Sciences, Beijing, China.
09/2008-07/2012: **B. Sc in Physics,** School of physics, Shandong university, Jinan, China.

❖Publications

Mengmeng Bai*, Fan Yang*, Martina Luysberg*, Junya Feng, Andrea Bliesener, Gertjan Lippertz, A. A. Taskin, Joachim Mayer, and Yoichi Ando, Novel self-epitaxy for inducing superconductivity in the topological insulator $(Bi_{1-x}Sb_x)_2Te_3$. Phys. Rev. Mater. 4, 094801 (2020).
Mengmeng Bai*, Xian-Kui Wei*, Junya Feng*, Martina Luysberg, Andrea Bliesener, Gertjan Lippertz, Anjana Uday, A. A. Taskin, Joachim Mayer, and Yoichi Ando, Novel realization of superconducting topological-insulator nanowires. arXiv:2108.08559 [cond-mat.mes-hall] (2021).

Mengmeng Bai
09.12.2021